UNIVERSITY OF OKLAHOMA

GRADUATE COLLEGE

COMPUTATIONAL INVESTIGATION OF TURBULENT BLOOD FLOW AND HEMOLYSIS IN BIOMEDICAL DEVICES

A DISSERTATION

SUBMITTED TO THE GRADUATE FACULTY

in partial fulfillment of the requirements for the

Degree of

DOCTOR OF PHILOSOPHY

By

MESUDE OZTURK
Norman, Oklahoma
2015

COMPUTATIONAL INVESTIGATION OF TURBULENT BLOOD FLOW AND HEMOLYSIS IN BIOMEDICAL DEVICES

A DISSERTATION APPROVED FOR THE
SCHOOL OF CHEMICAL, BIOLOGICAL AND MATERIALS ENGINEERING

BY

_____
Dr. Dimitrios V. Papavassiliou, Chair

_____
Dr. Edgar A. O'Rear III, Co-Chair

_____
Dr. Lance L. Lobban

_____
Dr. Robert L. Shambaugh

_____
Dr. Ramkumar N. Parthasarathy

I dedicate this dissertation to my father Halit Avci who is the most important person in my life. I am so grateful to him for all of his endless support, love, and prayers.

Acknowledgements

This thesis would not have been possible without the support of many people. I would like to thank all those who have helped me during my PhD study.

In the first place, I am very grateful to my advisors, Dr. Papavassiliou and Dr. O'Rear, for their encouragement, guidance and support. They were always helpful and understanding to their students including me. I am heartily thankful for their trust in me.

I am also thankful to Dr. Lobban, Dr. Shambaugh, and Dr. Parthasarathy for being my committee members. In addition I want to thank Dr. Snyder and Dr. Schmidtke for their help and suggestions during our meetings.

I am indebted to Dr. Ekmekyapar from Inonu University for his guidance and help. He opened my mind and motivated me to attend graduate school.

I had a great time with all research group members specifically with Minh Vo. I appreciate the help from Minh Vo on my conference preparations. My gratitude also goes to Zahra Shahrashoob, Sung Young Kim, Taiwo Omotoso, and Kritika Sharma for their assistance and friendship.

My deepest gratitude goes to my family for their constant support and love throughout my life. I am heartily thankful to my father Halit Avci for his love and the work ethic that he taught me as a child; and to my brothers Sevban Avci, Huzeyfe Avci, Nusret Muhammed Avci, and my sister Melike Eda Avci for their support and love.

I wish to convey special acknowledgement to my friends Tugba Turnaoglu, Ceyda Gunsel, Lutfiye Hacioglu, Hulya Yilmaz, Fatma Bozkurt, Kadriye Keceli, and Canan Demirdag for their friendship. My thanks also go out to my dearest friend, Naile Korkmaz

for her endless support and friendship. There are not enough words to describe her tremendous help.

The most special thanks go to my husband Serkan Ozturk for his great support, endless patience, and love. I deeply appreciate his encouragement, great sense of humor, listening, understanding, and that he has always been there for me in moments of doubt.

Finally, I would like to thank everybody who was important to the successful completion of this thesis, as well as express my sincere apology that I could not mention each one personally.

Table of Contents

List of Tables

List of Figures

Abstract

Turbulent blood flow in medical devices contributes to blood trauma, yet the exact mechanism(s) have not been fully elucidated. Local turbulent stresses, viscous stresses, and the rate of dissipation of the turbulent kinetic energy have been proffered as hypotheses to describe and predict blood damage.

In this work, simulations of experiments in a Couette flow viscometer, a capillary tube, and a jet were used to examine extensive properties of the turbulent flow field and to investigate contributing factors for red blood cell hemoglobin release in turbulence by eddy analysis. Moreover, flows in a Couette viscometer and a capillary tube were simulated to investigate the impact of Reynolds and viscous stresses on hemolysis prediction using computations. Also, the applicability of four different hemolysis power law models for the capillary tube flow was tested as a function of area averaged and time averaged Reynolds stresses, viscous, total, and wall shear stresses. Finally, the size of Kolmogorov scale eddies was used to define a turbulent flow extensive property, and a new hemolysis model was proposed. This empirical model can work well with devices that exhibit different exposure times and flow conditions.

It was found that hemolysis occurred when dissipative eddies were comparable in size to the red blood cells. The Kolmogorov length scale was used to quantify the size of smaller turbulent eddies, indicating correspondence of hemolysis with number and surface area of eddies smaller than about 10 μm. There was no evidence of a threshold value for hemolysis in terms of Reynolds and viscous stresses. Therefore, Reynolds and viscous stresses are not good predictors of hemolysis. In the case of power law models, area averaged Reynolds stress with the Zhang power law model gave the smallest error.

1 Introduction and Background

1.1 Motivation and Significance

Heart failure is one of several cardiovascular diseases affecting 5.1 million patients in the United States and causing more than 270,000 deaths in 2010. (Figure 1.1 [1]) Furthermore, 50% of people diagnosed with heart failure die within 5 years. [2]

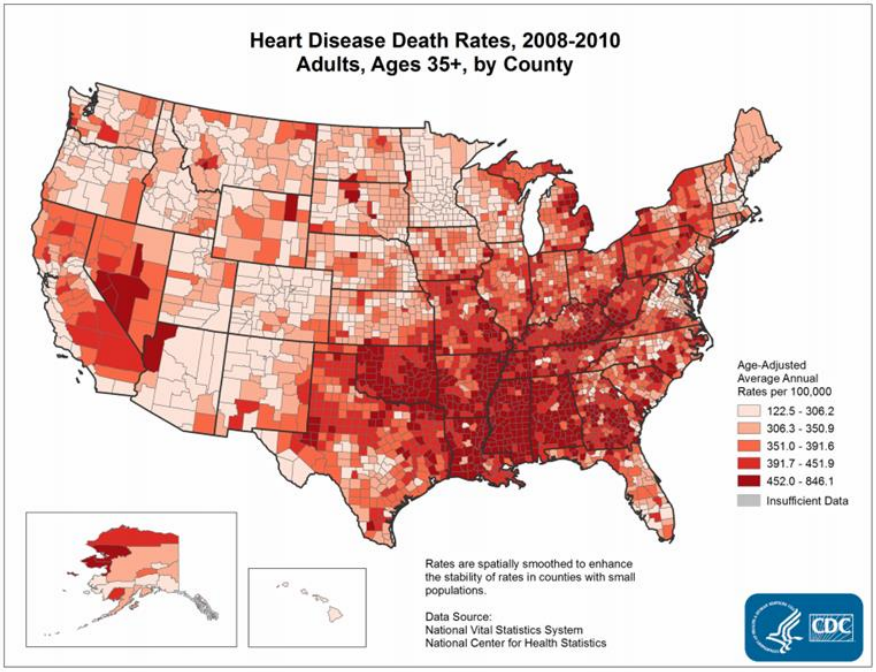

Figure 1.1. Heart disease rates in U.S. [2]

Heart failure is initially treated with medications, life style changes like diet and exercise, and surgery. For patients at an advanced stage of heart failure, the only definitive option is a heart transplant. However, heart transplantation will help only 6% of an estimated 35,000 patients in the United States, leaving the rest requiring alternative therapies while they are waiting for an insufficient number of donor organs. [3] Therefore, different kinds of prosthetic heart devices have been designed and developed to satisfy

the need for donor organs such as total artificial hearts, portable pump-oxygenators, aortic balloon pumps, and ventricular assist devices (VAD). [3, 4]

Ventricular assist devices (VAD) are commonly used prosthetic heart devices and they introduce an efficient therapy to those patients who are in advanced level of sickness while they wait for a heart donor, or those are not suitable for transplantation. [4] Initially intended as a bridge to heart transplantation, VADs are now often employed as a destination therapy providing lifetime support. [4] There are three kinds of ventricular assist device: left ventricular assist device (LVAD), right ventricular assist device (RVAD) and bi-ventricular assist device (BiVAD), which simultaneously supports both sides. [5] A left ventricular assist device (LVAD) maintains the pumping function of the left ventricle, which is the main pumping chamber, because it pumps the blood to the whole body except the lungs (right ventricle pumps to the lungs). In LVAD, when blood exits from the left ventricle, it goes to the pump through an inflow conduit and exits from the pump through an outflow conduit into the body as shown in Figure 1.2. [6] Development and optimization of better designs of VAD devices will help patients to recover fast and return to their normal life.

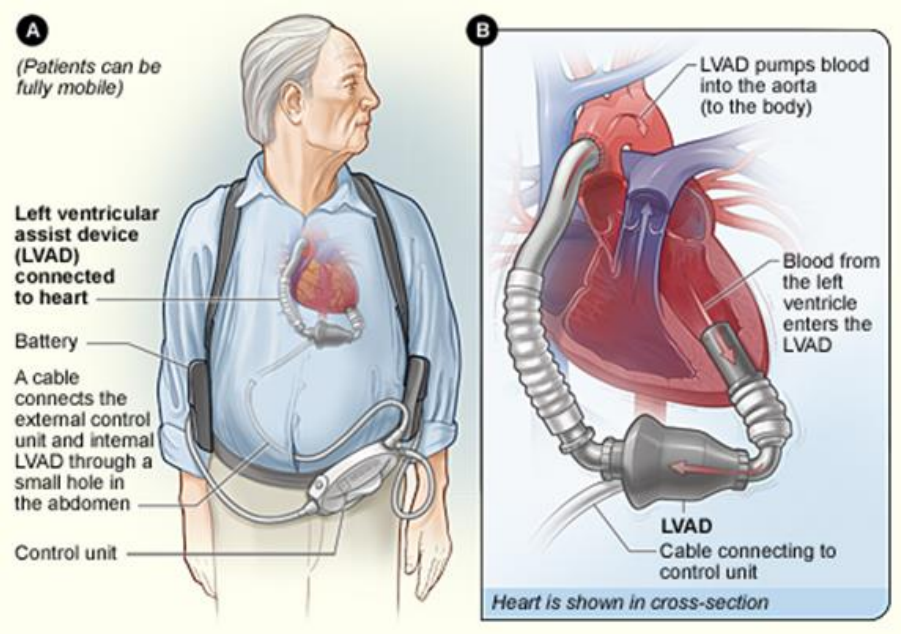

Figure 1.2. (A) Location of the heart and the typical equipment needed for an implantable LVAD. (B) LVAD connection to the heart. [6]

Ventricular assist devices and artificial hearts create non-physiological blood flow conditions, [3] such as turbulence, [7, 8] causing red blood cell (RBC) damage, an important consideration in the design of prosthetic heart devices. Turbulent flow means that irregular, random, chaotic, and multiscale flow conditions prevail with a wide range of time and length scales that cause harmful effects in blood, because of significant fluctuations in shear stresses and pressure. It is commonly accepted that turbulence effects are important to RBC damage causing hemolysis, i.e., release of hemoglobin from erythrocytes, which increases when cells are exposed to turbulent stresses. [9] While stress levels are well characterized for laminar flow fields, the effects of turbulence structure on hemolysis of blood cells are unclear. [9-11] Predicting and understanding the effect of turbulent stresses on erythrocytes would lead to more rational design of prosthetic heart devices. [9-11]

1.2 Blood and Blood Damage

1.2.1 Blood Properties

Blood constitutes about 8% of an average adult's body weight and its role is to transport material to and from tissue, prevent fluid loss, and defend the body. Blood is a mixture of plasma, which makes up 55% of blood's volume, and blood cells, which makes up the remaining 45%. While plasma consists of water, protein, inorganic salts, and organic substances, blood cells include white blood cells, platelets, and red blood cells (erythrocytes). For every 600 red blood cells (RBC), there are around 40 platelets and 1 white cell, while the human body contains approximately 25 trillion erythrocytes. Red blood cells, which are composed of 90% hemoglobin, are constantly created in the bone marrow and stay alive approximately for 120 days. [12] (Figure 1.3 [13])

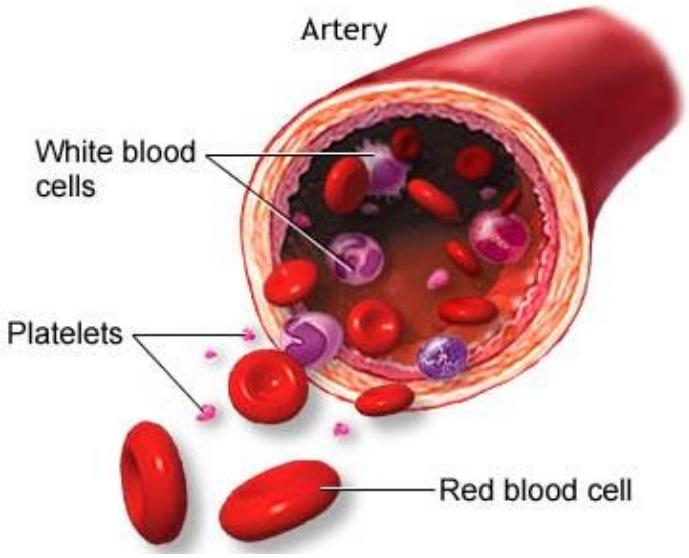

Figure 1.3. Cellular components of blood. [13]

The physical properties of blood are important in blood trauma studies. Generally, blood density is constant and is taken as 1050 kg/m^3. Blood viscosity is shear-thinning, which means viscosity decreases when shear stress increases, and depends on temperature

and hematocrit. Blood is often assumed to be Newtonian in modeling of cardiovascular devices, [8] because blood can be treated as a Newtonian fluid for shear rates above $100s^{-1}$ that is found in many applied problems. [8] Mostly, Newtonian blood viscosity is taken as 3.0 – 4.0 centipoise (cP) at 37 ^{o}C. [10, 14, 15] Another consideration is the assumption of blood as a homogeneous fluid. However, blood has often been represented as a homogeneous fluid by many investigators. [10, 16-18] Since blood contains suspended red blood cells in plasma, it has not always been considered as homogeneous, see for example the work of Antiga et al. [7] In all of the experiments of this study, blood was assumed to be Newtonian and homogeneous.

1.2.2 Blood Damage and Shortfalls of Current Models

Prosthetic heart devices expose blood to non-physiological conditions, [3] such as turbulent blood flow, [7, 8] causing locally high shear stresses and significant pressure fluctuations in blood. These non-physiological conditions cause different kinds of complications including hemolysis, infection, anemia, secondary shear effects of immunosuppression, thrombosis, and bleeding. [3] (Figure 1.4 [19]) In this study, we will be concentrating only on hemolysis. Hemolysis happens when hemoglobin is released from erythrocytes (RBCs) as a result of destruction or of trauma to the RBC.

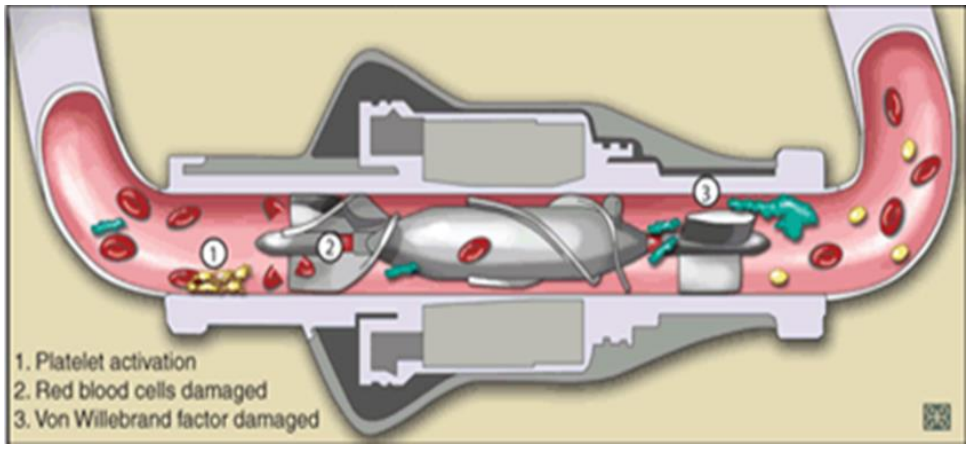

Figure 1.4. Ventricular assist device. [19]

Blood damage is often represented by empirical power law models that are consider it to be a function of the magnitude of the shear stress and of exposure time to high stresses. Blackshear et al. [20] proposed the following commonly used equation:

$$HI = C\tau^{\alpha}t^{\beta} \qquad \textbf{1.1}$$

where HI, hemolysis index, is a measure of hemolysis, τ is shear stress, t is time of exposure to stress τ, and α, β, and C are constants to be determined experimentally. These constants have been obtained largely from laminar flow data with well-defined homogeneous stress and exposure time to that stress.

The power law equation [Eq. 1.1] was adopted by Giersiepen et al. [21], based on in-vitro laminar flow experiments with human RBC, to predict hemolysis downstream of aortic valves. Constants α, β, and C were determined from regression analysis applied to experimental data for shear stresses less than 255 Pa and exposure times less than 700 ms. Heuser and Opitz [22] obtained their set of coefficients using laminar flow in a Couette viscometer to determine hemolysis of porcine blood for exposure times less than 700 ms and shear stresses less than 255 Pa. Fraser et al. [23] calculated hemolysis and

obtained their set of coefficients in laminar flow for shear stresses less than 5 Pa and exposure times of less than 1.81s. Zhang et al. [24] examined hemolysis of ovine blood for exposure times of less than 1500 ms and shear stresses between 50-320 Pa and obtained power law constants by fitting the hemolysis results to Eq.1.1. These models are summarized in Table 1.1. Furthermore, many other investigators developed different mathematical expressions by using Eq. 1.1 for hemolysis estimation. [25-28] There are also more advanced models that consider more detailed information about RBC, such as pore formation of membrane, distortion of cells, and hemoglobin transport from cells. [29, 30]

Table 1.1. Power law models and constants

Power Law Models	**C**	α	β
Giersiepen et al. [21]	$3.62*10^{-5}$	2.416	0.785
Heuser and Opitz [22]	$1.8*10^{-6}$	1.991	0.765
Fraser et al. [23]	$1.745*10^{-6}$	1.963	0.7762
Zhang et al. [24]	$1.228*10^{-5}$	1.9918	0.6606

Even though power law models have been helpful to understand mechanical trauma for several years, determining hemolysis as a function of shear stress and exposure time is not enough to fully identify damage to RBCs. Therefore, alteration of the power law models or the use of entirely different models have been proposed by several researchers. [15, 25, 31-37]

The biggest disappointment in the power law hemolysis models is the lack of universality of the model. As discussed above, the constants in the power law models

were entirely empirical, depending on specific flow conditions and device features. Moreover, since these models are purely empirical, they do not consider mechanical properties of the RBC while missing any physical basis. [38]

Another most important shortfall of power law models is that adjustment of power law constants has been used in order to force models based on laminar flow experiments to work for devices with turbulent flows. However, these models are missing the general flow features of typical medical devices because they were derived from steady viscometer experiments with uniform shear stress. [30] The use of a particular power law expression derived from typical viscometer experiments [20, 22, 39] is problematic for turbulent flows. Experimental determination of an average shear stress in these viscometers derives from the observed torque for a specified geometry, dimensions and operational speed of the unit. A single torque value, however, cannot describe the complexity of turbulent flows. It is possible that the combined effect of local variations in flow field structure around a cell on hemolysis cannot be captured by a single value of stress.

To deal with hemolysis in a turbulent flow field, application of a power law model in a Lagrangian sense has also been employed. However, analysis of hemolysis in devices with this method has yet to demonstrate consistent power law constants in large part due to the difficulty in characterizing turbulent stresses. [40]

1.3 Effects of Turbulence on Hemolysis

Turbulence is a random, highly three dimensional, chaotic, irregular and multiscale flow condition that results in strong vorticity, high rate of mixing, with

pressure and velocity variations occurring over a wide range of time and length scales. [41] Rapidly moving impeller blades of heart devices is the reason for highly disturbed turbulent flow in/near these devices.

It is commonly accepted that turbulence has important effects on RBC damage. One of the most common and widely studied effects is hemolysis. While an increase in hemolysis is observed when cells are exposed to turbulent stresses, [9] the structure of turbulence in proximity to the blood cells and the fundamental mechanism by which cells are injured remain unclear. [9-11] Therefore, understanding and predicting the effect of turbulent stresses on erythrocytes is a major concern when designing prosthetic heart devices. [9-11] To deal with blood damage in turbulent flow, hemolysis has been examined using different stresses (Reynolds, viscous, wall shear, etc.) by several researchers.

Quinlan and Dooley [18] have presented an analysis for both laminar and turbulent flow. In their turbulent flow analysis, a model to predict shear stress on RBCs was developed by considering the effect of turbulent flow on an isolated cell. They applied their model to prosthetic valve data by Liu et al. [42] and investigated the relationship between true stress on blood cells and the measurable macroscopic stresses. Hemolysis occurs at the cellular scale and Reynolds stress does not directly describe microscopic flow field experienced by red blood cells. [18, 43-45]. Moreover, the stress distribution on the surface of the cell was affected by complicated local plasma flow around each cell. Quinlan and Dooley suggested that cells are exposed to low stress and acceleration by larger eddies. However, smaller eddies are responsible for causing the cells to experience high velocity gradients and fast velocity changes. Therefore, effect of

different length scales on cells cannot be captured separately by using Reynolds stresses. [18] Viscous stresses also characterize blood in macroscopic levels and they are not adequate to define the flow field near the cells to determine hemolysis. [18] Lee et al. [46] investigated viscous and Reynolds stresses for three different heart valves. The calculated maximum value of viscous shear stresses was small. Therefore, the effect of viscous stresses on cell trauma was neglected.

In the work of Hund et al., [8] the Navier Stokes and Reynolds Averaged Navier Stokes (RANS) equations were used to mathematically calculate the errors of predicted blood damage. It was found that significant error can be anticipated when Reynolds stresses are used in a power law equation to predict hemolysis. As such, if Reynolds stresses are used in blood damage calculations, the accuracy of the predictions would be doubtful. [8] However, Hund et al. also noted surprising success of some groups on predicting hemolysis by using Reynolds stresses.

The value of Reynolds stresses in predicting blood damage was also investigated by Jones. [47] Local viscous stresses were determined in turbulent flow and it was suggested that using local viscous stresses instead of Reynolds stresses to determine hemolysis was more reasonable. [47] Even though Reynolds stresses were used to correlate hemolysis results in the work of Sallam and Hwang, [48] viscous shearing was recommended as a potential mechanism. [49, 50] Other researchers have considered Reynolds stresses as having a similar effect as the viscous stresses in laminar flows. [17, 42, 48, 51]

While turbulent stresses, the well-known Reynolds stresses, have often been considered responsible for hemolysis, [8, 9, 48, 51] other researchers have examined the

size of flow eddies relative to the size of the RBCs in order to identify the mechanism responsible for RBC trauma. [10, 42, 47, 52]

Turbulent flow eddies are known as an important mechanism on hemolysis. The smallest dissipative flow eddies in turbulent flow, known as Kolmogorov length scale eddies have a length scale that is described as $KLS = \left(\frac{\nu^3}{\varepsilon}\right)^{1/4}$, where ν is kinematic viscosity and ε is the dissipation rate of turbulent kinetic energy. The dissipation mechanism of turbulent eddies is known as the Energy Cascade [53-55] in which large eddies break up continually and transfer their energy to smaller eddies (Figure 1.5). Viscosity effects are negligible for larger eddies but when eddies smaller, viscosity effects and dissipation become more important. Energy cascade continues until eddy sizes become so small (size of KLS) that viscous forces and dissipation become important. At the end of Energy Cascade, the small eddies with size of a RBC can interact with the cell and transfer their energy to the cell membrane causing membrane rupture and hemolysis. However, if these eddies are larger than RBCs, the cells are displaced within the flow field and the cell membrane does not experience stressing or damaging. Thus, a relationship between dimensions of the turbulent eddies and the RBC damage can be obtained by examining the information of the smallest turbulent eddies. [56] Several researchers suggest that when KLS size is smaller, especially similar to RBC size, there will be more damage to RBCs. [10, 43, 47, 51, 57, 58]

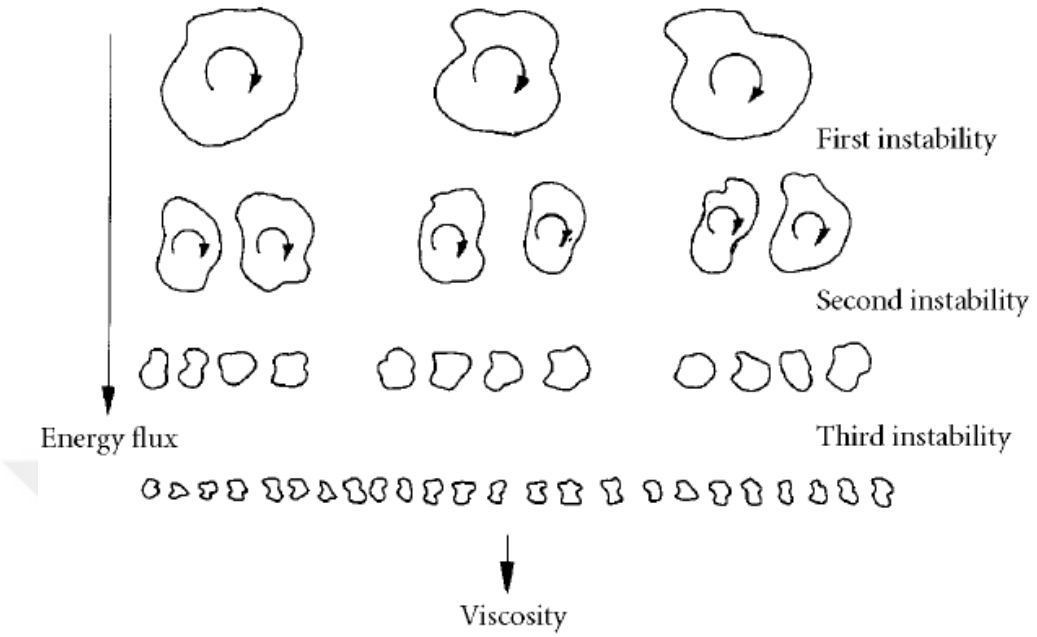

Figure 1.5. A schematic representation of energy cascade in turbulent flow. [53]

Ellis et al. [51] determined KLS values as 7.1 μm in a turbulent jet study, and concluded that turbulent energy dissipates through the membranes of blood elements and ruptures them when turbulent eddies are similar in size with blood elements. Aziz et al. [10] calculated Kolmogorov length scales in a stirred tank reactor and concluded that Kolmogorov length scale correlates inversely with damage, i.e., smaller eddies cause more damage. Jones [47] also calculated Kolmogorov length scales and stated that when length scales are similar with RBC size, shearing becomes important for hemolysis. An approach based on KLS is closely tied to energy dissipation and can be computationally manageable.

1.4 Objectives

Turbulence in which large turbulent eddies break up continually and transfer their energy to smaller eddies has important effects on flow properties which a pump designer needs to pay attention. These effects include pressure head evaluation, and the prediction of shear stress, which are important in blood damage calculations. [3] It is commonly accepted that hemolysis increases when cells are exposed to turbulent stresses. [9] However, the structure of turbulence in proximity to the blood cells and the fundamental mechanism by which cells are injured remains unclear. [9-11] Therefore, understanding and predicting the effect of turbulent stresses on erythrocytes is a major concern when designing prosthetic heart devices. [9-11]

Hemolysis calculation in turbulent flow is a big challenge because of complex flow conditions of turbulence, lack of experimental data, uncertainty of a threshold shear stress value, and, most importantly, the lack of understanding of turbulence structure in proximity to the blood cells and the fundamental mechanism of cell damage. This work fills a gap on understanding the mechanism of turbulence structure on hemolysis by performing Computational Fluid Dynamics (CFD) simulations on distinctly different and widely used geometries.

The primary objective of this work is to examine, for the first time, the correspondence of hemolysis to the surface area of eddies that are assumed to have diameters equal to the KLS length scale by using CFD simulations (we call this process eddy analysis). The main hypothesis is that extensive measures of turbulent eddies with sufficient energy dissipation could be a predictive indicator of trauma – the more of these eddies, the more exposure RBCs will have to them. It might also be envisioned that the

stresses within and between eddies cause damage. The damage to cells from such eddies will be greater for similar total exposure times in a flow field. This is a measure of hemolysis based on an extensive property in turbulent flows. It thus takes into consideration that turbulence is a flow condition rather than a fluid property, in contrast to intensive measures.

Another objective of the present study is to consider a different aspect of the power law approach by testing applicability of area averaged, time averaged Reynolds, total, viscous, and wall shear stresses using reported power law parameters [21-24] utilizing hemolysis experiments in a capillary tube. Moreover, as discussed above several researchers calculated hemolysis by using different stresses such as Reynolds, viscous, and wall shear. Which characterization of turbulent stress relates best to hemolysis is an important consideration for application of the power law. If the dependence on Reynolds stresses is similar to what is seen for stresses in laminar flow, then one expects to see a large increase in hemolysis at some threshold value of the Reynolds stress, because of the exponential feature of the power law relationship. However, the issue of a value of the threshold turbulent stresses for hemolysis remains unsettled. [59] As such, in this research we investigate the effect of time averaged, area averaged Reynolds stresses and viscous stresses on hemolysis by conducting a threshold analysis.

Moreover, as discussed above, power law models often fail to predict hemolysis in medical devices because they were derived from steady viscometer experiments with uniform shear stress. [30] Therefore, we also propose a hemolysis model based on results from three distinctly different devices: a jet, [57] a Couette viscometer, [60] and a capillary tube. [9] We also perform eddy analysis on jet flow and investigate the relation

between hemolysis and surface area of eddies. With eddy analysis on jet, we validate and support our previous work [61] in which we applied the same methodology to a Couette viscometer [60] and a capillary tube. [9]

2 Methods

2.1 Computational Fluid Dynamics

Computational Fluid Dynamics (CFD) is the study of fluid flow by using powerful computers. Simulation of fluid flow simply means that a series of well-known equations, i.e., Navier-Stokes equations, are solved in computers for a particular geometry and flow conditions. Solving the Navier-Stokes (N.S.) equations in supercomputers gave rise to the field of CFD and became one of the greatest achievements in fluid dynamics. [62] Governing equations for flow consist of the continuity equation, Eq. 2.1, and the momentum equation, Eq. 2.2 (Equations are in tensor form).

$$\frac{\partial \rho}{\partial t} + \frac{\partial \left(\rho U_i \right)}{\partial x_i} = 0 \text{ or } \frac{\partial U_i}{\partial x_i} = 0 \text{ (for incompressible flow)} \quad \textbf{2.1}$$

$$\frac{\partial U_i}{\partial t} + U_j \frac{\partial U_i}{\partial x_j} = -\frac{1}{\rho}\frac{\partial p}{\partial x_i} + \nu \frac{\partial^2 U_i}{\partial x_j \partial x_j} \quad \textbf{2.2}$$

where U_i and U_j are the instantaneous velocity in the i and j directions respectively, ν is kinematic viscosity, ρ is density, p is pressure, and x_i, x_j are coordinate directions. It is well-known that there is no general solution to the N.S. equations, thus there is no general solution to turbulent flow problems. [63] The N.S. equations for simple turbulent flows at moderate Reynolds numbers, Re, can be solved numerically by direct numerical simulation (DNS). However, common applications that require high Re flows do not have a direct solution of N.S. equations. [41] Therefore, CFD techniques have been developed that include statistical approaches and methods such as finite difference, finite volume, finite element, and spectral methods. A computational domain, which is a bounded region

in space, is needed for flow simulation. Interaction between computational domain and the surrounding is represented by the boundary of this region. A solver is used to calculate the flow within the domain by using the information about the flow on the boundary. After boundary conditions are determined, the computational domain is discretized into a number of small cells, generating the computational mesh or grid. In each cell of the domain, discretized versions of governing equations [Eq. 2.1 and Eq.2.2] are solved numerically, and provide the flow field with regard to velocity and pressure (temperature and density, if needed). The solution changes with time for an unsteady flow therefore results are needed to be obtained as a function of time to yield temporarily varying flow field. On the other hand, there is only one solution for steady flow field (time independent). While several different numerical techniques (such as finite difference method, finite element method, spectral methods, and spectral element methods) are available, the finite volume method is the most commonly used numerical technique that is also generally available for commercial CFD codes. In the finite volume method, the governing equations [Eq. 2.1 and Eq.2.2] are integrated over each cell in the domain and the terms of the equations are approximated with algebraic expressions. The number of unknowns (three velocity components and one pressure component) and the number of equations (one continuity equation and three momentum equation) are equal in incompressible, three-dimensional flow. When these equations are applied to each cell of the mesh (boundary conditions control the cells on the boundaries), there will be a system of algebraic equations that is solved for the unknown variables in each cell. Because of the integration over each cell, the values of variables are spatial averages for each cell in the domain.

CFD has been widely used to determine hemolysis as a function of flow field conditions found in cardiovascular devices and has often been used to analyze, improve, and optimize VADs. [23, 64-68] Correct measurements of flow parameters, such as the instantaneous spatial distribution of the rate of dissipation of turbulent kinetic energy (ε), are difficult in the laboratory, which makes CFD essential for these systems. Furthermore, several different implant designs can be created in silico and examined for a broad range of operating conditions without the time and expense necessary for the production and testing of prototype devices. For example, over the last decade several researchers have used CFD to develop, analyze, and optimize VADs. [64, 68]

2.2 CFD Analysis

CFD analysis in this work includes the following steps: creating and modeling the experimental devices, meshing the geometries, solving the problem by setting up boundary conditions, and post processing using Fluent, Excel, and Matlab. All the simulations are performed in Fluent 14.0 by using a Dell Precision PC. Simulation time varies from order of seconds to hours depending the simulation type. Analysis of all the devices in this work was performed with a three dimensional model to represent the flow domains. Each analysis includes different setup, but the general setup is similar in different devices.

First of all, the experimental setup representing the flow domain was created using ICEM CFD (Ansys, Pittsburgh, PA), a preprocessing program of Fluent. After creating the geometry, the computational domain was discretized into a mesh. Hexahedral elements were used for the meshing. After boundary conditions appropriate for each specific experiment were defined, the discretized mesh was imported into Fluent. For

each turbulent simulation, a turbulence model was specified in Fluent. Most of the time k-ε and k-ω SST models were chosen, since they are the most commonly used models and have wide range of applicability. [41] Moreover, specific boundary conditions, such as the average inlet velocity, were specified for the fluid entering the domain.

In order to solve the problem in Fluent, another important step is to determine solution parameters that include determining the discretization method and convergence. Mostly, first or second order discretization schemes are used for all Fluent runs. In order to determine whether the problem solution converged or not, a specific convergence criterion was set for the simulation. After determining convergence criteria, the final step before running the program is to initialize the simulation. For turbulent flow simulations, simulations start with a slow velocity (or rotational velocity in Couette viscometer) such that the flow remained laminar, then the velocity was slowly increased in silico until the resulting parameters equaled the experimental parameters. This parameter can be experimental shear stress, experimental velocity or any other parameter depending on different experiments. Detailed explanations of turbulent flow simulations for different experimental systems are presented in Sections 3, 4, and 6. After simulation started running, residuals and also some other monitors (if necessary) were monitored. Once they reach below convergence criteria, the simulation ended.

2.3 Modelling Turbulent Flow

2.3.1 k-ε SST Turbulence Modelling

The turbulence k-ε model is a semi-empirical Reynolds Averaged Navier-Stokes (RANS) model, which solves model transport equations for the turbulent kinetic energy, k, and the turbulent kinetic energy dissipation rate, ε. The k-ε model is the most

commonly used turbulence model which is also used in most commercial CFD codes.[41] Some of the advantages of the k-ε model are robustness, reasonable accuracy for wide flow ranges, and computational economy.[3, 8] The k-ε model is known to be inaccurate in capturing turbulent features in highly swirling flows and when secondary flows are present in non-circular ducts, and also in capturing non-zero normal-Reynolds stress (Re) differences. [8] Further, it is not very accurate when calculating fluid characteristics along the boundary during flow separation. [69] The flows simulated here do not fall in these categories. In this study, the turbulence k-ε model has been used with enhanced wall treatments to define and satisfactorily solve near wall flow conditions. The k-ε model has been commonly used to design prosthetic heart devices.[69-74] In the turbulence k-ε model, the turbulence kinetic energy, $k = \frac{1}{2}\overline{u_i' u_i'}$, and the dissipation rate of turbulent kinetic energy, $\varepsilon = 2\nu\overline{s_{ij}' s_{ij}'}$, $(\overline{s_{ij}'} = \frac{1}{2}\left(\overline{\frac{\partial u_i'}{\partial x_j}} + \overline{\frac{\partial u_j'}{\partial x_i}}\right))$ are determined as:

$$\frac{\partial}{\partial t}(\rho k) + \frac{\partial}{\partial x_j}(\rho k U_j) = \frac{\partial}{\partial x_j}\left[\left(\mu + \frac{\mu_t}{\sigma_k}\right)\frac{\partial k}{\partial x_j}\right] + G_k - \rho\varepsilon \qquad \textbf{2.3}$$

$$\frac{\partial}{\partial t}(\rho \varepsilon) + \frac{\partial}{\partial x_j}(\rho \varepsilon U_j) = \frac{\partial}{\partial x_j}\left[\left(\mu + \frac{\mu_t}{\sigma_\varepsilon}\right)\frac{\partial \varepsilon}{\partial x_j}\right] + \rho C_1 S\varepsilon - \rho C_2 \frac{\varepsilon^2}{k + \sqrt{\nu\varepsilon}} \qquad \textbf{2.4}$$

$$\mu_t = \rho C_\mu \frac{k^2}{\varepsilon}, \quad C_1 = \max\left[0.43, \frac{\eta}{\eta + 5}\right], \quad \eta = S\frac{k}{\varepsilon}, \quad S = \sqrt{2S_{ij}S_{ij}} \qquad \textbf{2.5}$$

where $\overline{u_i'}$ and $\overline{u_j'}$ are the mean fluctuating velocity in the i direction and j directions respectively, $\overline{s_{ij}'}$ is the mean fluctuating strain rate, ν is kinematic viscosity, ρ is density, μ is viscosity, μ_t is turbulent viscosity, G_k is the generation of turbulent kinetic energy due to the mean velocity gradients, and S_{ij} is the mean strain rate. The standard values of

model parameters are C_2=1.9, C_μ=0.09 and the turbulent Prandtl numbers for k and ε are σ_k=1.0, σ_ε=1.2.[75] These parameters were refined and determined over years from flow balance equations between production and dissipation based on several flow conditions.[75-77]

k-ω SST Turbulence Modelling

The k-ω model is the second most commonly used two- equation model after the k-ε model. [41] The k-ω SST model solves the model transport equations for turbulent kinetic energy, k and ω which is defined as $\omega \equiv \varepsilon/k$. Both k-ε and k-ω models solve the same equation for the turbulence kinetic energy and they differ when solving the second variable. The k-ω model is better on dealing with the viscous near-wall region and influence of streamwise pressure gradients when solving boundary-layer flows. While it has difficulty when solving non-turbulent free-stream boundaries, [41] the simulations in this work are not in that category. For the k-ω turbulence model, the shear-stress transport (SST) k-ω model was used in this study. Menter [78] created the k-ω SST model to obtain the best behavior of k-ε and k-ω models. The k-ω SST model efficiently combines free-stream independence of the k-ε model in the far field region and accurate and robust formulation of the k-ω model in the near-wall region. [75] The k-ω SST is developed as a non-standard k-ω model in which the last term of ω equation is multiplied with a blending function. Blending function becomes zero close to walls (corresponding to the standard ω equation), while far from walls the blending function is 1 (leading to the standard ε equation). The k-ω SST model has also been used commonly to design prosthetic heart devices. [79-82] Transport equations of the k-ω SST model are as follows:

$$\frac{\partial}{\partial t}(\rho k)+\frac{\partial}{\partial x_j}(\rho k U_j)=\frac{\partial}{\partial x_j}\left[\left(\mu+\frac{\mu_t}{\sigma_k}\right)\frac{\partial k}{\partial x_j}\right]+G_k-Y_k \quad \textbf{2.6}$$

$$\frac{\partial}{\partial t}(\rho \omega)+\frac{\partial}{\partial x_j}(\rho \omega U_j)=\frac{\partial}{\partial x_j}\left[\left(\mu+\frac{\mu_t}{\sigma_\omega}\right)\frac{\partial \omega}{\partial x_j}\right]+G_\omega-Y_\omega+D_\omega \quad \textbf{2.7}$$

where G_k is the generation of turbulent kinetic energy due to the mean velocity gradients, G_ω is the generation of ω, Y_k and Y_ω are dissipation of k and ω due to turbulence, D_ω is the cross-diffusion term. Calculation of all of the above terms is shown below.

$$\mu_t=\frac{\rho k}{\omega}\frac{1}{\max\left[\frac{1}{\alpha^*},\frac{SF_2}{a_1\omega}\right]},\ \sigma_k=\frac{1}{F_1/\sigma_{k,1}+(1-F_1)/\sigma_{k,2}},\ \sigma_\omega=\frac{1}{F_1/\sigma_{\omega,1}+(1-F_1)/\sigma_{\omega,2}} \quad \textbf{2.8}$$

$$\alpha^*=\alpha_\infty^*\left(\frac{\alpha_0^*+\mathrm{Re}_t/\mathrm{R}_k}{1+\mathrm{Re}_t/\mathrm{R}_k}\right),\ \mathrm{Re}_t=\rho k/\mu\omega,\ \mathrm{R}_k=6,\ \alpha_0^*=\beta_i/3,\ \beta_i=0.072 \quad \textbf{2.9}$$

$$F_1=\tanh(\phi^4),\ \phi=\min\left[\max\left(\frac{\sqrt{k}}{0.09\omega y},\frac{500\mu}{\rho y^2\omega}\right),\frac{4\rho k}{\sigma_{\omega,2}D_\omega^+ y^2}\right],\ D_\omega^+=\max\left[2\rho\frac{1}{\sigma_{\omega,2}}\frac{1}{\omega}\frac{\partial\omega}{\partial x_j},10^{-10}\right] \quad \textbf{2.10}$$

$$F_2=\tanh(\phi_2^2),\ \phi_2=\max\left[2\frac{\sqrt{k}}{0.09\omega y},\frac{500\mu}{\rho y^2\omega}\right] \quad \textbf{2.11}$$

where y is the distance to the next surface and D_ω^+ is the positive portion of the cross-diffusion term.

$$G_k=-\rho\overline{u_i'u_j'}\frac{\partial u_j}{\partial x_j},\ G_\omega=\alpha\frac{\omega}{k}G_k \quad \textbf{2.12}$$

$$Y_k=\rho\beta^*\mathrm{f}_{\beta^*}\mathrm{k}\,\omega,\quad \mathrm{f}_{\beta^*}=\begin{cases}1 & x_k\le 0\\ \dfrac{1+680x_k^2}{1+400x_k^2} & x_k>0\end{cases},\qquad x_k=\frac{1}{\omega^3}\frac{\partial k}{\partial x_j}\frac{\partial\omega}{\partial x_j},\quad \beta^*=\beta_i^*\left[1+\zeta^*F(M_t)\right] \quad \textbf{2.13}$$

$$\beta_i^* = \beta_\infty^* \left(\frac{4/15 + \left(\mathrm{Re}_t / \mathrm{R}_\beta \right)^4}{1 + \left(\mathrm{Re}_t / \mathrm{R}_\beta \right)^4} \right), \quad \zeta^* = 1.5, \quad \mathrm{R}_\beta = 8, \quad \beta_\infty^* = 0.09 \qquad \textbf{2.14}$$

$$D_\omega = 2\left(1 - F_1\right) \rho \frac{1}{\omega \sigma_{\omega,2}} \frac{\partial k}{\partial x_j} \frac{\partial \omega}{\partial x_j} \qquad \textbf{2.15}$$

The model constants are $\sigma_{k,1} = 1.176$, $\sigma_{\omega,1} = 2.0$, $\sigma_{k,2} = 1.0$, $\sigma_{\omega,2} = 1.168$, $a_1 = 0.31$, $\beta_{i,1} = 0.075$, $\beta_{i,2} = 0.0828$, $a^* = 1$, $a_\infty = 0.52$, $a_0 = \frac{1}{9}$, $\beta_\infty^* = 0.09$, $\beta_i = 0.072$, $R_\beta = 8$, $R_k = 6$, $R_\omega = 2.95$, $\zeta^* = 1.5$, $M_{t0} = 0.25$, $\sigma_k = 2.0$, $\sigma_\omega = 2.0$.

2.4 Eddy Analysis

Fluid flow simulations produced time-averaged spatial distributions of the Kolmogorov length scale (KLS) for each particular geometry and experimental condition. The parts of the geometries in which KLS values were calculated are described in the specific chapters, when we discuss each geometry separately. The same approach was applied for all of the systems in this work. We assume that the distribution of Kolmogorov length scales strongly reflects the distribution of small eddy sizes. Eddy analysis in the virtual geometries began by calculating the values of the KLS in the whole flow domains. With the assumption that the KLS values characterized regions containing spherical eddies of similar size, the total volume for that region led to the number and surface area of eddies representing each KLS value. We picked increments of 1μm for binning the

KLS values and created surfaces for each specific KLS value in Fluent. Surface areas for every KLS were identified in Fluent.

The total volume of regions containing dissipative eddies of similar spherical size was calculated by generating contours of KLS with increments of 1 μm in Fluent, calculating the area corresponding to each contour increment, and then integrating this area throughout the flow domain using contours at planes generated through the flow domain. Total volume calculation for each geometry is also discussed separately in the following chapters. To find the number of eddies (N_{eddy}) of a specific size, the total volume of the region was divided by the volume of one eddy (V_{eddy}) that was calculated as $V_{eddy} = \frac{4}{3}\pi\left(\frac{KLS}{2}\right)^3$. Finally, the total surface area of eddies for each KLS value (A_{eddy}) was calculated as $A_{eddy} = N_{eddy} 4\pi\left(\frac{KLS}{2}\right)^2$. Eddy surface areas were used as a main parameter, because we envisioned that cell damage would take place at the interface between eddies due to shear forces acting on a cell, or possibly extensional stresses. This is a measure of hemolysis based on an extensive property in turbulent flows. It thus takes into consideration that turbulence is a flow condition rather than a fluid property, in contrast to intensive measures. The use of extensive quantities accommodates the complexity of flows in medical devices, which may have considerable spatial variation in turbulence intensity among their parts. A small, highly turbulent region in the device may contribute disproportionately to hemolysis so that the size of that region is important to the extent of damage. The goal was to determine the correspondence of hemolysis with extensive quantities rather than intensive, on a per unit volume basis for different values

of KLS. In addition, cumulative values of these extensive quantities with increasing values of KLS were considered.

The main assumptions for eddy analysis of the dissipative turbulent length scales are as follows:

i) KLS are assumed to correspond to uniform spherical eddies that have radius equal to the KLS;

ii) All volume of the flow domain that displays a particular KLS is occupied by spherical eddies with diameter equal to the KLS;

iii) Turbulent flow in our simulated systems is fully mixed, so RBCs spend time in different zones of KLS values that is proportional to the volume of the flow domain occupied by these KLS values;

iv) The presence of the RBCs does not affect the structure of the turbulence;

v) The rheology of the fluid is Newtonian and homogeneous;

vi) The k-ε and k-ω turbulence models are appropriate for use in the flow configurations examined herein.

For assumption (i), application of eddy analysis in this study of hemolysis is limited to the extent that Kolmogorov length scales correspond directly to turbulence eddies. Moreover, choice of turbulence models for the calculation of the rate of kinetic energy dissipation and, thus, of KLS is quite important to the results. While Kolmogorov scales do not necessarily correspond to actual spherical eddies that are present in turbulent blood flow, we make the assumption that the distribution of Kolmogorov length scales is strongly correlated with the distribution of small eddy sizes. This is an Eulerian approach,

in which we relate time-averaged extensive flow field properties obtained from turbulent eddy size distributions to hemolysis. Regarding assumption (vi), it should be recognized that one would need to fully resolve the turbulent field to have complete information about flow at the cellular scale, since one should not use macroscale turbulence information to obtain information about a time-dependent microscale flow field around a cell or the blood damage response. [44] Flow is assumed to be fully turbulent. [83] Turbulence models adopted herein adequately predict the dissipation field of the turbulent kinetic energy. Other more accurate approaches to determining the dissipative length scales could be combined with the proposed eddy analysis. However, different turbulence models will have an impact on the final calculations for the KLS. We use here the k-ε and k-ω SST models, described in the previous section, which can provide the ε and ω fields, recognizing that other more sophisticated models for turbulence simulation (like large eddy simulations or direct numerical simulations) would provide more accurate results. While the KLS field calculated here is subject to uncertainties associated with the turbulence model, the approach proposed for the definition of small KLS eddies and the exploration of their relation to hemolysis observed experimentally offers a fresh examination of the reasons for RBC trauma.

Returning to assumptions (iv) and (v), it is expected that cellular components of flow can influence turbulence in blood. For the experiments simulated, only washed red cells were used. In the case of whole blood, the effects of platelets and white cells should be negligible, since platelets and white cells are more than an order magnitude lower in number concentration than red cells and in blood they comprise a much smaller volume percent. Red cells comprise a high volume percent that will indeed affect turbulence.

However, red cells have the ability to tank tread and the property of a very low membrane bending modulus (1-3 x 10^{-13} ergs [84]). Therefore, calculation of the KLS based on Newtonian fluid properties will be valid for all of the simulations in this work since the suspensions are very dilute and can be considered homogeneous. (Details of eddy analysis are discussed in Appendix A).

2.5 Reynolds Stress Calculation

In Reynolds stress (RS) calculations in this work, it is assumed that the simulated systems were well mixed in turbulent flow. Therefore, cells are assumed to spend on average the same amount of time in any location inside of the flow field.

Reynolds stress calculations were performed for the Couette viscometer and the capillary tube configurations at a post-processing stage. For both capillary tube and Couette viscometer experiments several lines (called rakes in Fluent) were created through the model geometry. Rakes were created equally spaced and each rake had several points that were equally spaced. Then, Reynolds stresses were calculated in each point of each rake and eventually there were more than 1000 different calculated Reynolds stress values for both capillary tube and Couette viscometer. Time averaged velocity gradients at each point of every rake ($\tau_v = \mu * \frac{d\overline{U}_x}{dy}$ on rakes aligned with the y axis and $\tau_v = \mu * \frac{d\overline{u}_x}{dz}$ along rakes aligned in the z axis) yielded viscous stresses. The total stress, $\tau_t = \frac{r}{R} * \tau_w$, was found at each point and the Reynolds stresses were calculated by taking the difference between viscous and total stresses $\tau_{Re} = \tau_t - \tau_v$. Finally, the area averaged Reynolds stress, $<\tau_{Re}>$, was calculated by using

$$\langle \tau_{\mathrm{Re}} \rangle = \frac{\sum_{i=1}^{Nbins} \tau_{\mathrm{Re}_{r_i}} * \pi \left(r_i^2 - r_{i-1}^2 \right)}{\pi * R^2} \qquad \textbf{2.16}$$

where $\tau_{Re_{r_i}}$ is the Reynolds stress at point r_i, N_{bins}, is the number of points in each rake, and r_i is the distance of each point from the center of the capillary tube. For the Couette viscometer, rakes were created in the blue vertical plane shown in Figure 3.1(B). Calculations of area averaged viscous and Reynolds stresses were conducted similarly to the capillary tube, keeping in mind that the total stresses for the Couette viscometer were calculated as

$$\tau_{r\theta} = 2 * \pi * \Omega_i * \frac{R_i^2 * R_o^2}{R_o^2 - R_i^2} * \frac{1}{r^2} \qquad \textbf{2.17}$$

where Ω_i is the rotation rate of the inner cylinder, R_i is the radius of inner cylinder and R_o is the radius of outer cylinder.

3 Modelling Turbulent Flow and Cell Damage in a Couette Viscometer

Portions of this chapter have been reproduced from the following source. This paper has been published for publication in the Artificial Organs Journal:

- Ozturk, M., O'Rear, E. A., & Papavassiliou, D. V. (2015). Hemolysis related to turbulent eddy size distributions using comparisons of experiments to computations. Artificial Organs, 39(12), E227-E239. Doi: 10.1111/aor.12572.

3.1 Background

When RBCs are flowing through medical devices that are based on Couette flow, such as implantable rotary blood pumps, they can be affected by hemolytic and/or traumatic effects.[85] Therefore, a better understanding of behavior of blood and its constituents when they interact with these devices is possible by testing these devices to reduce blood damage and improve their design. [86] In general, Couette viscometers can provide high shear stresses with relatively short loading times, [22] but they have also been used for longer periods of exposure. The magnitude of the produced shear stress inversely depends on the gap width and proportionally depends on the relative speed of the two concentric cylinders. Concentric cylinder viscometer has commonly been used to study hemolysis in both laminar [22, 24, 37, 38, 87-90] and turbulent flow. [60] Moreover, it has been seen that a value of the threshold shear stresses in laminar and turbulent flow for hemolysis remains unsettled. Some of these studies are summarized below and also shown in Table 3.1.

When we review the studies of hemolysis in laminar Couette flow, Leverett et al. [90] used concentric cylinder viscometer in laminar flow to study effect of different

factors on blood damage which are centrifugal force, damage at the air-blood interface, viscous heating, relation between red blood cells and solid surfaces, and cell-cell interaction. Experiments were performed at shear stresses ranging from 500 – 4000 dyne/cm^2 and an exposure time of 2 minutes. As a result of experiments, damage was caused only by shear stress above the threshold shear stress of 1500 dynes/cm^2. A Taylor Couette viscometer was used to explore effect of laminar shear stress and exposure time on red blood cell damage in a recent study by Arwatz et al. [38] Hemolysis of human blood was investigated for shear stresses from 50 to 500 Pa and for exposure times of 60-300 s. Based on their results and previous work, a viscoelastic strain-based hemolysis model was fitted to their data. While they were observing hemolysis for shear stresses as low as 50 Pa, they did not observe a hemolysis threshold value. Couette flow was also used in the study of Klaus et al. [89] to measure hemolysis using porcine blood and hemolysis was not observed until shear stress of 400 Pa and exposure times of 400 ms. In a further study of Klaus et al., [88] porcine and human blood was sheared in a Couette viscometer to compare the effect of blood types on hemolysis and platelet reduction for shear stress ranges of 6.5 Pa – 400 Pa and exposure time of 400 ms. Hemolysis and platelet reduction were similar in both blood types except for higher hemolysis measurements in which high standard deviations were observed. Paul et al. [37] used Couette viscometer to measure hemolysis for exposure times of 25-1250 ms and shear stresses of 30 – 450 Pa. Hemolysis levels were increased largely for shear stresses $\tau \geq 425$ and exposure times $t \geq 620$ ms and hemolysis measurements were the same as hemolysis measurements of Klaus et al. [89] Boehning et al. [87] developed their laminar Couette shear flow based on the set up of Klaus et al. [88, 89], and Paul et al. [37] by using porcine

blood at four levels of shear stresses (24, 592, 702, and 842 Pa) and at two exposure times (54 and 873 ms). Experimental results showed a large increase of hemolysis for shear stresses above ~600 Pa at 873 ms. Heuser et al. [22] used Couette viscometer to shear porcine blood in a laminar flow field for exposure times less than 700 ms and shear stresses less than 255 Pa. Zhang et al. [24] examined hemolysis of ovine blood in a laminar Couette flow for exposure times of less than 1500 ms and shear stresses between 50-320 Pa and obtained slightly lower hemolysis values than Paul et al. [37]and Klaus et al. [89]

Although, Couette viscometers were used by several investigators to study hemolysis in laminar flow, hemolysis data in turbulent flow are rare. Therefore, it was quite a challenge for this study to find hemolysis data in turbulent flow. In this work, the Couette viscometer experiments of Sutera et al. [60] were simulated, where human erythrocytes were sheared for shear stresses from 100 to 4500 dynes/cm^2 and for exposure time of 4 minutes. [60] Large increase of hemolysis was observed for shear stresses above 2500 dynes/cm^2.

Table 3.1. A review of Couette viscometer studies for hemolysis

Reference for Couette experiment	Exposure time (s)	Shear stress ranges (Pa)	Shear stress threshold for RBC damage (Pa)	Flow field
Leverett et al. [90]	120	50 - 400	150	Laminar
Arwatz et al. [38]	60 - 300	50 - 500	-	Laminar
Klaus et al. [89]	0.4	6.5 - 400	400	Laminar
Paul et al. [37]	0.025 - 1.25	30 - 450	425	Laminar
Boehning et al. [87]	0.054 – 0.873	24 - 842	600	Laminar
Heuser et al. [22]	< 0.7	< 255	-	Laminar
Zhang et al. [24]	1.5	50 - 320	-	Laminar
Sutera et al. [60]	240	10 - 450	250	Turbulent

3.2 Methods

3.2.1 Geometry and Computational Domain

The Couette viscometer of Sutera and Mehrjardi[60] utilized a rotating inner cylinder and a stationary outer cylinder. The rotor was 10 cm in diameter, 5 cm long and the gap between the cylinders was 2.07 mm, which allowed a maximum shear stress of 450 Pa. Washed, human erythrocytes in phosphate buffered saline (PBS)/glucose at low hematocrit (2%) were exposed to turbulent flow for a period of 4 minutes. Only $1/32^{nd}$ of the whole viscometer has been modeled and simulated to reduce computational time [Figure 3.1].

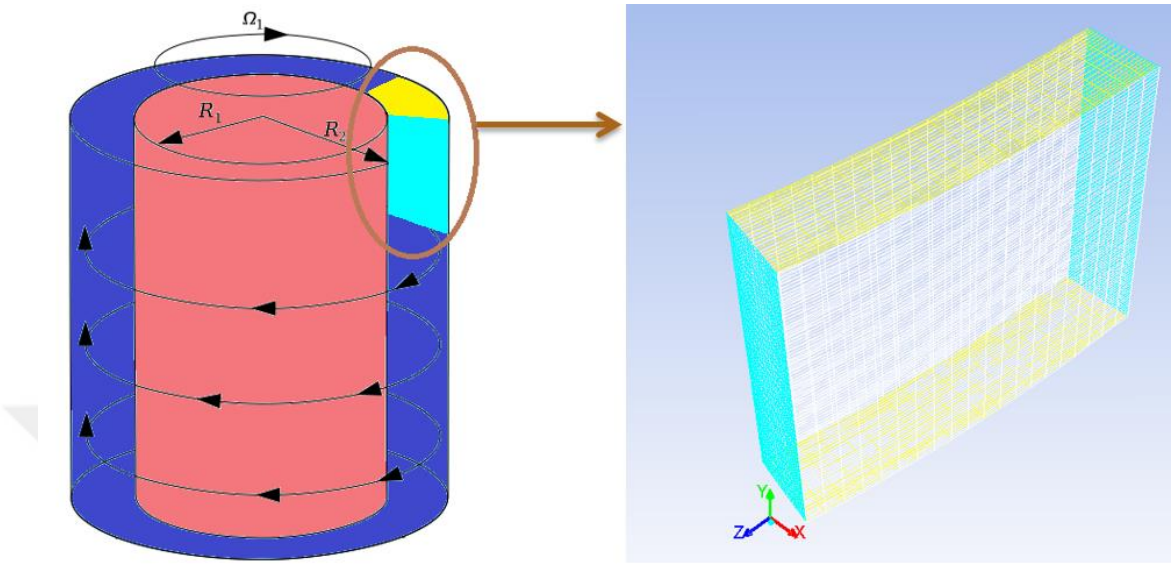

(A) (B)

Figure 3.1. (A): Couette Viscometer, (B): 3D model of 1/32nd of viscometer.

Using 1/32nd of the geometry was justified by considering the integral length scales in the computational domain when expressed in dimensionless viscous wall parameters. When walls are present in turbulent flow, it is customary to use dimensionless quantities that are based on the friction velocity, u^*, and the viscous length scale, l^*. The friction velocity is defined based on the fluid density, ρ, and the average wall shear stress, $\bar{\tau}_w$, as $u^* = \sqrt{\frac{\bar{\tau}_w}{\rho}}$, while the viscous length scale is calculated from the fluid kinematic viscosity, ν, and the friction velocity as $l^* = \frac{\upsilon}{u^*}$). The range of the integral length scales in wall turbulence is about 1000 in viscous wall units, while the dimensions of our computational domain in the azimuthal direction was from 2174 (for the lowest shear stress experiment, 50 Pa) to 6498 (for the highest shear stress experiment, 450 Pa. Both

values are more than twice the typical value of 1000, justifying the use of 1/32 of the viscometer in the azimuthal direction for the simulations.

3.2.2 Computational Mesh Development

Grids for the geometry of the Couette viscometer [Figure 3.1(B)] was created using the Fluent 14.0 and its preprocessing program ICEM CFD (Ansys, Pittsburgh, PA). The flow domain of the Couette viscometer was represented by using a $1/32^{nd}$ three dimensional model section of the experimental geometry, saving computational time while capturing the necessary flow features. Once a geometric shape had been prepared, meshing proceeded with formation of hexahedral elements throughout the entire geometry. After a computational mesh was created in ICEM CFD, it was imported into Fluent for solution of the incompressible Navier-Stokes equations. Mesh independence of the models was tested by refining the grid in regions of high mean velocity gradient until the percent difference for pressure loss and velocity profile at multiple cross sectional cuts between a more and less refined simulation solution was less than 3%. The final mesh used for the Couette viscometer included 33,600 cells and 37,000 nodes with an average grid cell size of $4x10^{-3}$ mm^3. Grid independence analysis was performed for several parameters to check mesh integrity and independence. Distributions of KLS and mean velocity magnitude results are shown in Figure 3.2. It can be seen from Figure 3.2 that velocity and KLS values in the Couette viscometer were independent of mesh size.

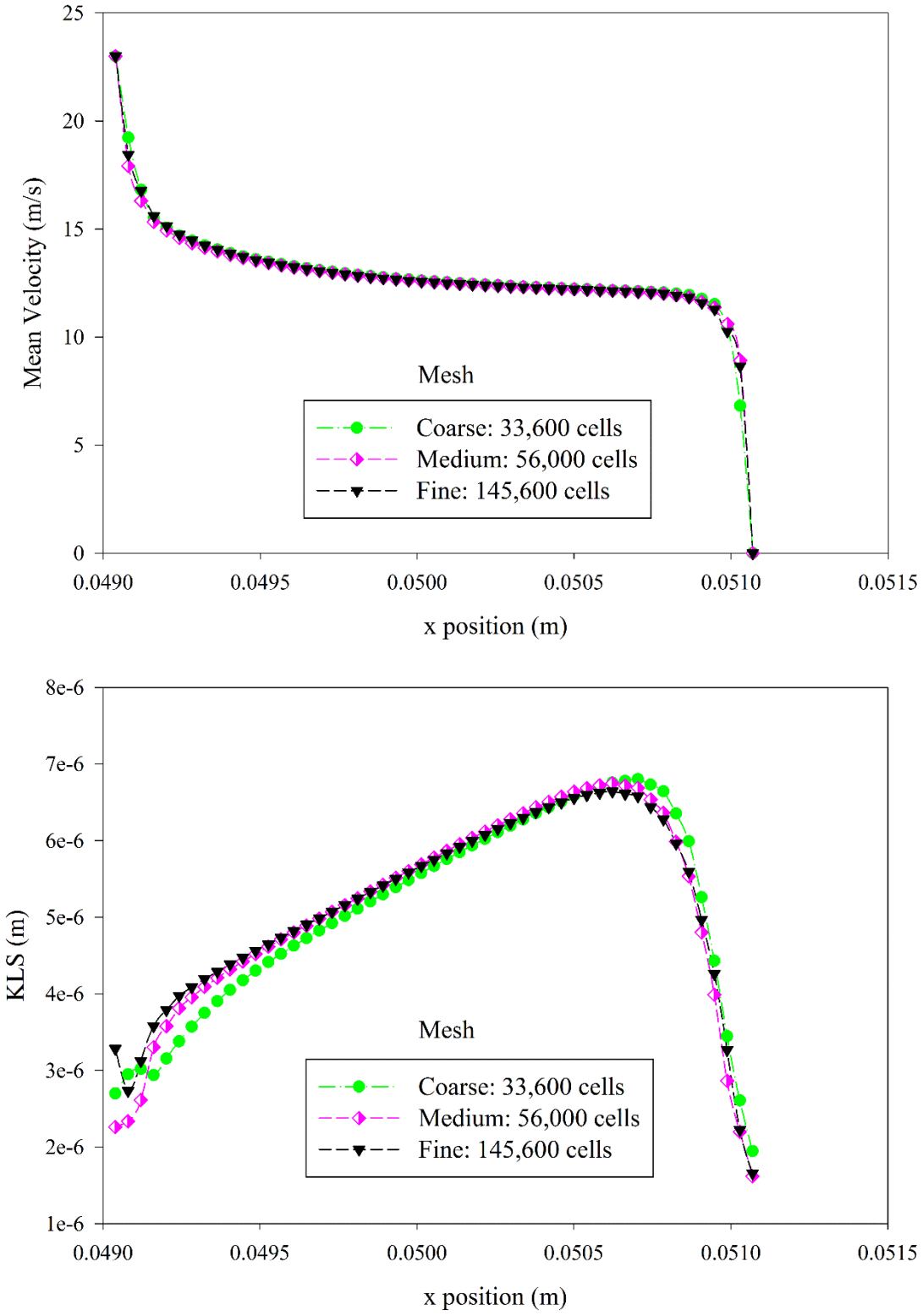

Figure 3.2. Top: Grid independence analysis for velocity. Bottom: Grid independence analysis for KLS. The k-ε model was used with enhanced wall functions.

3.2.3 Flow Simulations

Couette viscometer simulations were performed with symmetry boundary conditions at the top and the bottom of the domain (axial direction) along with periodic boundary conditions in the azimuthal direction. Also, no-slip boundary conditions were specified for the inner and outer walls of the viscometer (radial direction). The fluid properties for all simulations of the Couette viscometer consisted of a Newtonian rheological model with a viscosity of 0.001 Pa.s and a density of 998 kg/m^3 [60]. The viscosity used in the simulations is not of physiological value, because this work involved simulations of the experimental study. Therefore, conditions representing the conditions of the actual experiments have been used. This included the geometries (dimensions, diameters, etc.), as well as the fluid properties and flow conditions. Therefore, the viscosity reported in the experimental paper was used for the Couette simulations. [60] The Newtonian and homogenous fluid assumptions are valid, since the suspensions used in the simulated experiments contained washed red blood cells.

Simulations were performed with the finite volume based Fluent simulator, using the 2nd order upwind discretization scheme, the *presto* interpolation scheme for pressure, and the *simple* scheme for pressure-velocity coupling. In the beginning of the flow simulations of the Couette viscometer, a slow rotational velocity was assigned to the inner wall (such that the flow remained laminar), then the velocity was slowly increased *in silico* until the resulting shear stress equaled one of the experimental shear stress values reported by Sutera and Mehrjardi. [60] After the rotational rate attained a value high enough to yield turbulent flow, the realizable k-ε model and enhanced wall functions, which increases model capability near the wall, were applied. The procedure of increasing

the rotation rate of the inner cylinder was repeated until all seven cases of different shear stress values (50-450 Pa) of the Sutera and Mehrjardi [60] experiments had been simulated (see Table 3.2). Simulations were considered converged when residuals for the velocity components, the continuity equations, and the equations of k, ε, and ω of the turbulence models fell below $1x10^{-5}$. The Reynolds number based on the inner cylinder velocity for Couette flow was determined by using the rotational velocity of the inner cylinder, Ω_i, the radius of the inner cylinder, R_i, the gap width, h, and the kinematic viscosity, ν, as $Re = \frac{\Omega_i R_i h}{v}$, giving values of 13390 (for lowest shear stress, 50 Pa) to 47382 (for highest shear stress, 450 Pa). Sutera and Mehrjardi [60] stated that when the Taylor number (Ta) is higher than 400, the flow will be turbulent, therefore the Ta was also determined for the Couette viscometer as $Ta = \frac{\Omega_i R_i^{1/2} h^{3/2}}{v}$. Calculated Taylor number values for the Couette viscometer range from 2725 (for lowest shear stress, 50 Pa) to 9641 (for highest shear stress, 450 Pa) (shown in Table 3.2), much higher than the critical Ta. Thus, flow in the Couette viscometer is fully turbulent.

Table 3.2. Model conditions for Couette viscometer experiments

Shear Stress (Pa)	Rotation Rate (rad/s)	Experimental Hemolysis (%)	Taylor Number	Reynolds Number	KLS Range (μm)
50	130	1.403	2725	13391	4 – 16
100	196	1.1364	4108	20189	3 – 13
150	240	2.5448	5030	24721	2 – 12
200	300	4.2883	6288	30901	2 – 11
250	340	11.0547	7126	35022	2 – 11
350	400	40.3351	8383	41202	2 – 11
450	460	85.3609	9641	47382	1 – 11

Selection of turbulence model (k-ε or k-ω SST) was based on comparison to appropriate data obtained through direct numerical simulation (DNS) results and available in the literature. [91] The turbulence models for the Couette viscometer simulations were compared by using the DNS data of Pirro et al. [91] who simulated for the first time the Taylor-Couette flow in fully turbulent flow. Mixed spatial discretization was used in their computational code that was the extension of the numerical method of Luchini and Quadrio. [92] Pirro et al. [91] calculated statistical quantities to compare their results with planar turbulent flow at same Reynolds number while also completing the deficiency of current experiments and observed large-scale rotating structures as a main difference to planar flow. Couette viscometer simulations were simulated by using both k-ε and k-ω SST turbulence models and the simulation results and the DNS data of Pirro et al. [91] were matched at corresponding friction Reynolds number, Re_τ, which was

defined as $Re_\tau = \frac{u^* * \frac{h}{2}}{\upsilon}$, where $u^*$is the friction velocity, h is the gap width, and ν is the kinematic viscosity. After simulations were performed, the mean velocity profiles for the near wall region were calculated using the dimensionless wall parameters. The dimensionless distance from the wall, y^+, was calculated based on distance from wall, *Y,* and the viscous length scale, l^*, as $y^+ = \frac{Y}{l^*}$. The dimensionless velocity, u^+, was calculated as $u^+ = \frac{<U>}{u^*}$, where <U> is the mean velocity. The mean velocity profile for the Couette viscometer is plotted with the DNS data [91] in Figure 3.3. It can be seen from Figure 3.3 that using the k-ε model in the computation of the flow domain can describe the near-wall region better than the k-ω SST model.

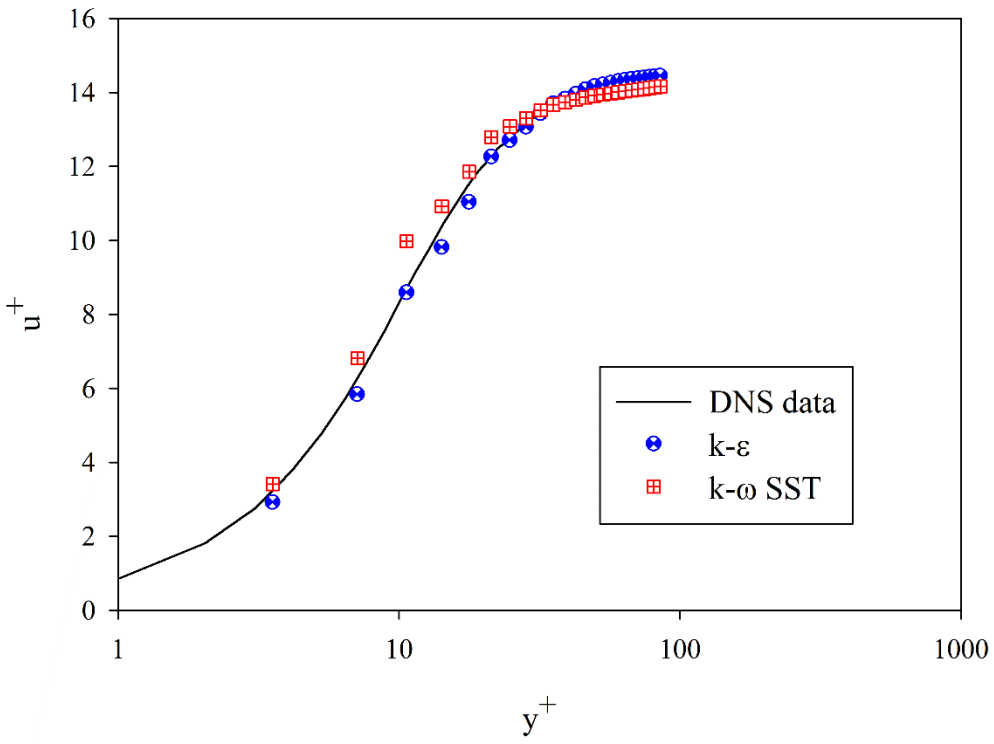

Figure 3.3. Couette viscometer mean velocity profiles using both k-ε and k-ω SST models near wall for the DNS data of Pirro et al.[91] at Re_τ =180 with Ω_i=94 rad/s and τ_w= 30.7 Pa.

After determination of the root mean square error for both models, the k-ε model was selected for simulation of the Couette experiments (Table 3.3).

Table 3.3. Root mean square errors for the Couette viscometer experiments

Root Mean Square Error	Couette Viscometer
k-ε Model	0.39
k-ω SST Model	0.65

3.3 Results and Discussion

3.3.1 Relation between Eddy Size Distribution and KLS

For the Couette viscometer, KLS values were first calculated on a vertical plane [blue plane in Figure 3.4]. The KLS values were the same when moving circumferentially, along the yellow plane in Figure 3.4. The calculated KLS values had a range between 1 μm and 11 μm for the highest average shear stress experiments (450 Pa), while the maximum value of KLS was up to 16 μm for the lowest average shear stress experiments (50 Pa). The complete range of KLS and experimental conditions are shown in Table 3.2

The time-averaged spatial distribution of KLS values in a vertical plane (shown in red rectangle) is shown in Figure 3.4 for the Couette viscometer for the highest wall shear stress experiment.

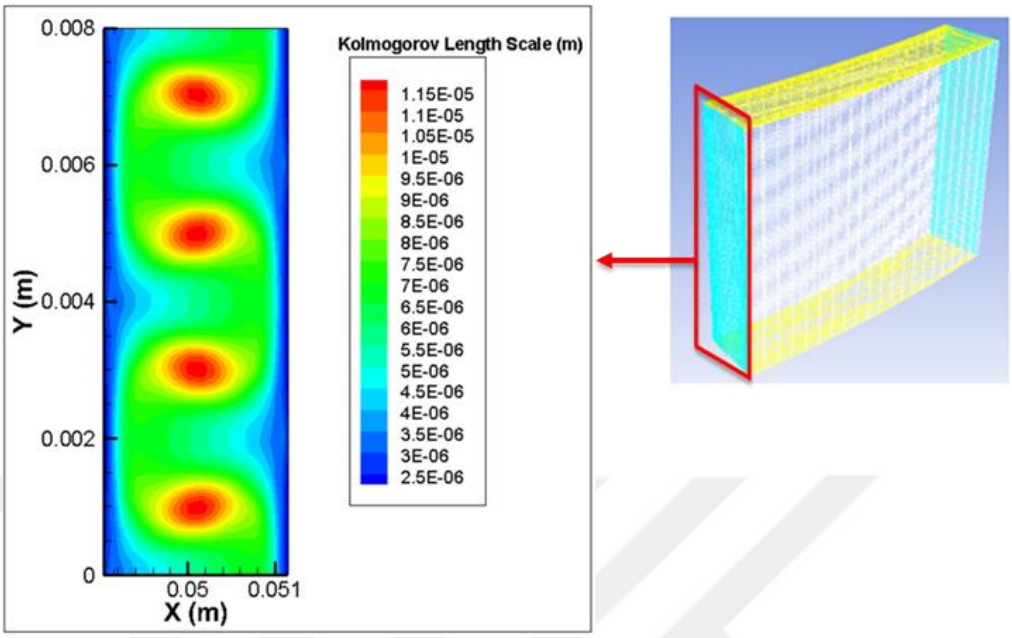

Figure 3.4. KLS values on the blue vertical plane of Couette viscometer by using k-ε turbulence model. The inner cylinder, at x = 0 is rotating at Ω_i = 460 rad/s and τ_w= 450Pa.

It can be seen from Figure 3.4 that KLS values reach a maximum value at distinct locations in the Couette viscometer with lower values near the wall.

Estimation of the eddy sizes based on the Kolmogorov length scale provided a representative eddy size distribution. Calculations were performed for 7 experiments of Couette viscometer as seen in Table 3.2. Results showed that the size distributions shifted to smaller values with simulations for increasing shear stress [Figure 3.5]. This shift reflects greater energy dissipation with higher angular velocities of the Couette viscometer.

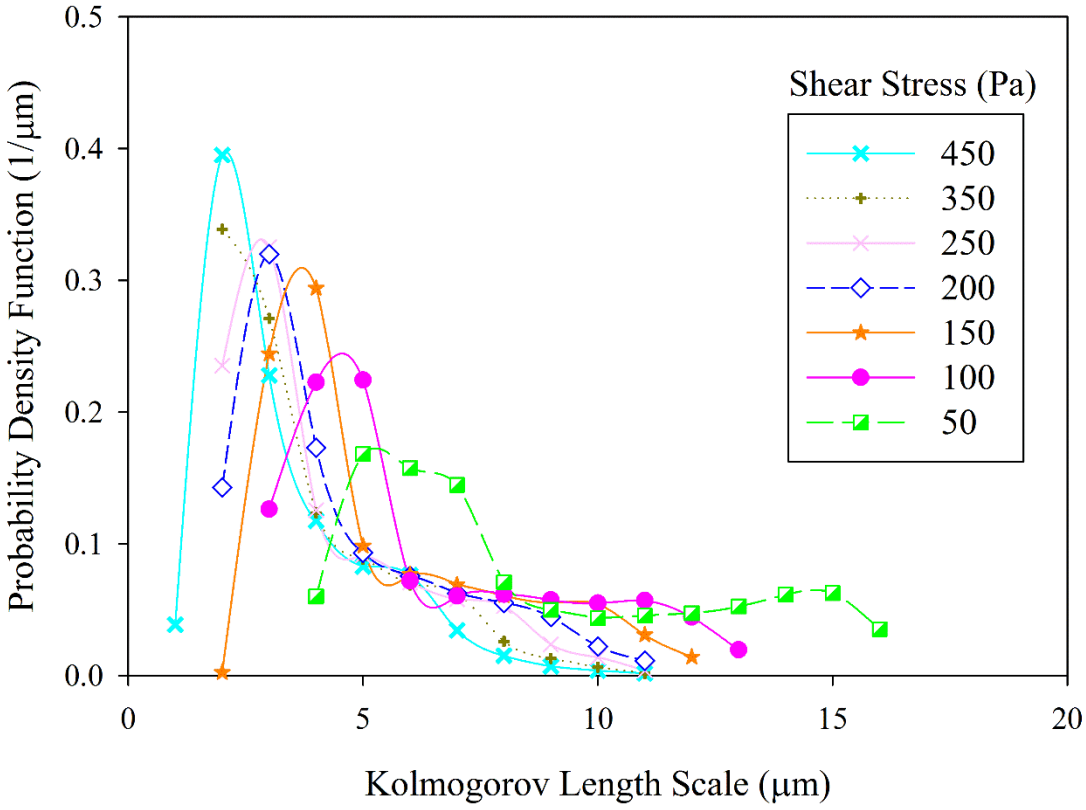

Figure 3.5. Probability distribution of KLS values in the Couette viscometer for all experiments (450 Pa – 50 Pa). The area under the each curve is equal to 1.

The increased presence of smaller eddies occurs in conjunction with greater hemolysis. This finding suggests that blood damage in turbulent flow could be predicted by looking more closely at Kolmogorov length scales as proposed previously by others. In the Couette viscometer, higher shear stresses show sharper eddy distributions [Figure 3.5]. When the shear stress decreases, the eddy distributions are flatter, e.g., at 50 Pa the KLS are between 5 and 8 μm [Figure 3.5].

3.3.2 The Effect of Eddy Surface Area on Hemolysis

The total surface area of the KLS-sized eddies per unit volume has been calculated for the seven experiments in the Couette viscometer as a function of the KLS values. Analysis to find a relation between eddy area and hemolysis continued by combining experimental results of each experiment of the Couette viscometer. A relationship between eddy surface area per volume and hemolysis is shown in Figure 3.6 for the Couette viscometer simulation. Please note that for every figure of eddy area, eddy number, and eddy volume (both cumulative and not cumulative), each data point corresponds to observed hemolysis reported in the experiment of Sutera et al. [60] (% hemolysis values were digitized from original paper, as is shown in Table 3.2), while the eddy area (or eddy number, or eddy volume) for the specified KLS size was found from simulation of that experiment. The lines are plotted to guide the eye over the data points.

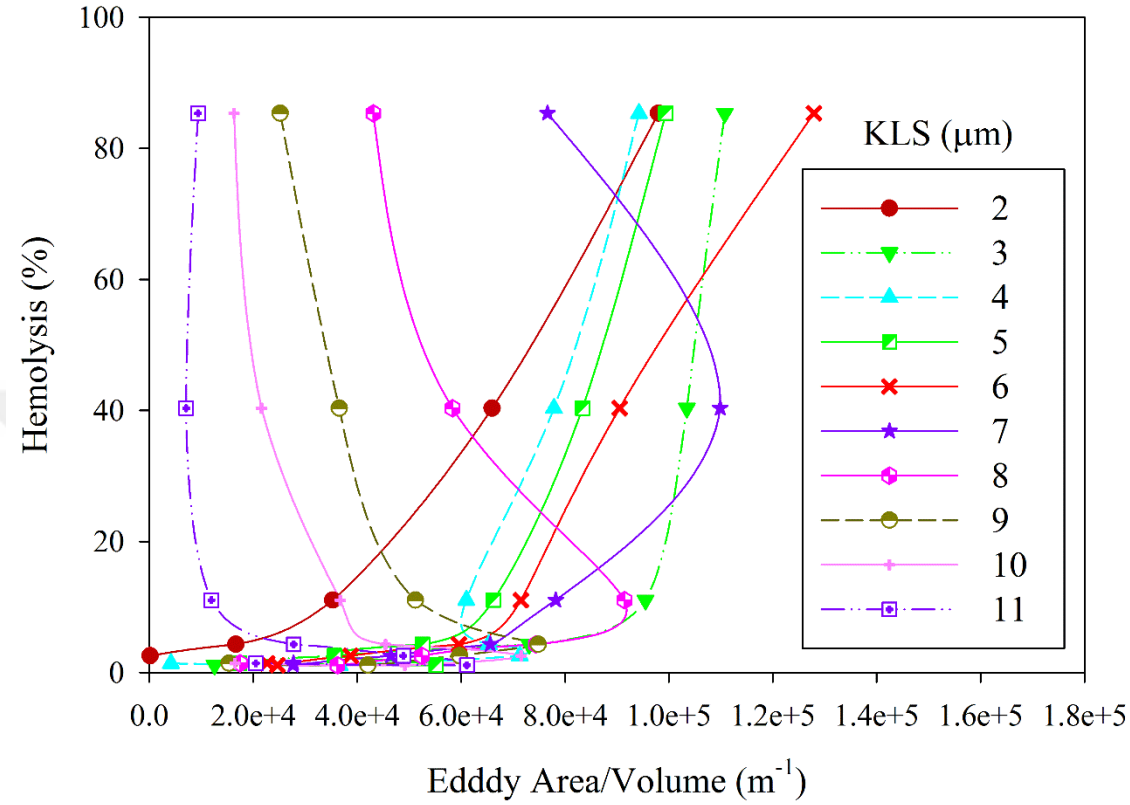

Figure 3.6. Hemolysis as a function of normalized eddy surface area in the Couette viscometer (experimental data from Sutera et al. [60]).

It can be seen from Figure 3.6 that a transition in the shape of these lines occurs as KLS value goes from 6 to 8 µm. For KLS above 6 µm, the lines curve back and up, suggesting no apparent dependence of hemolysis on the presence of eddies in this flow field.

Damage as measured by hemolysis appears to result from eddies below a certain size. It appears from Figure 3.6 that the critical eddy size is 6µm for the Couette viscometer. However, given the uncertainty associated with the k-ε model, as discussed in Section 2.5, a more meaningful way to interrogate the data is to explore the cumulative data rather than data binned in KLS bins of 1µm. In order to examine the cumulative effect of all eddies with a size less than a critical value, the KLS eddy surface area was

summed up as the KLS values increased. The cumulative sum of eddy surface area values versus % hemolysis is shown in Figure 3.7

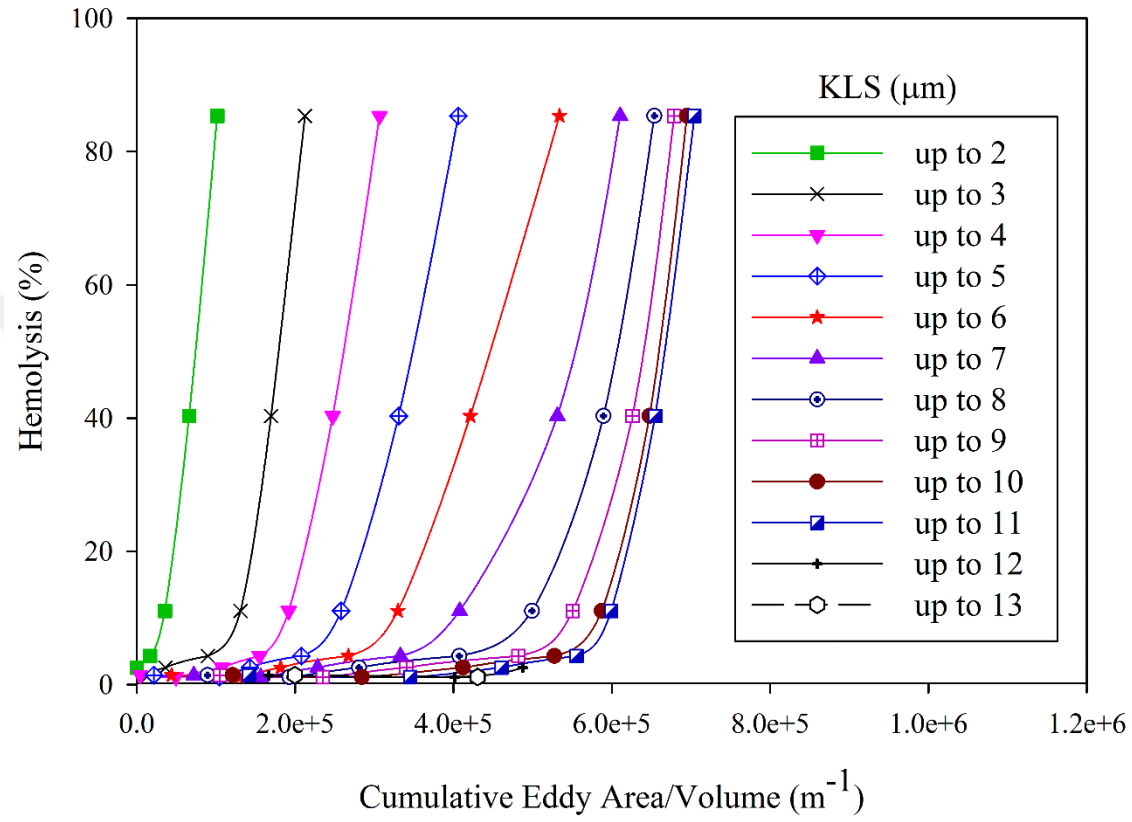

Figure 3.7. Hemolysis as a function of cumulative eddy surface area in the Couette viscometer.

It is clear from Figure 3.7 that hemolysis increases with increasing KLS eddy area per volume. Also note that, for higher KLS values, the curves begin to overlap with each other, the data almost collapse for eddies larger than 10 μm in the Couette viscometer.

3.3.3 The Effect of Eddy Number on Hemolysis

The total number of the KLS-sized eddies per unit volume has been calculated for the seven experiments in the Couette viscometer as a function of the KLS values. Relation between eddy number and hemolysis was found by calculating and combining eddy

numbers for each experiments of Couette viscometer (Table 3.2). A relationship between eddy number per volume and hemolysis is shown in Figure 3.8.

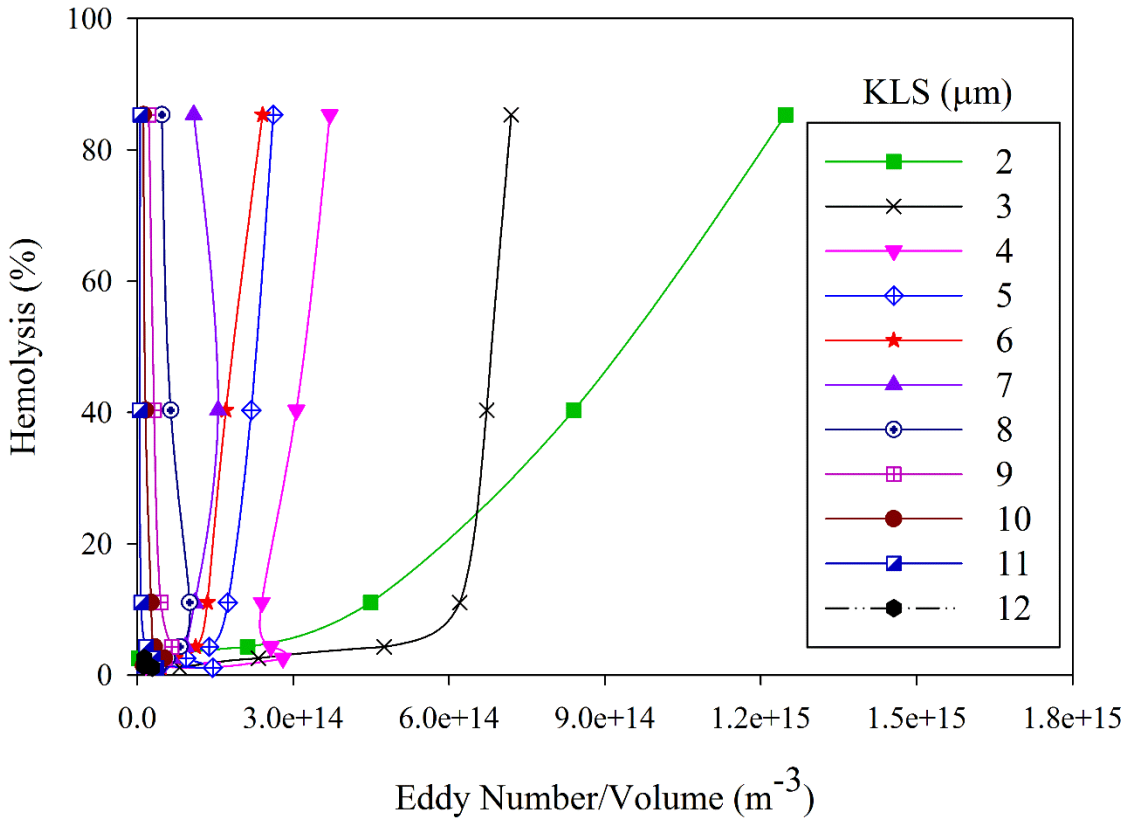

Figure 3.8. Hemolysis as a function of eddy number in the Couette viscometer.

Similar with eddy area, eddy number also shows transition in the shape of the lines as KLS value goes from 6 to 8 µm although the effect is not as apparent as in Figure 3.6 for area. For KLS above 6 µm, the lines curve back and up, suggesting no apparent dependence of hemolysis on the presence of eddies in this flow field.

Moreover, the cumulative effect of all eddies with a size less than a critical value was also examined for the eddy number by summing the KLS eddy numbers as the KLS values increased. The cumulative sum of eddy number values versus % hemolysis is shown in Figure 3.9.

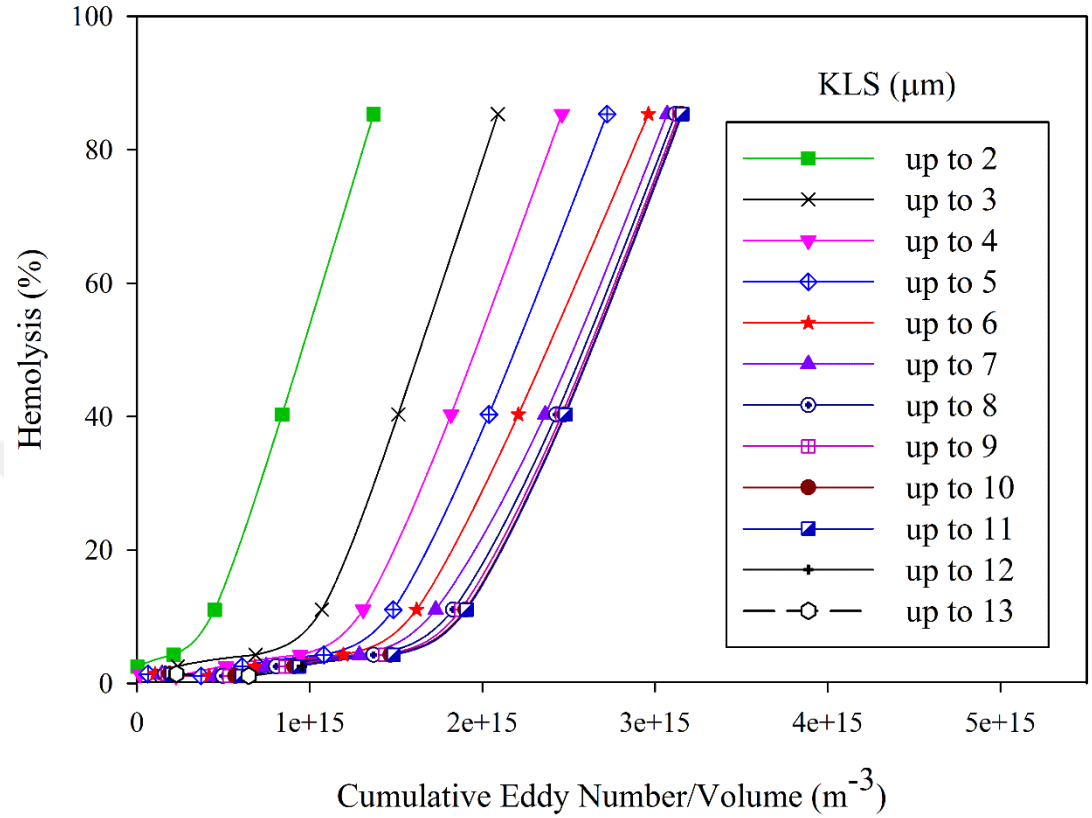

Figure 3.9. Hemolysis as a function of cumulative eddy number in the Couette viscometer.

It is clear from Figure 3.9 that hemolysis increases with increasing KLS eddy number per volume. Also, similar with eddy area, curves start to overlap for higher KLS values. For example, overlapping can be seen clearly for KLS ≥ 10 μm which is supporting the critical KLS size of 10 μm as determined by observations of Figure 3.7 in the previous section.

3.3.4 The Effect of Eddy Volume on Hemolysis

Same as in eddy area and eddy number, the total eddy volume of the KLS-sized eddies per unit volume has also been calculated for the seven experiments in the Couette viscometer as a function of the KLS values. Eddy volumes for each experiment of each KLS value were calculated and then combined with other experiments of Couette

viscometer (Table 3.2). Eddy volume per volume and hemolysis relationship is shown in Figure 3.10.

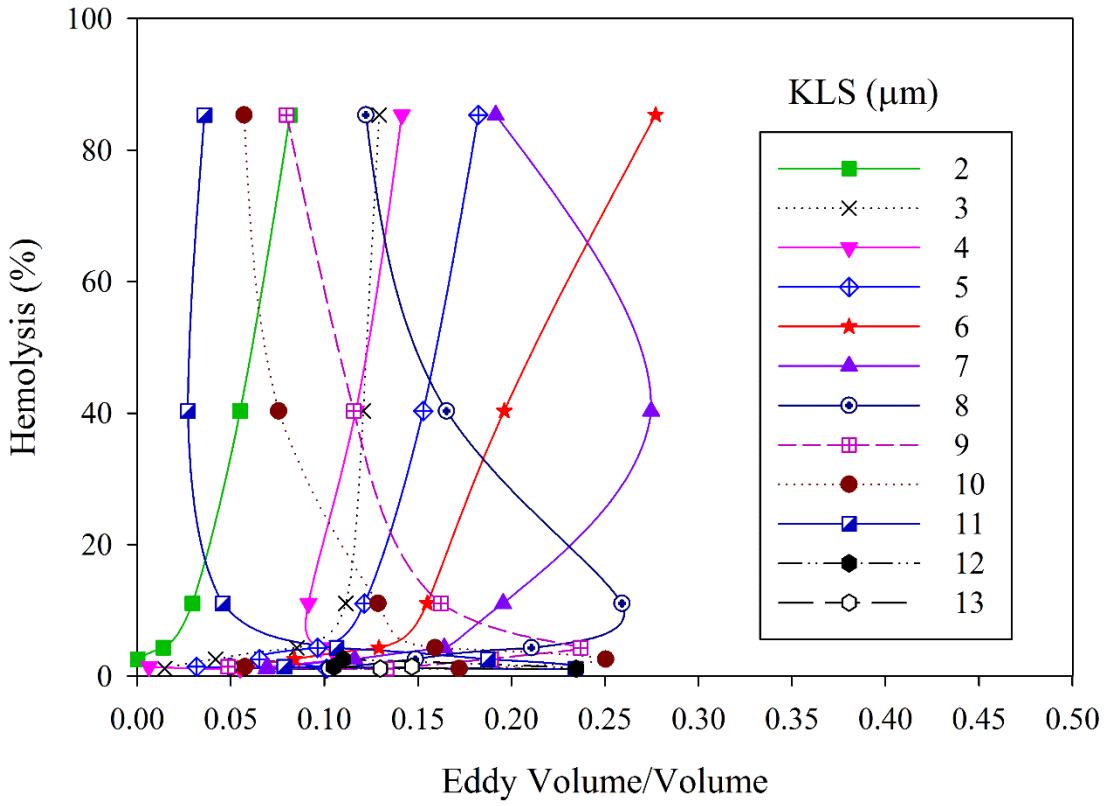

Figure 3.10. Hemolysis as a function of eddy volume in the Couette viscometer.

It can be seen from Figure 3.10 that again line shapes change when we go from smaller to larger KLS values. Curving back of the lines can also be seen for KLS above 6 μm, which also supports our previous plots suggesting no apparent dependence of hemolysis on the presence of such eddies in this flow field.

Additionally, the cumulative volume and hemolysis relation was also examined, in a similar manner to the eddy area and eddy number calculations. The cumulative sum of eddy volume values versus % hemolysis is shown in Figure 3.11.

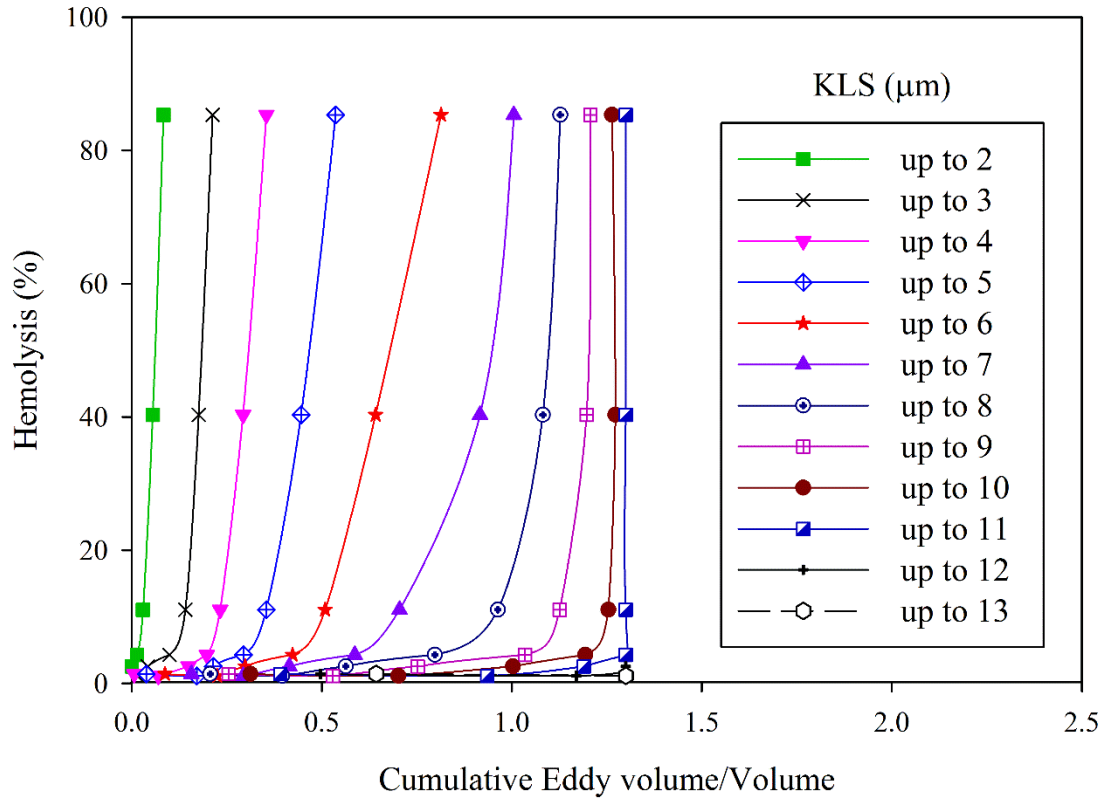

Figure 3.11. Hemolysis as a function of cumulative eddy volume in the Couette viscometer.

As can be seen from Figure 3.11, hemolysis increases with increasing KLS eddy volume per volume. Please note that, eddy volume does not show overlapping for larger KLS values. Instead, lines tending to become vertical suggest little or no effect on hemolysis for larger KLS values.

3.3.5 Reynolds Stress Calculations and Threshold Analysis

Reynolds stress calculations were also performed for 7 experiments of the Couette viscometer [60] as seen in Table 3.2. With varying amounts of hemolysis levels (1% - 85%) using the Couette viscometer, exploring the existence of a critical (or threshold) value provided a perspective to the importance of Reynolds and viscous stresses for

hemolysis. Experimental % hemolysis values were obtained from the original work of Sutera and Mehrjardi [60] (Table 3.2). The spatial distributions of Reynolds Stress were found for each experiment of the Couette viscometer. Contours of constant stress were mapped for a given experiment and *the threshold Reynolds Stresses were taken to be on the contour corresponding to the contour level enclosing a volume percent of the flow domain equal to the percent hemolysis*. A histogram of results (Figure 3.12) showed that for the highest shear stress experiment (450 Pa), the threshold Reynolds Stress value was 417 Pa (shown with red color in Figure 3.12), which means that 85% (hemolysis level of 450 Pa experiment) of the spatial distribution of Reynolds Stress was above this value.

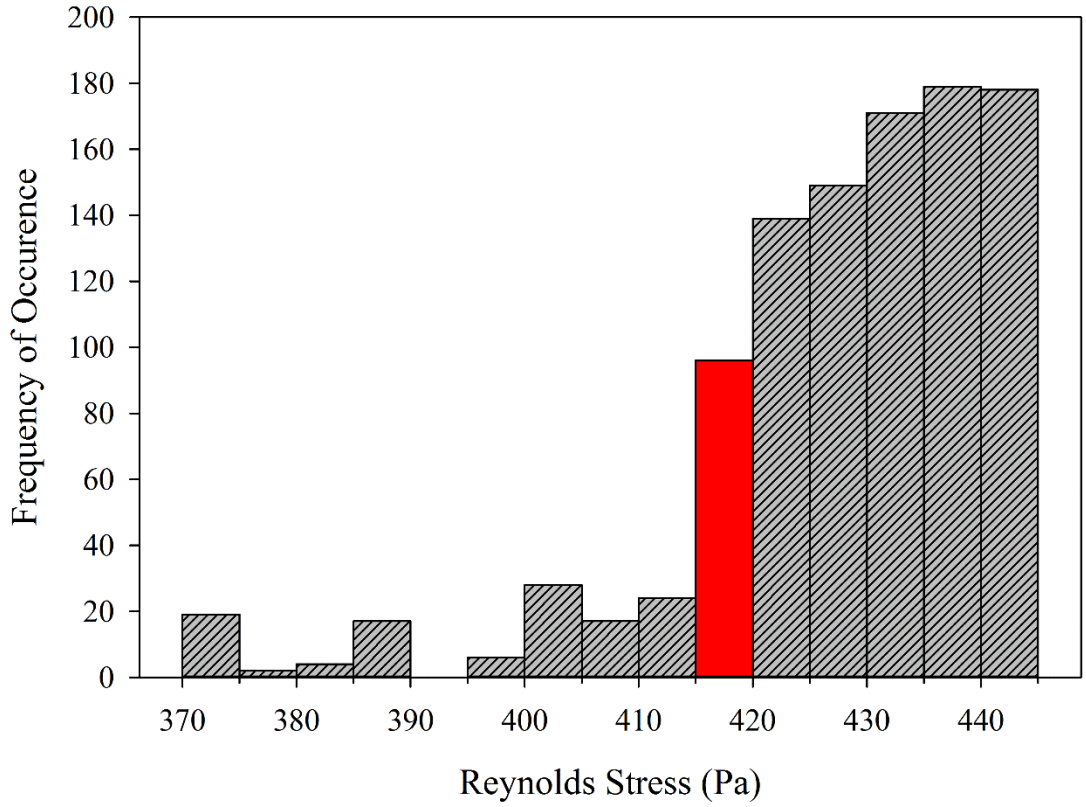

Figure 3.12. Distribution of Reynolds stresses in the Couette viscometer for 450 Pa. There were a total of 1071 mesh points examined on 21 different rakes in the Couette viscometer.

When the next highest shear stress experiment (350 Pa) was observed, it was seen that the threshold Reynolds Stress value was 336 Pa, which is lower than the threshold value of the previous experiment (450 Pa). The same analysis was repeated for the entire sequence of lower shear rate experiments (350 Pa -50 Pa) and the frequency plots are shown in Figure 3.13.

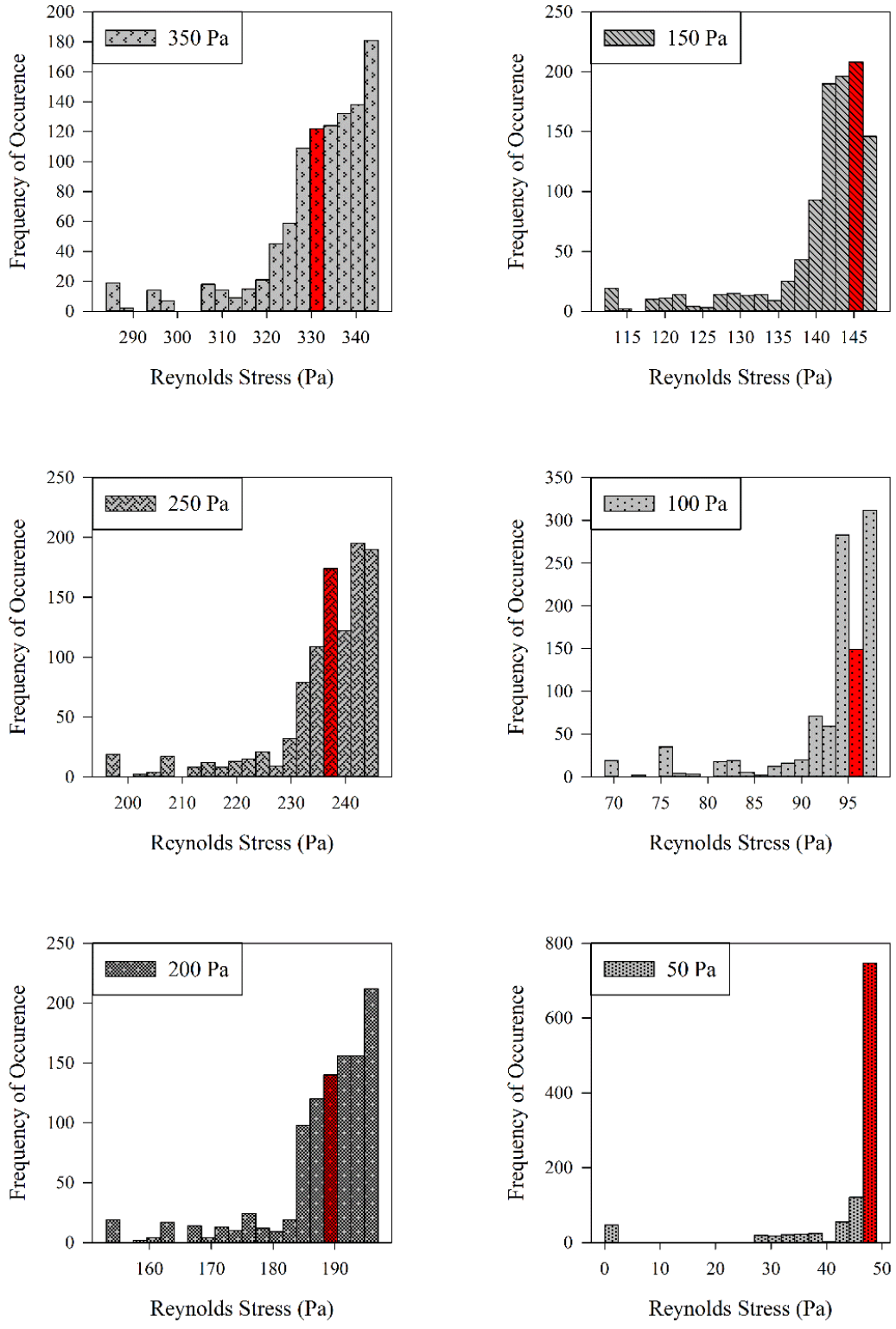

Figure 3.13. Distribution of Reynolds stresses in Couette viscometer for all experiments (450 Pa – 50 Pa). There were a total of 1071 mesh points examined on 21 different rakes in the Couette viscometer.

As can be seen from Figure 3.13 that the threshold Reynolds stresses shifted continually toward the lower end of the frequency plots. Threshold Reynolds stress values for the other six experiments (350-50 Pa) changed from 336 to 49 Pa.

When all the threshold Reynolds stress values are compared for Couette viscometer, it can be seen that results (Figure 3.14) for Reynolds stress, threshold values stretched over an order of magnitude.

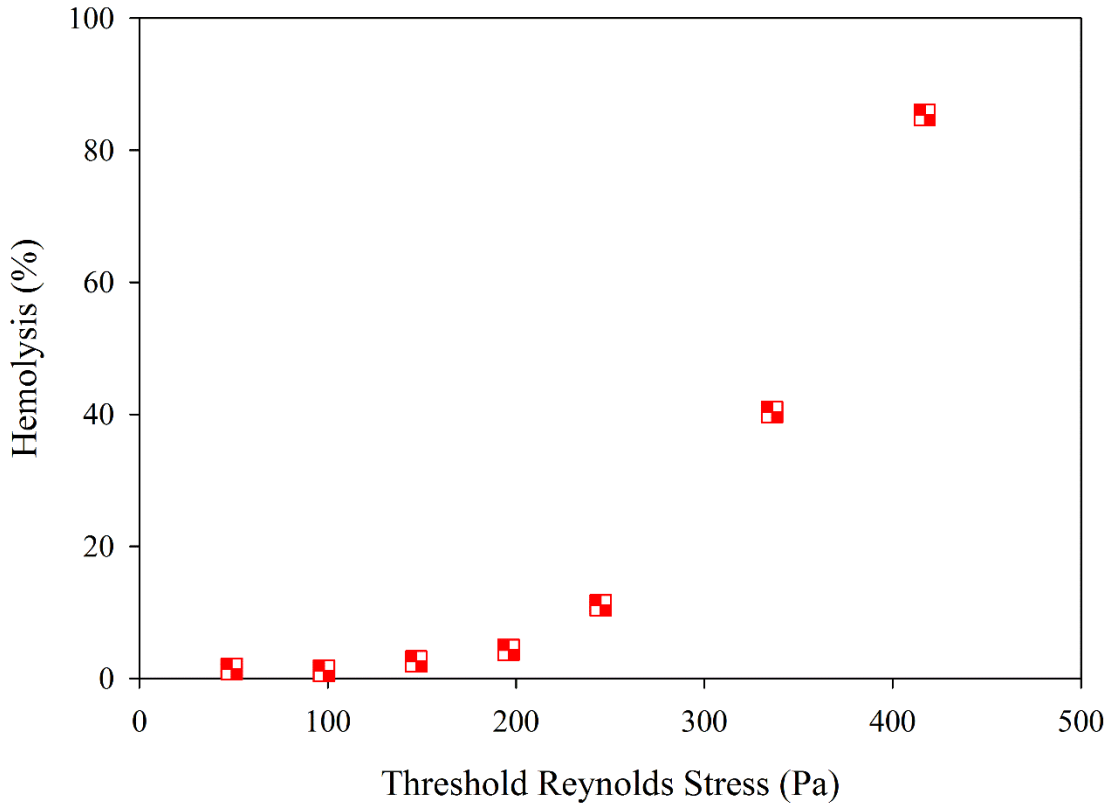

Figure 3.14. Estimated values of critical Reynolds stresses in the Couette viscometer for all the experiments (450 to 50 Pa).

If Reynolds stress were critical for hemolysis, one might expect to see a common value above which hemolysis is found, given that the exposure time of the RBCs in the Couette viscometer experiments was 4 min for all cases. However, results show that there was not a critical Reynolds stress leading to hemolysis (Figure 3.14). For example, for the 200 Pa experiment, the critical Reynolds stress value was 196 Pa. However, in the 150 Pa experiment, the critical Reynolds stress value was 147 Pa. If we rely on the 200 Pa experiment, we accept the threshold Reynolds stress value for hemolysis to be 196 Pa. When we look at the 150 Pa experiment, we would expect that there should not be any hemolysis at 150 Pa. When the other experiments are considered in the same way, it can be seen that there is not a common value of critical Reynolds stress for all experiments.

3.3.6 Viscous Stress Calculations and Threshold Analysis

Viscous stress threshold analysis for the Couette viscometer was performed the same way as the Reynolds stress threshold analysis. Viscous stress calculation does not contain viscous stresses in or between turbulent structures. They were calculated from time averaged velocity gradients on several locations in the domain from $\tau_v = \mu * \frac{d\overline{U}_x}{dy}$ on rakes aligned with the y axis and $\tau_v = \mu * \frac{d\overline{U}_x}{dz}$ along rakes aligned in the z axis. For each experiment of the Couette viscometer, the distribution of viscous stresses was found. Then depending on the hemolysis level of each experiment, the threshold viscous stresses were found. A histogram of results (Figure 3.15) showed that for the highest shear stress experiment (450 Pa), the threshold viscous stress value was found to be 1.2 Pa (shown with red color in Figure 3.15), which means that 85% (hemolysis level of 450 Pa experiment) of the spatial distribution of Reynolds stress was above this value.

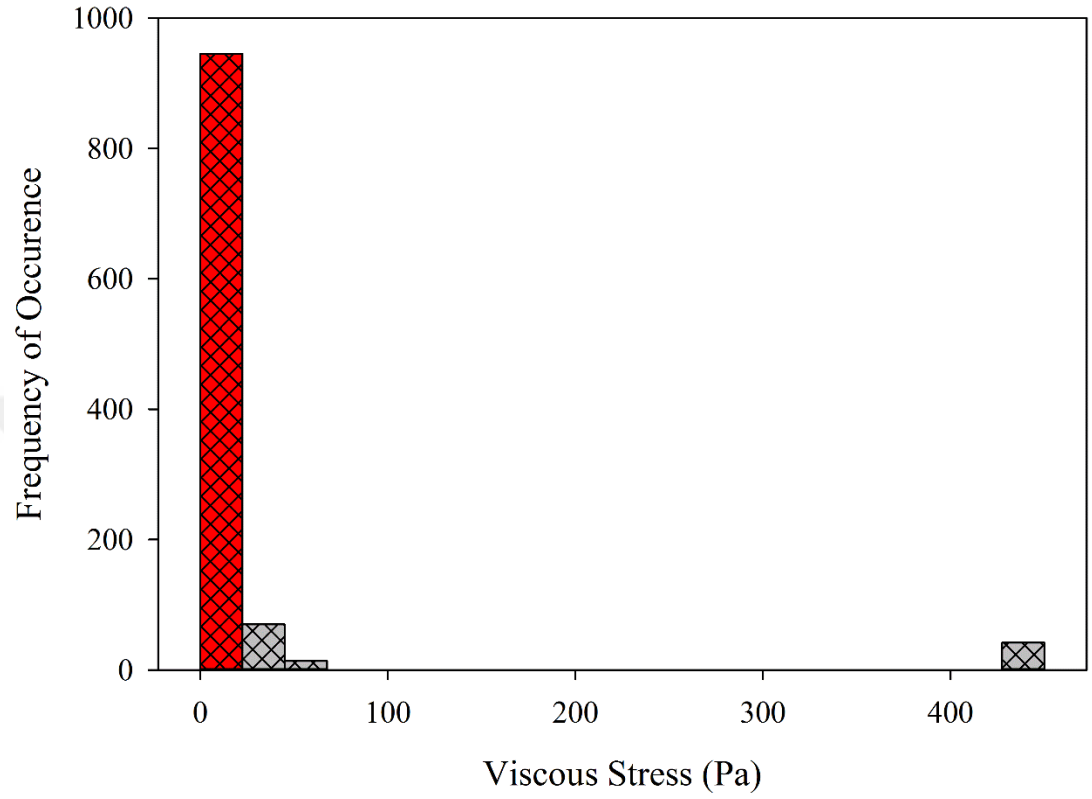

Figure 3.15. Distribution of viscous stress in Couette viscometer for 450 Pa. There were a total of 1071 mesh points examined on 21 different rakes in the Couette viscometer.

The same analysis was repeated for the entire series of lower shear rate experiments (350 Pa -50 Pa) and the frequency plots are shown in Figure 3.16. It can be seen from Figure 3.16 that the threshold viscous stresses were also shifted continually toward the lower end of the frequency plots similar to threshold Reynolds stresses.

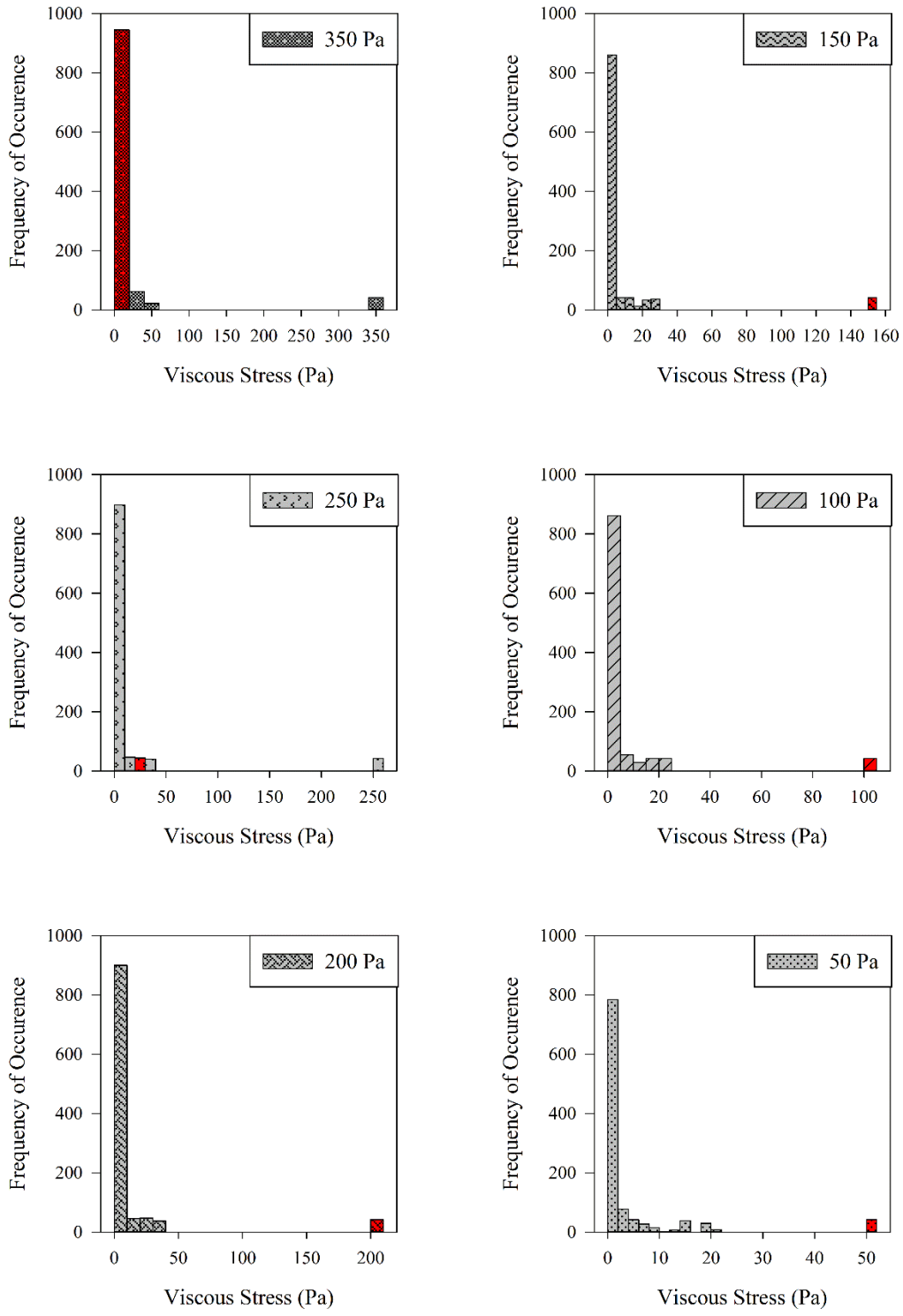

Figure 3.16. Distribution of viscous stresses in Couette viscometer for all experiments. There were a total of 1071 mesh points examined on 21 different rakes in the Couette viscometer.

When all the threshold viscous stress values are compared and plotted together for Couette viscometer, it can be seen that viscous stress threshold values are also different for each experiment (Figure 3.17). As in the Reynolds stress, if viscous stress were critical for hemolysis, there should be a common value for a critical viscous stress above which hemolysis occurs. It should further be noted that these stress levels are below thresholds known for laminar flow experiments.

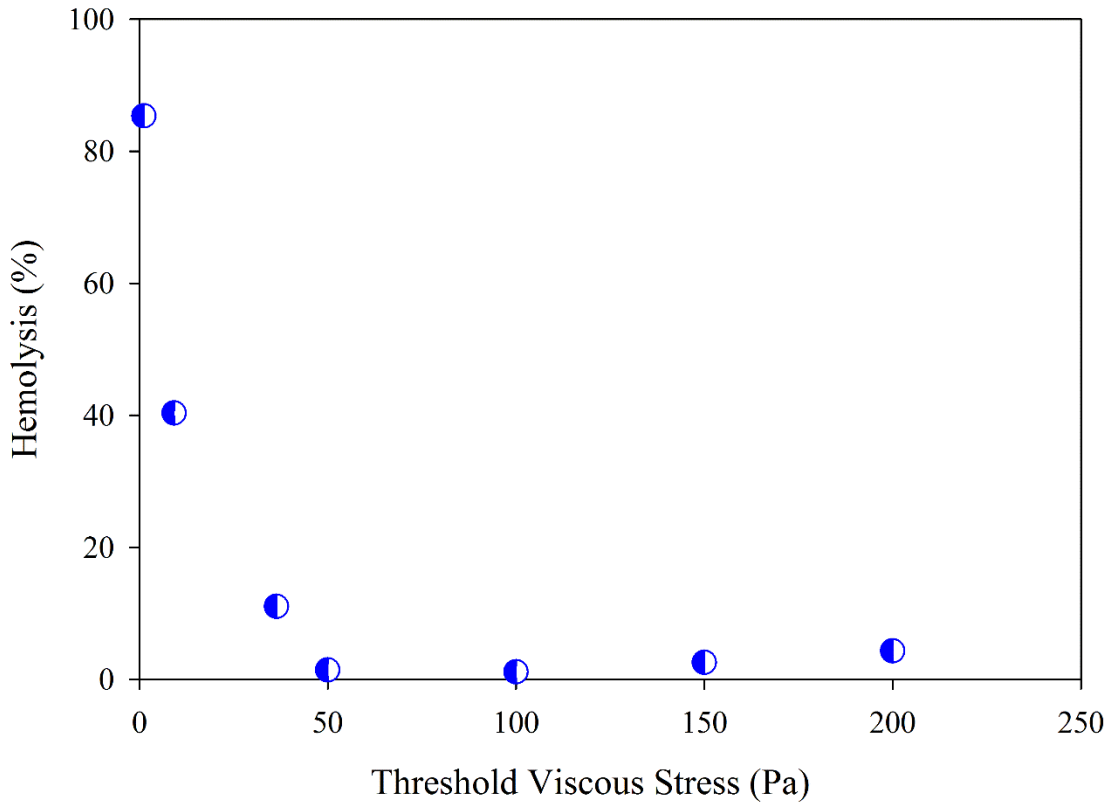

Figure 3.17. Distribution of viscous stresses in Couette viscometer for all experiments (450 to 50 Pa).

The threshold analysis of both Reynolds stress and viscous stress showed that the threshold stress was changing in each different experiment in the Couette viscometer.

3.4 Summary

The results presented up to now indicate that Reynolds stress or viscous stress cannot be used as a measure for hemolysis prediction, while KLS seem to be promising. When KLS smaller than about 10 μm exist in the flow, hemolysis is observed. Based on these findings, we move to examine different experimental settings to confirm these results.

4 Modelling Turbulent Flow and Cell Damage in a Capillary Tube

Portions of this chapter have been reproduced from the following source. This paper has been published for publication in the Artificial Organs Journal:

- Ozturk, M., O'Rear, E. A., & Papavassiliou, D. V. (2015). Hemolysis related to turbulent eddy size distributions using comparisons of experiments to computations. Artificial Organs, 39(12), E227-E239. Doi: 10.1111/aor.12572.

4.1 Background

Capillary tubes have also been used to study hemolysis in biomedical practice with the advantage of giving an opportunity to observe hemolysis when changing different parameters, such as tube diameter and length. Moreover, influence of different wall surfaces on hemolysis can also be examined easily. [93]

In the work of Bacher et al. [93], a capillary tube was used to examine the effect of wall shear stress, capillary material, hematocrit, and tube geometry (length and diameter) on hemolysis by shearing steer blood in laminar flow. Experimental results showed that cell surface interaction in the capillary tube was the main reason for mechanical hemolysis. Moreover, threshold level for shear stress was found to be 5000 dynes/cm^2 as a result of shearing blood for 10^{-2} seconds. [93] Keshaviah et al. [94] and Blackshear et al. [95] also studied hemolysis in capillary tubes with canine blood and observed the effect of entrance geometry on hemolysis in laminar flow. Blood was sheared for 10^{-2} seconds and the critical shear stress for hemolysis, which was dominated by entrance effects, was found to be 4500 dynes/cm^2 for normal capillaries and around 7000 dynes/cm^2 for capillaries with smooth, tapered entrance. [94, 95] The experiments of Keshaviah [94] were modeled in CFD study of Down et al., [96] where it was also

found that entrance effects in capillaries can be a significant factor contributing to hemolysis because of extensional stresses acting on cells. Yen et al. [97] recently aimed at the severe conclusion in a study combining simulation and experiments of capillary flow. Porcine blood was sheared for less than $6*10^{-5}$ s and results showed extensional stresses as main cause of hemolysis. The threshold stress value was found as 1000 Pa. In the present work, capillary tube experiments by Kameneva et al. [9] were simulated, in which bovine blood was sheared for shear stresses from 100 to 400 Pa and for cumulative exposure time of around 1 second. The effect of turbulent flow on hemolysis was examined and it was found that, hemolysis level was significantly larger in turbulent flow than in laminar flow for the same wall shear stress. Summary of the studies is also shown in Table 4.1.

Table 4.1. A review of capillary tube studies for hemolysis

References for Capillary tube experiments	**Exposure time (s)**	**Shear stress threshold for RBC damage (dynes/cm^2)**	**Flow field**
Bacher et al. [93]	100	5000	Laminar
Keshaviah et al. [94]	100	4500 - 7000	Laminar
Blackshear et al. [95]	100	4500 - 7000	Laminar
Yen et al. [97]	$6*10^{-5}$	10000	Laminar
Kameneva et al. [9]	0.025 - 1.25	425	Laminar and turbulent

4.2 Methods

4.2.1 Geometry and Computational Domain

The length and the diameter of the capillary tube of Kameneva et al. [9] were 70 mm and 1 mm, respectively, and the tube had conically shaped connectors (8 mm length) at each end of the capillary [Figure 4.1(B)].

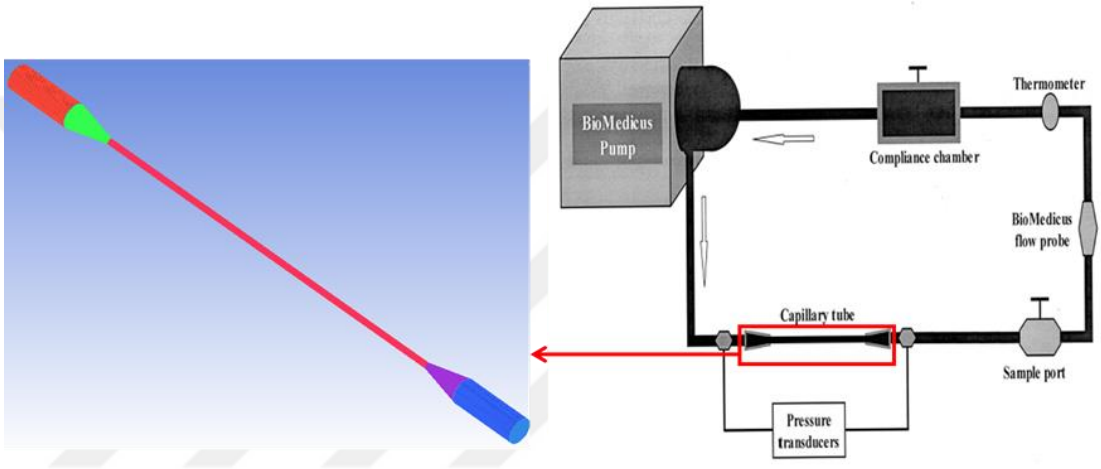

Figure 4.1. Left: 3D model of the capillary tube, Right: Flow loop used in experiments of Kameneva et al. [9]

Hemolysis experiments were performed by circulating washed bovine red cells in phosphate buffered saline (PBS) at a 24% hematocrit through the capillary in a closed loop network providing multiple short term exposures to turbulent flow. Capillary tube was in a closed circulating loop [Figure 4.1(B)] which includes a pump, PVC tubing, a water bath, a collapsible reservoir, and a small glass capillary tube. [9] The average time for circulation of blood in the experimental loop was calculated from total volume of blood sample and volumetric flow rates that were specified in the original work. [9] Moreover, average residence time of blood in the capillary tube was calculated from known volume of capillary tube and experimental volumetric flow rates. The number of

circulations of blood in the experimental loop was calculated from the given experimental time and the time for one circulation of blood in the flow loop. Finally, estimated cumulative exposure time of blood was calculated from given experimental time and times of blood for one circulation in the loop and in the capillary (Table 4.2). Estimated cumulative exposure time was on the order of 1 second. Times for one circulation of blood in the loop and in the capillary and the number of circulations were different for each experiment (100 – 400 Pa). However, cumulative exposure time of blood in each experiment (100 – 400 Pa) was found as equal, as was stated in the original work. [9] Results of the calculations that are mentioned above are summarized in Table 4.2.

Table 4.2. Exposure time calculations in capillary tube experiments

In Table 4.2, t(L) is the average circulation time of blood in the whole experimental loop, t(c) is the time for a single pass of blood in the whole capillary (including the conical shape connectors), t(n) is the residence time for a single pass of blood in the narrow part of capillary (excluding the conical shape connectors), N(L) is the number of passes through the capillary, texp(c) is the total exposure time for blood in the whole capillary (including the conical shape connectors), and texp(n) is the total exposure time for blood in the narrow part of capillary (excluding the conical shape connectors). All time units are in seconds.

Experimental wall shear stresses, Pa	**t(L)**	**t(c)**	**t(n)**	**N(L)**	**texp(c)**	**texp(n)**
100	104.8	0.23	0.023	52	12.04	1.19
200	65.5	0.15	0.014	82	12.04	1.19
300	46.2	0.103	0.0102	117	12.04	1.19
400	39.3	0.088	0.0086	137	12.04	1.19

4.2.2 Computational Mesh Development

The capillary tube [Figure 4.1(A)] was also meshed using Fluent 14.0 and its preprocessing program ICEM CFD (Ansys, Pittsburgh, PA). In the capillary tube geometry, a three dimensional model of the whole geometry with the conic entrance and exit regions was recreated. Meshing the entire geometries with hexahedral elements was performed after the geometries were created. Moreover, element orthogonality and the

mesh quality of the capillary tube was increased by using o-grids around the inlet and outlet region. After mesh creation in ICEM CFD, the flow geometries were imported into Fluent to solve the incompressible Navier-Stokes equations. Mesh independence of the models was tested on several parameters to check mesh integrity and independency by refining the grid in regions of high mean velocity gradient until the percent difference for pressure loss and velocity profile at multiple cross sectional cuts between a more and less refined simulation solution was less than 3%. The final mesh used for the capillary tube includes 1,773,099 cells and 2,023,864 nodes with an average grid cell size of $1x10^{-2}$ mm^3. Distribution of KLS and mean velocity magnitude results are shown in Figure 4.2. It can be seen from Figure 4.2 that velocity and KLS values in the capillary tube were independent of mesh size.

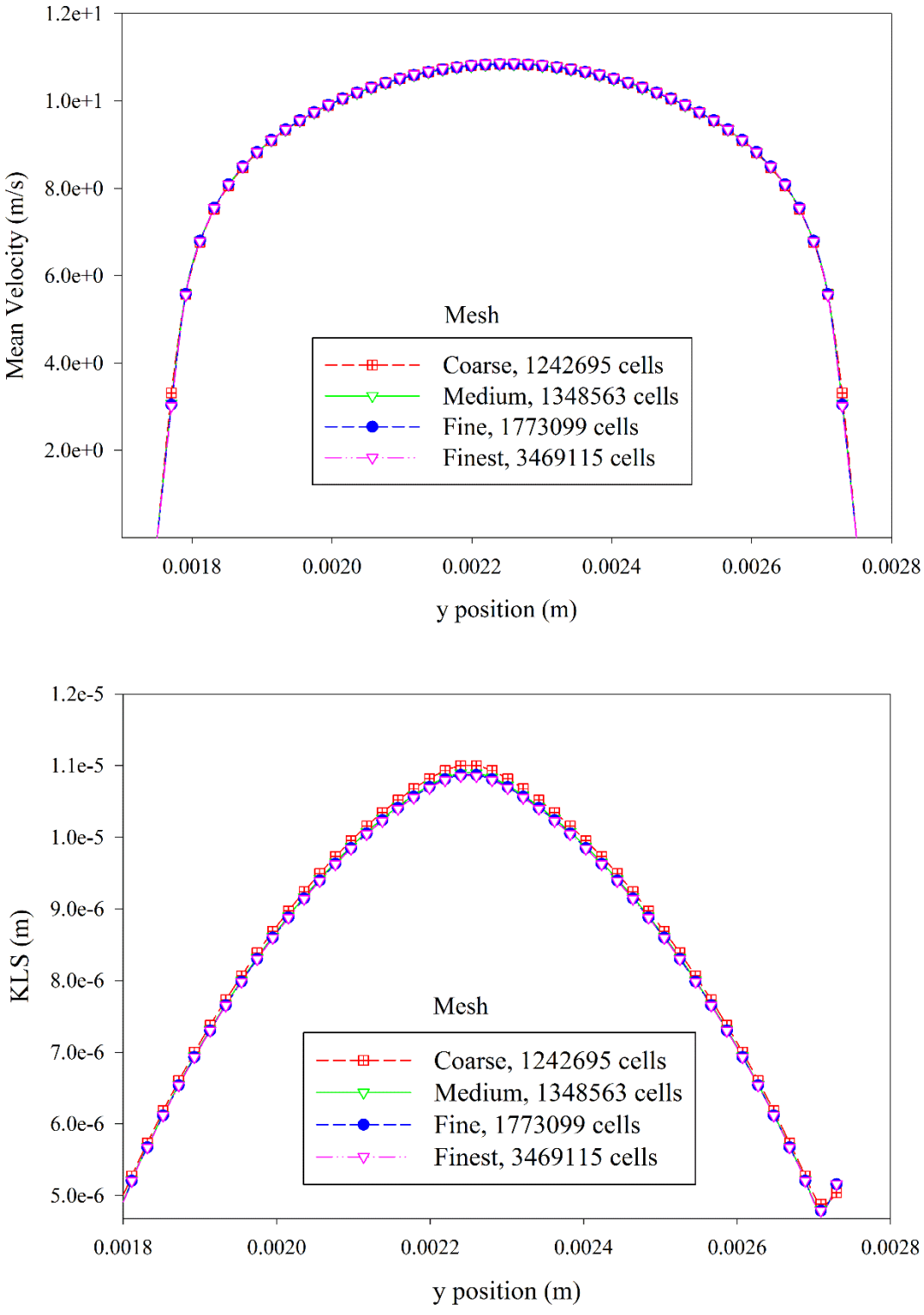

Figure 4.2. Top: Grid independence analysis for velocity. Bottom: Grid independence analysis for KLS. The k-ω SST model was used. Simulations were performed at velocity of 11.89 m/s and the wall shear stress of 400 Pa.

4.2.3 Flow Simulations

Capillary tube simulations were performed with velocity inlet boundary condition at the domain inlet. The no-slip boundary condition was applied on the capillary walls. The fluid properties for all simulations of the capillary tube [9] consisted of a Newtonian model with a viscosity of 0.002 Pa.s and a density of 1050 kg/m^3. Because the shear rates that were used in the capillary tube experimental study were much higher than 500 s^{-1}, Kameneva et al. [9] assumed that blood was a single phase homogeneous Newtonian fluid. Same as in the Couette viscometer experiments, the Newtonian and homogenous fluid assumptions are also valid in capillary tube experiments, since the suspensions used in the simulated experiments contained washed red blood cells in phosphate buffered saline (PBS).

Solution parameters were specified as the 2nd order upwind discretization scheme, the *presto* interpolation scheme for pressure, and the *simple* scheme for pressure-velocity coupling for capillary tube simulations that were performed with the finite volume based Fluent simulator. The flow simulations of the capillary tube experiments were started with a slow inlet velocity (such that the flow remained laminar). The velocity was slowly increased *in silico* until the resulting shear stress equaled one of the experimental wall shear stress values reported by Kameneva et al. [9] After the velocity attained a value high enough to yield turbulent flow, the k-ω SST model was applied. The procedure of increasing the velocity was repeated until all four cases of different shear stress values of 100 to 400 Pa of the Kameneva et al. [9] experiments had been simulated (see Table 4.3). Convergence criteria were chosen as 1x10^{-5} for the residuals of the velocity components,

the continuity equation, and the equations of k, ε, and ω of the turbulence models. The Reynolds numbers for the capillary experiments ranged from 2783 (for lowest shear stress, 100 Pa) to 6242 (for the highest shear stress, 400 Pa), as seen in Table 4.3. We assume that flow in the capillary tube is fully turbulent, since these Reynolds numbers are higher than the critical Reynolds number for pipe flow of 2100-2300. [53, 98]

Table 4.3. Model conditions for the capillary tube experiments

Wall Shear Stress (Pa)	**Inlet Velocity (m/s)**	**Experimental Hemolysis (%)**	**Reynolds Number**	**KLS Range (μm)**
100	5.3	0.0954	2783	1 – 52
200	8.1	0.1538	4253	1 – 39
300	10.12	0.7625	5313	5 – 33
400	11.89	1.9375	6242	4 – 29

The turbulence model (k-ε or k-ω SST) was selected by comparing the simulation results with Direct Numerical Simulation (DNS) data obtained from the literature in closely related flows. [99] The turbulence models for the capillary tube simulations were compared by using the DNS data of Chin et al., [99] who simulated turbulent pipe flow at 4 different friction Reynolds numbers (Re_τ = 180, 500, 1002, and 2003). They also compared the DNS data for boundary layer and channel, and found that statistical differences were negligible in these flows. Differences were found when comparing the transverse velocities and pressure fluctuations of channel and boundary layer. In this study, the simulation results and the DNS data were matched at corresponding friction

Reynolds number, Re_τ, which was defined as $Re_\tau = \frac{R}{l^*}$ where R is the radius of the pipe and $l^*$is the viscous length scale in wall turbulence, defined as $l^* = \frac{\upsilon}{u^*}$ (recall that $u^* = \sqrt{\frac{\bar{\tau}_w}{\rho}}$). Simulations were performed with both k-ε and k-ω SST models until obtaining the Re_τ value that was given in the DNS data Chin et al. [99] After simulations were completed, mean velocity profiles were calculated for the near wall regions using dimensionless wall parameters ($y^+ = \frac{Y}{l^*}$ and $u^+ = \frac{<U>}{u^*}$). The mean velocity profile for the capillary tube is plotted with the DNS data [99] in Figure 4.3. It can be seen from Figure 4.3 that using the k-ω SST in the computation of the flow domain can describe the near-wall region better than the k-ε model.

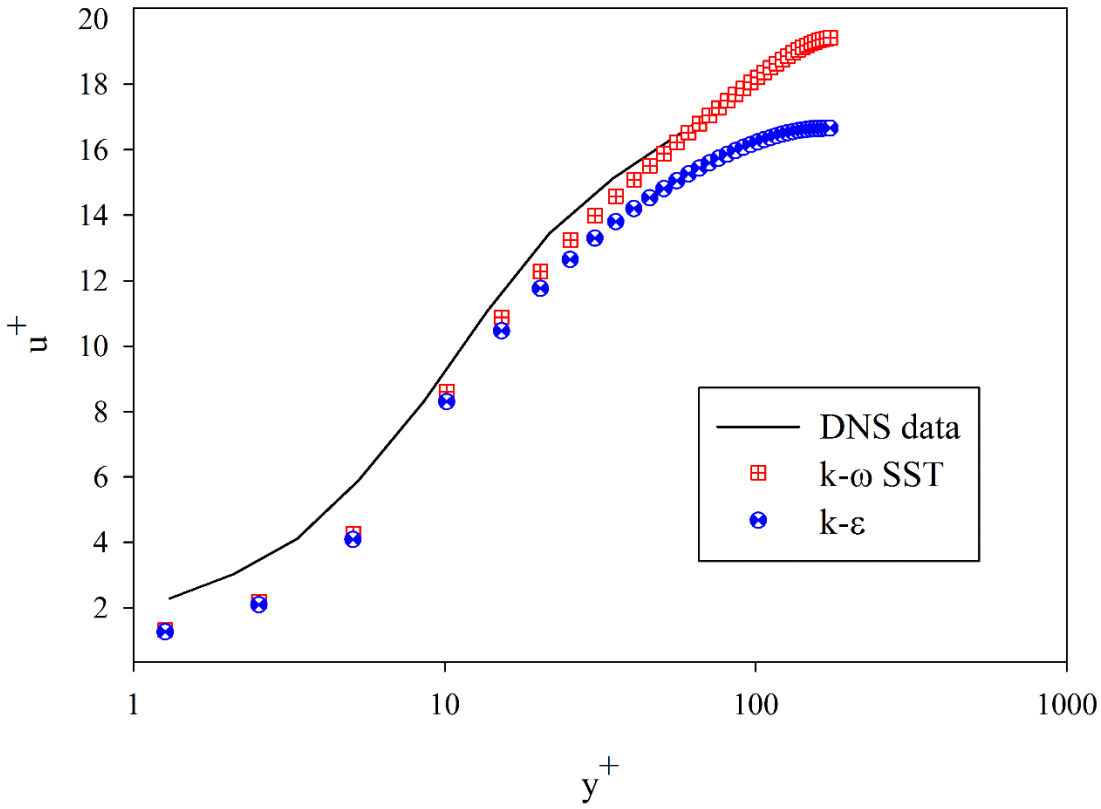

Figure 4.3. Capillary tube mean velocity profiles near wall using both k-ε and k-ω SST models for the DNS data of Chin et al. [99] at Re_τ =180 and τ_w= 499.8 Pa.

Root mean square errors for both models were determined and the k-ω SST model was chosen for the capillary tube simulations, (see Table 4.4).

Table 4.4. Root mean square errors for the turbulence models in the capillary tube

Root Mean Square Error	**Capillary Tube**
k-ε Model	1.32
k-ω SST Model	1.04

4.3 Results and Discussion

4.3.1 Relation between Eddy Size Distribution and KLS

KLS values were calculated between the conically shaped connectors [Figure 4.1(A)], since the experimental hemolysis data were derived from that region. [9] Planes perpendicular to the capillary axis were created, the KLS values were calculated on each plane, and then analyzed (Figure 4.4).

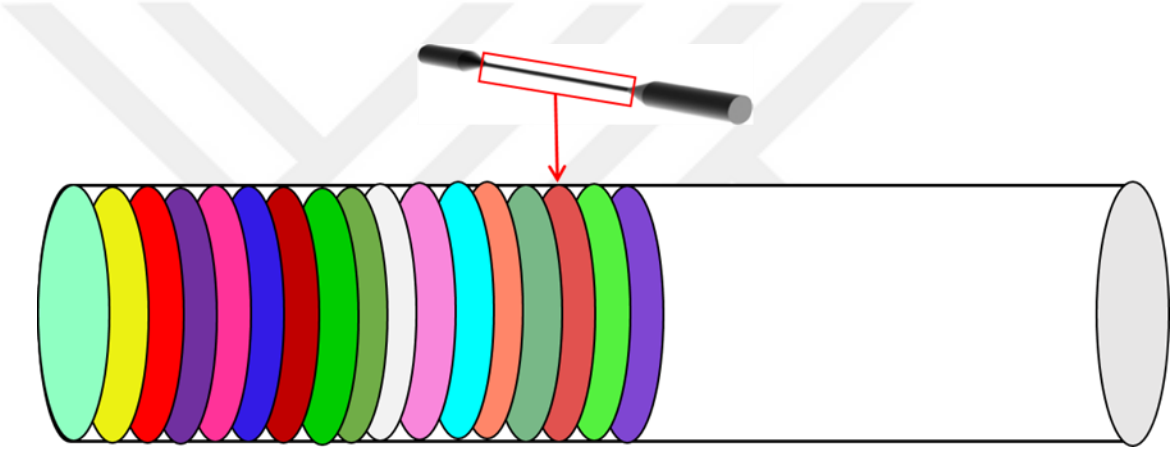

Figure 4.4. Planes in capillary tube.

On each created plane, the KLS values exhibited a range as can be seen on Table 4.5. The first column of each experiment (100 to 400 Pa) indicates the location of the planes, while the second column show the smallest and the largest KLS values. For the planes that have different range of KLS values, they were analyzed separately. When the KLS ranges were the same for the planes, they were analyzed together. Calculations were performed for every plane and every KLS value of each plane for 4 experiments of the capillary tube seen in Table 4.3.

Table 4.5. KLS ranges in all of the planes in the capillary tube for all experiments (100-400 Pa). The plane location of 20.4 mm is at the pipe entry.

100 Pa

Plane locations, mm	KLS: min-max, µm
20.4	1 - 51
21.5	1 - 52
22	1 - 51
23	23 - 47
24	16 - 43
25	12 - 40
26	11 - 38
27	10 - 38
28 - 29	10 - 39
30	9 - 35
31	9 - 27
32	9 - 23
33	9 - 20
34	9 - 19
35 - 90	9 - 18
90.4	10 - 18

200 Pa

Plane locations , mm	KLS: min-max, µm
20.4	1 – 39
21.5	18 – 39
22	14 – 37
23	9 – 32
24	7 – 27
25	7 – 24
26 - 27	7 – 25
28	7 – 26
29	7 – 24
30	6 – 21
31	6 – 18
32	6 – 16
33 - 34	6 – 15
35 - 90	6 – 14
90.4	7 – 14

300 Pa

Planes locations, mm	KLS: min-max, µm
20.4	7 – 33
21.5	9 – 32
22	7 – 29
23	6 – 23
24 - 26	5 – 19
27 - 28	5 – 20
29	5 – 18
30	5 – 16
31	5 – 15
32	5 – 14
33	5 – 13
34 - 90	5 – 12
90.4	5 – 12

400 Pa

Planes locations, mm	KLS: min-max, µm
20.4	5 – 29
21.5	6 – 27
22	5 – 24
23	5 – 18
24	4 – 15
25 - 26	4 – 16
27	4 – 17
28	4 – 16
29	4 – 15
30	4 – 14
31	4 – 13
32	4 – 12
33 - 36	4 – 11
37 - 90	4 – 10
90.4	5 – 10

The range of KLS values observed in the capillary tube was between 4 µm and 29 µm for the highest wall shear stress, while the maximum value of KLS was up to 52 µm for lower shear stress simulations. The complete range of experimental conditions is shown in Table 4.3.

The time-averaged spatial distribution of KLS values in a vertical plane in the middle of the capillary is shown for the highest wall shear stress experiment in Figure 4.5. As can be seen from this figure, KLS values reached a maximum in the middle of the capillary tube with minimum values near the wall.

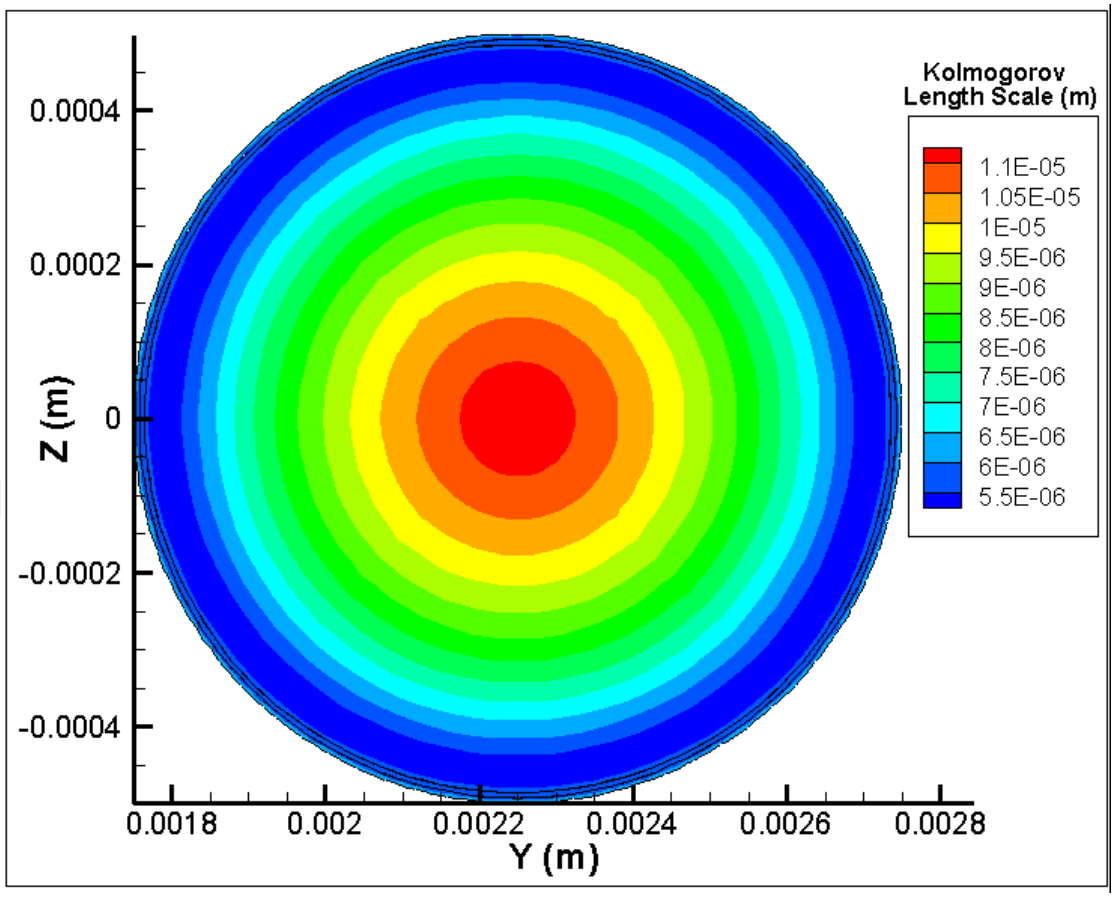

Figure 4.5. KLS values of the plane in the middle of the capillary tube for the highest wall shear stress experiment (400 Pa, shown in Table 4.3) using the k-ω SST model.

A characteristic eddy size distribution was calculated by evaluating the eddy sizes based on the Kolmogorov length scale. As discussed before, calculations were performed for 4 experiments of the capillary tube as seen in Table 4.3. Results showed a similar shift with the Couette viscometer distribution (Figure 3.5), by having smaller values with simulations for increasing shear stress (Figure 4.6). This shift reflects greater energy dissipation with higher flow rates in the capillary tube. Moreover, similar with the Couette viscometer experiments, the number of smaller eddies increases at greater hemolysis in the capillary tube, suggesting that KLS analysis can help to predict blood damage in turbulent flow.

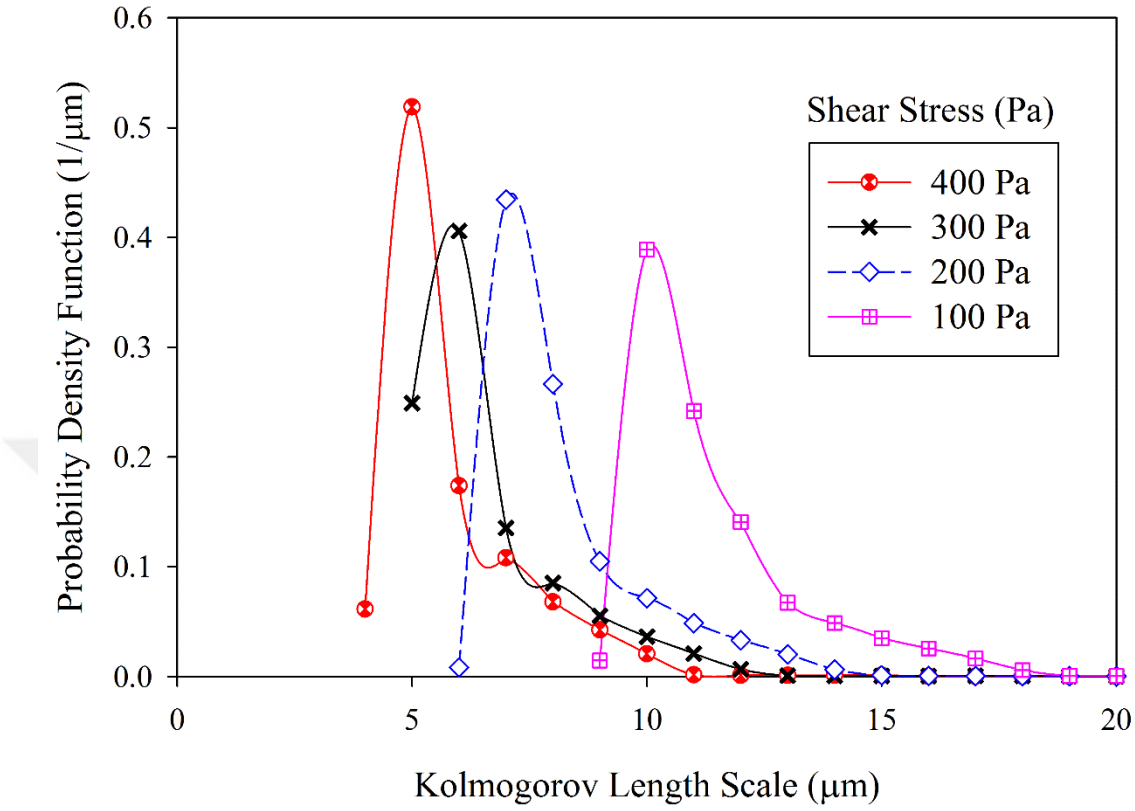

Figure 4.6. Probability distribution of KLS values in the capillary tube for all experiments (400 Pa – 100 Pa). The area under the each curve is equal to 1.

When KLS distributions in the capillary tube (Figure 4.6) are compared with the Couette viscometer KLS distribution (Figure 3.5), it can be seen that, for a specific wall shear stress, the capillary tube has higher KLS values. For example, if we pick 100 Pa for the wall shear stress and 20% for the frequency of the eddy distribution in Figure 4.6 and Figure 3.5, the range of KLS values for the capillary is between 10-12 μm and the range of KLS value for the Couette viscometer is between 4-6 μm. It can be concluded that Couette viscometer gives lower KLS values for the same wall shear stress values. The total stress in turbulent Couette flow is practically constant across the gap width, but it changes in the capillary from the wall to the center of the channel, leading to different

Reynolds stress profiles in the two flow configurations and, thus, to different turbulent kinetic energy dissipation patterns. Nevertheless, the figure also illustrates the difficulty in comparing turbulent flows in different devices, even when the wall shear stress is the same.

4.3.2 The Effect of Eddy Surface Area on Hemolysis

The total surface area of the KLS-sized eddies per volume has been calculated for the four experiments in the capillary tube as a function of the KLS values. Analysis to find a relation between eddy area and hemolysis continued by combining experimental results of each experiment of the capillary tube. A relationship between eddy surface area per volume and hemolysis is shown in Figure 4.7. Please note that in the figures of the rest of this section, each data point corresponds to observed hemolysis reported in the experiments of Kameneva et al. [9], while the eddy area (or eddy number, or eddy volume) for the specified KLS size is found from simulation of that experiment. The lines are plotted to guide the eye over the data points. In the capillary tube experiment, % hemolysis was not given directly in the original work [9]. We calculated hemolysis using the formula [22] $H(\%) = \frac{\Delta Hb}{Hb} * 100$ where, H is the percentage of hemolysis, ΔHb is change of plasma hemoglobin as hemoglobin is released, and Hb is the total amount of hemoglobin (hemolysis values can be seen on Table 4.3).

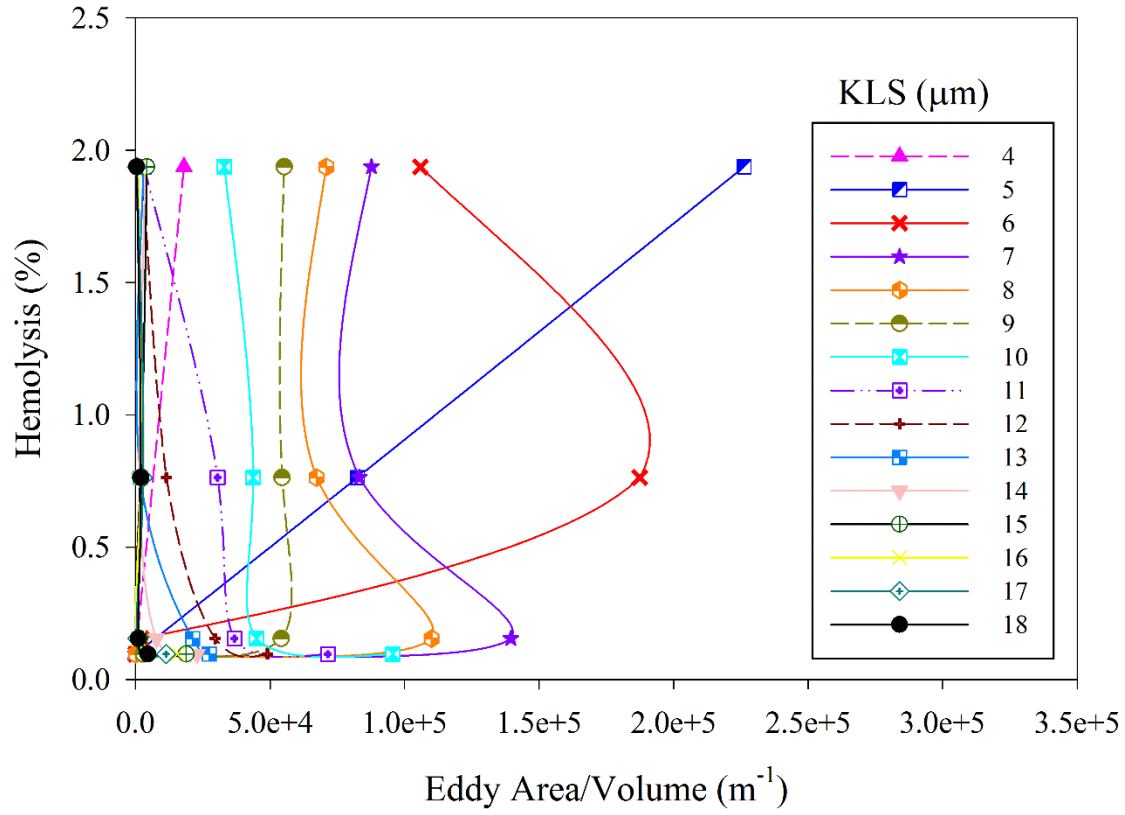

Figure 4.7. Hemolysis as a function of normalized eddy surface area in the capillary tube (experimental data from Kameneva et al. [9]).

It can be seen from Figure 4.7 that, the data corresponding to KLS values above 5 µm indicate lines that curve back, showing no obvious relationship with hemolysis.

Eddies below a certain size seem to cause hemolysis as can be seen from Figure 4.7 that the critical eddy size is 5µm for the capillary flow, respectively. Similarly with the Couette viscometer, we also examined the cumulative effect of all eddies with a size less than a critical value in the capillary tube experiments. The KLS eddy surface area was summed up as the KLS values increased. The cumulative sum of eddy surface area values versus % hemolysis is shown in Figure 4.8.

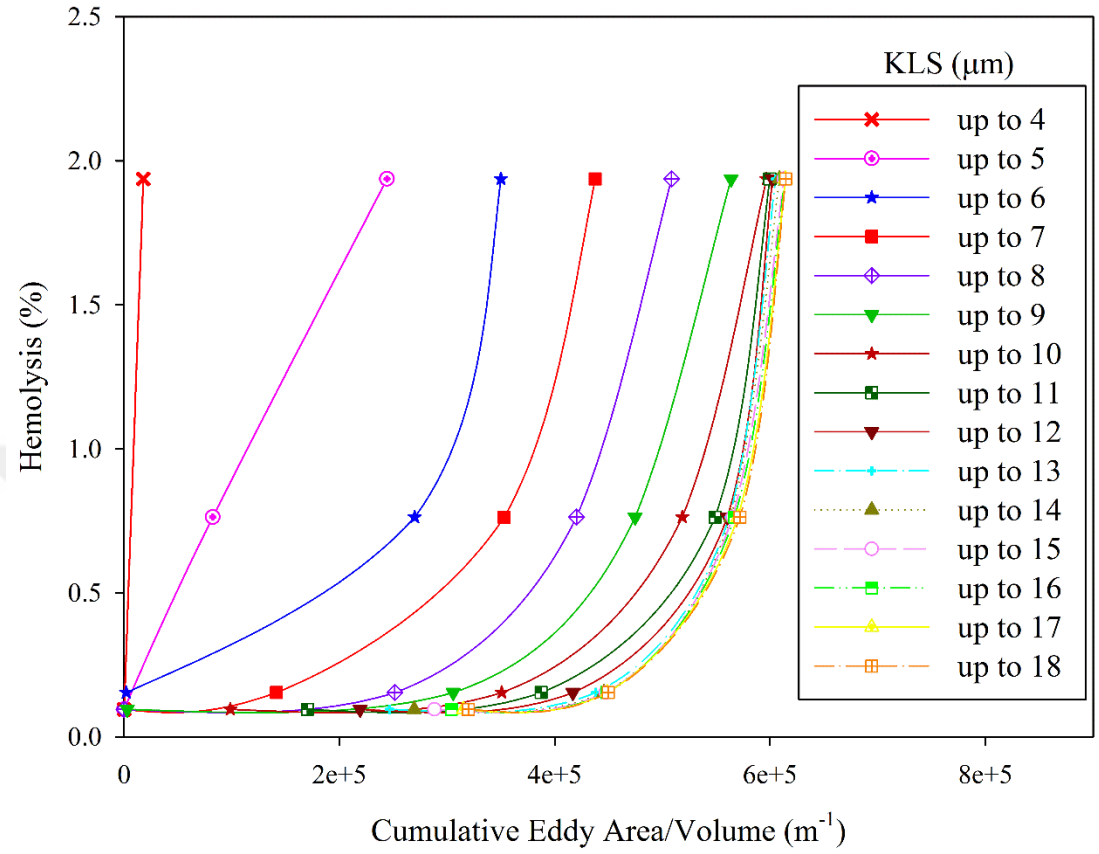

Figure 4.8. Hemolysis as a function of cumulative eddy surface area in the capillary tube.

Figure 4.8 shows that hemolysis increases with increasing KLS eddy area per unit volume. Also, similar to the cumulative eddy area of the Couette viscometer (Figure 3.7), the curves for larger KLS values start to overlap with each other. For example, overlapping can be seen clearly in the capillary tube for KLS ≥ 10 μm.

4.3.3 The Effect of Eddy Number on Hemolysis

The total number of the KLS-sized eddies per unit volume has been calculated for the four experiments in the capillary tube as a function of the KLS values. Eddy number values were calculated and combined for each experiment of the capillary tube and plotted

with the experimental hemolysis (Table 4.3). A relationship between eddy number per volume and hemolysis is shown in Figure 4.9.

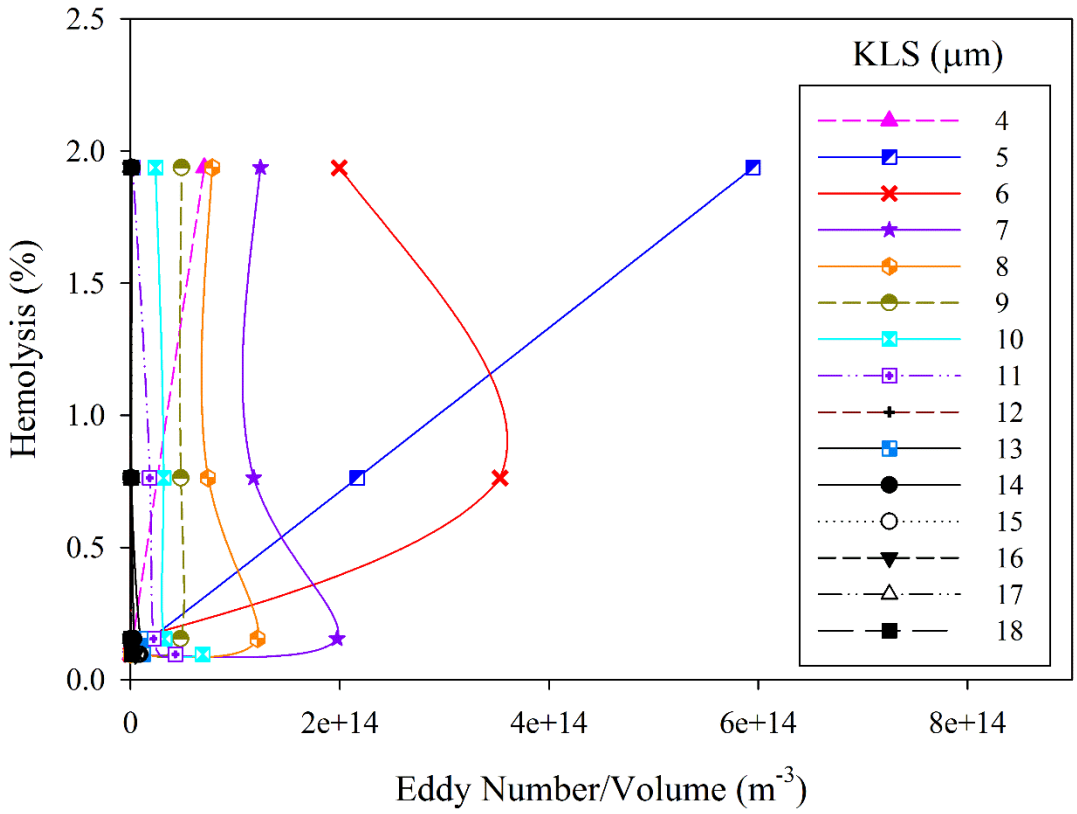

Figure 4.9. Hemolysis as a function of eddy number in the capillary tube.

Figure 4.9 also shows similar behavior as Figure 4.7 about eddy area, with having vertical lines for KLS values larger than 5 μm and indicating no obvious relationship with hemolysis.

Additionally, critical KLS size for hemolysis was also examined by looking at the cumulative effect of all eddies. Eddy number values were summed up to a specific KLS size and plotted with experimental hemolysis (Figure 4.10). Cumulative eddy number also indicated a similar relationship with cumulative eddy area in the capillary tube. When hemolysis increases, the cumulative eddy number was also increased. Also, for larger

KLS values (KLS ≥ 10 μm) again curves were overlapping by suggesting no difference on hemolysis with the smaller KLS values.

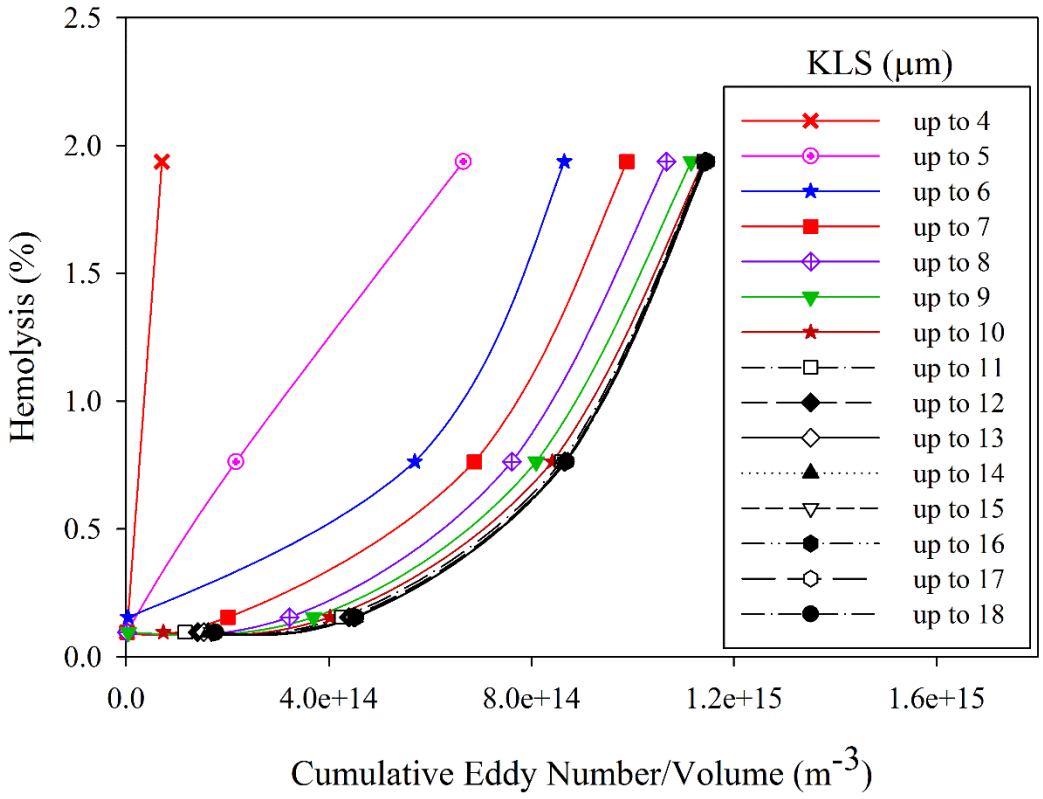

Figure 4.10. Hemolysis as a function of cumulative eddy number in the capillary tube.

4.3.4 The Effect of Eddy Volume on Hemolysis

Total eddy volume of the KLS-sized eddies per unit volume was the last parameter investigated on eddy analysis. Similar analysis with eddy area and eddy number was performed for the eddy volume and hemolysis relationship. Eddy volumes were calculated for each experiment for every KLS size then plotted with experimental hemolysis. The eddy volume per volume and hemolysis relationship is shown in Figure 4.11.

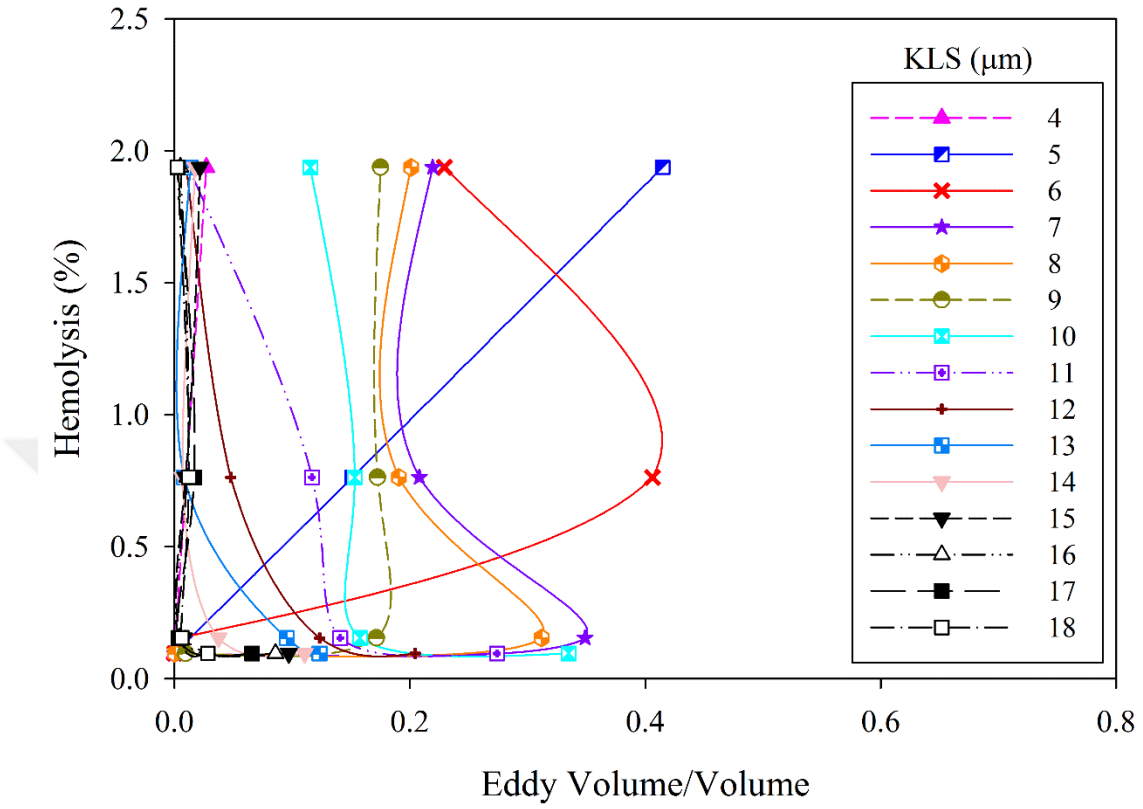

Figure 4.11. Hemolysis as a function of eddy volume in the capillary tube.

Eddy volume also shows similar relation as eddy area and eddy number in the capillary tube. Curves become vertical for KLS values bigger than 5 µm (Figure 4.11).

To investigate the eddy volume relation further and deeper, the cumulative volumes were also calculated for different KLS sizes and plotted with hemolysis. The cumulative sum of eddy volume values versus % hemolysis is shown in Figure 4.12.

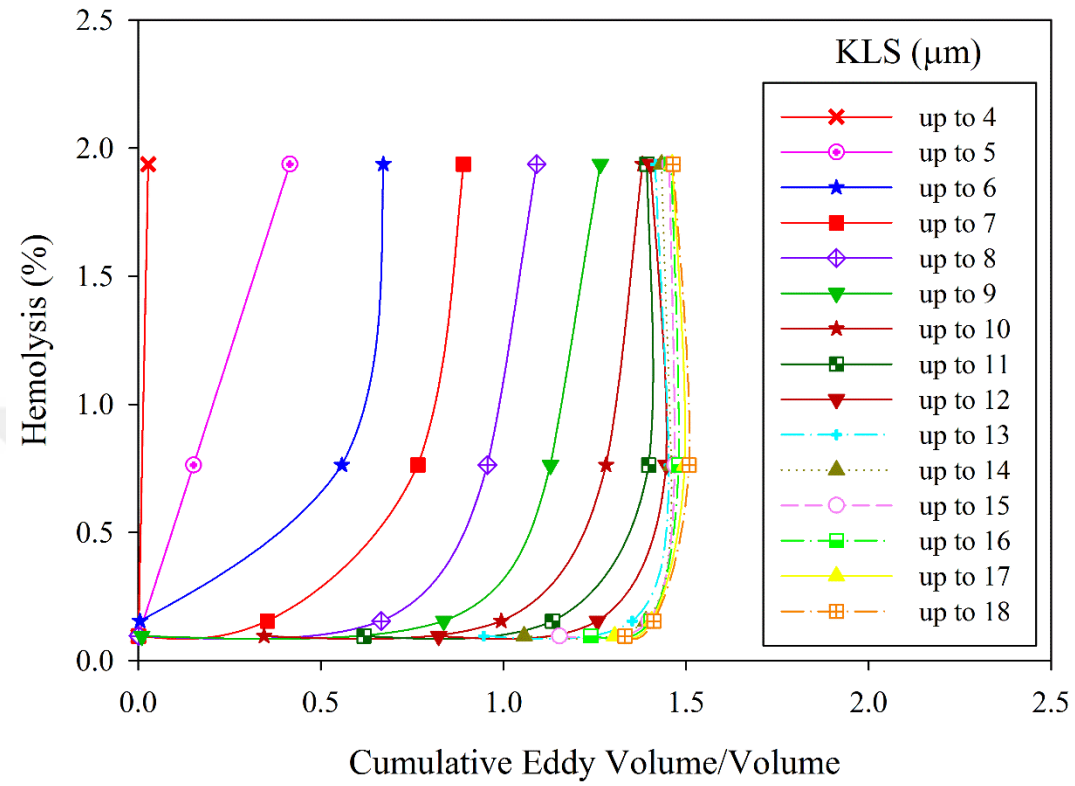

Figure 4.12. Hemolysis as a function of cumulative eddy volume in the capillary tube.

As can be seen from Figure 4.12 that hemolysis increases with increasing KLS eddy volume per unit volume. Moreover, curves for larger KLS values are overlapping as well as tending to become vertical suggesting no effect on hemolysis for larger KLS values.

4.3.5 Reynolds Stress Calculations and Threshold Analysis

Calculations were performed for 4 experiments of the capillary tube [9] (Table 4.3). Although, capillary tube experiments have lower degrees of hemolysis than these for Couette viscometer, they still have varying levels of hemolysis for each experiment. Hemolysis levels varied from 0.1% to 1.9% enabling threshold analysis in the same way

as in the Couette viscometer. Results show that for the highest shear stress experiment (400 Pa), the threshold Reynolds stress value is 272 Pa (shown with red color in Figure 4.13), representing that 1.9% (hemolysis level of 400 Pa experiment) of spatial distribution of Reynolds stress was above this value.

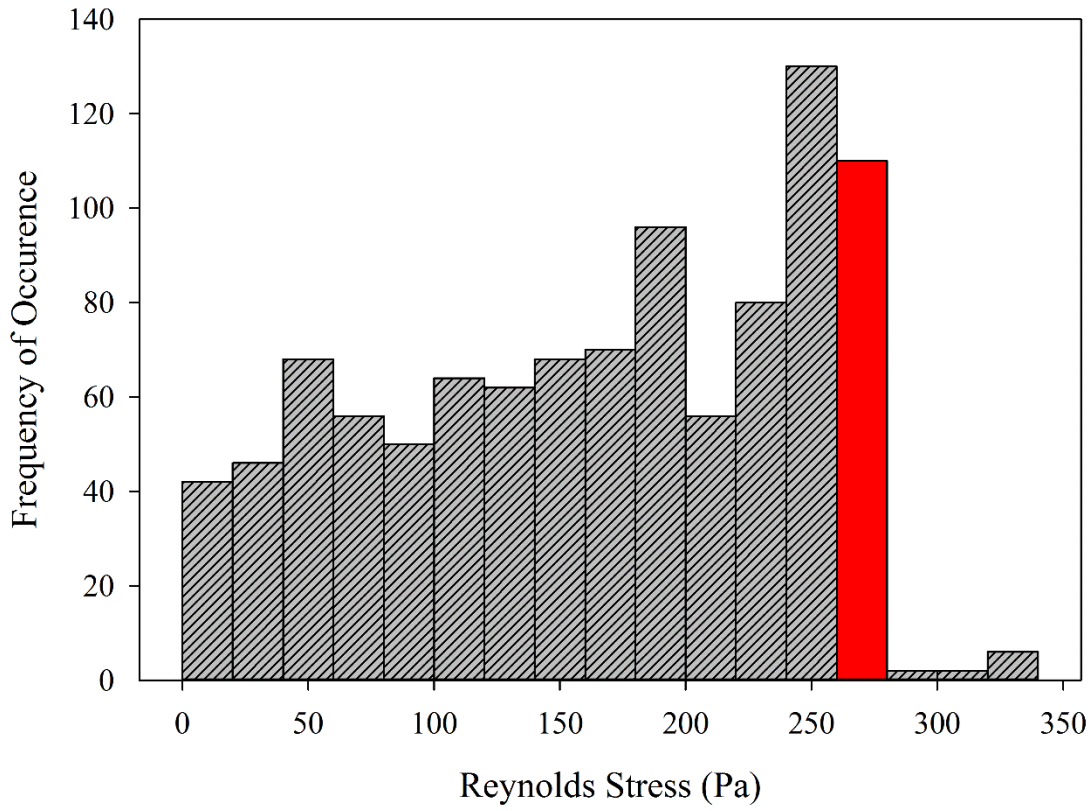

Figure 4.13. Distribution of Reynolds stresses in capillary tube for the highest wall shear stress (400 Pa) experiment. There were a total of 1071 mesh points examined on 21 different rakes in the capillary tube.

In the next highest shear stress experiment (300 Pa), it was seen that the threshold Reynolds stress value decreased to 229 Pa. Similar analyses were repeated for the lower shear rate experiments (200 Pa and 100 Pa) and the frequency plots are shown in Figure 4.14.

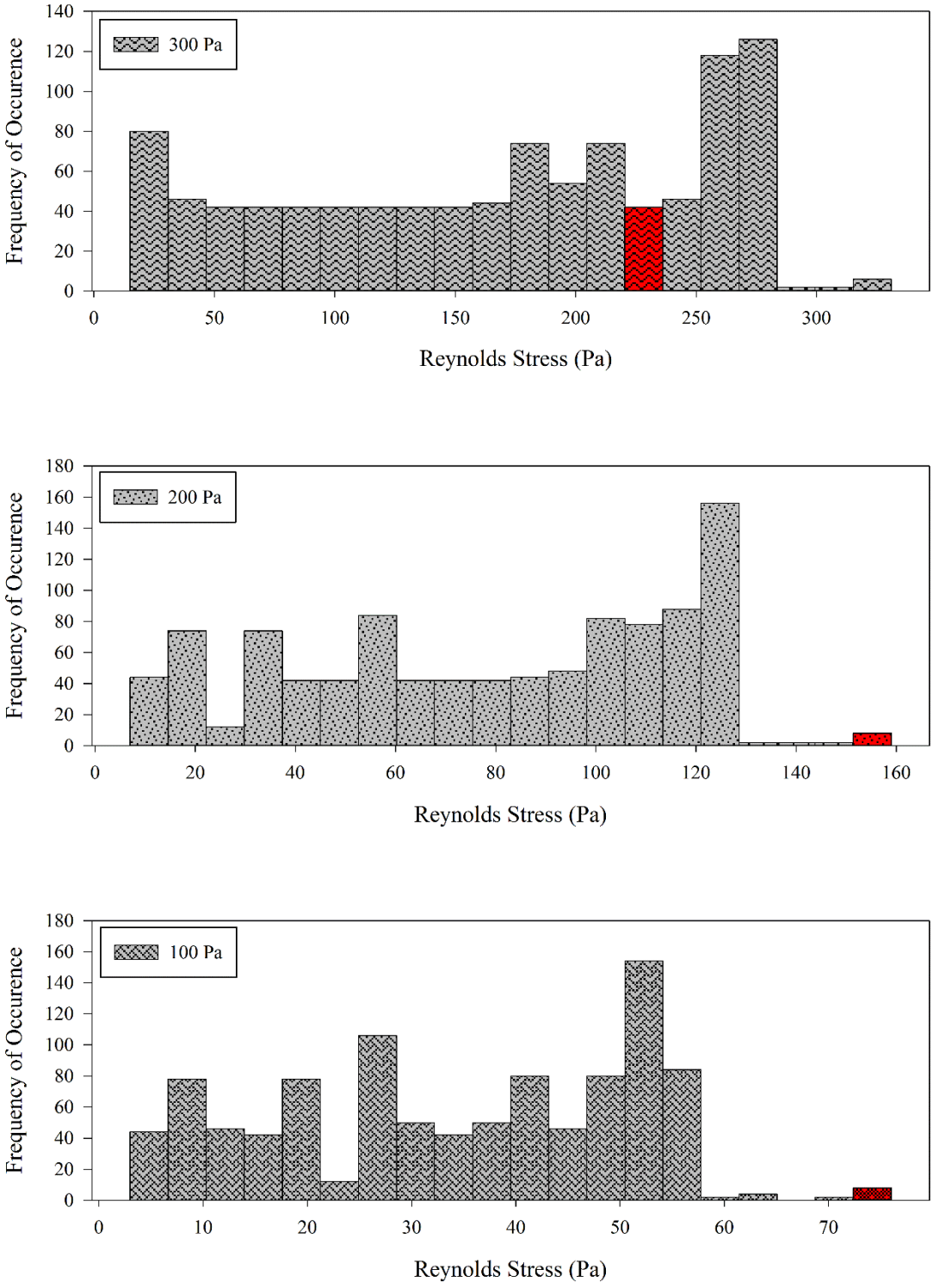

Figure 4.14. Distribution of Reynolds stresses in the capillary tube for all experiments (400 Pa - 100 Pa). There were a total of 1071 mesh points examined on 21 different rakes in the capillary tube.

The threshold Reynolds stress values for each experiment showed that there were 4 different Reynolds stress threshold values for four different experiments (Figure 4.15). As in Couette viscometer experiments, it was expected to see a common threshold. Results do not support Reynolds stress as a determining factor for hemolysis.

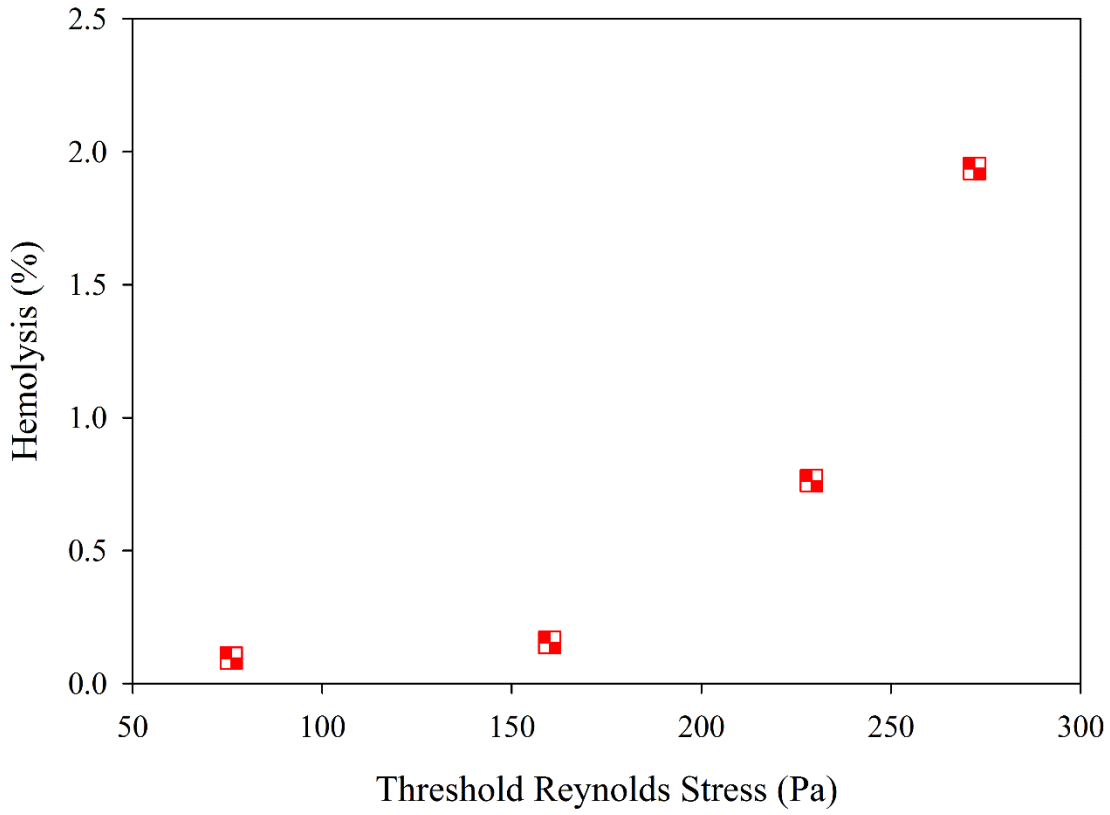

Figure 4.15. Estimated values of critical Reynolds stresses in capillary tube for all the experiments (400 Pa – 100 Pa).

4.3.6 Viscous Stress Calculations and Threshold Analysis

A similar procedure was applied to viscous stresses for the capillary tube. Viscous stress distributions were calculated for each experiment of the capillary tube and threshold viscous stresses determined. A histogram for the highest shear stress experiment is shown in Figure 4.16.

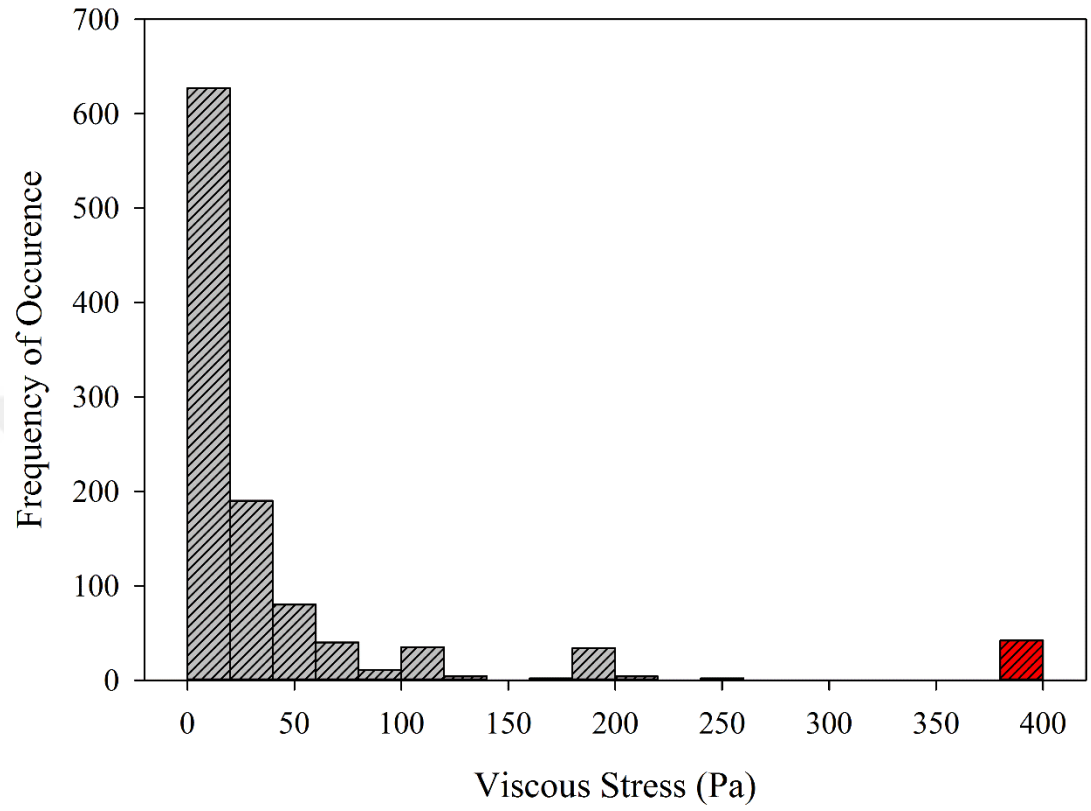

Figure 4.16. Distribution of viscous stress in the capillary tube for 400 Pa. There were a total of 1071 mesh points examined on 21 different rakes in the capillary tube.

The same analysis was repeated for the entire series of lower shear rate experiments (300 Pa -100 Pa) and the frequency plots are shown in Figure 4.17. For every experiment of the capillary tube, a different threshold viscous stress value was found. All threshold stress values are also plotted in Figure 4.18. Threshold viscous stress increased with increasing shear stress with no common viscous stress value found for the capillary tube.

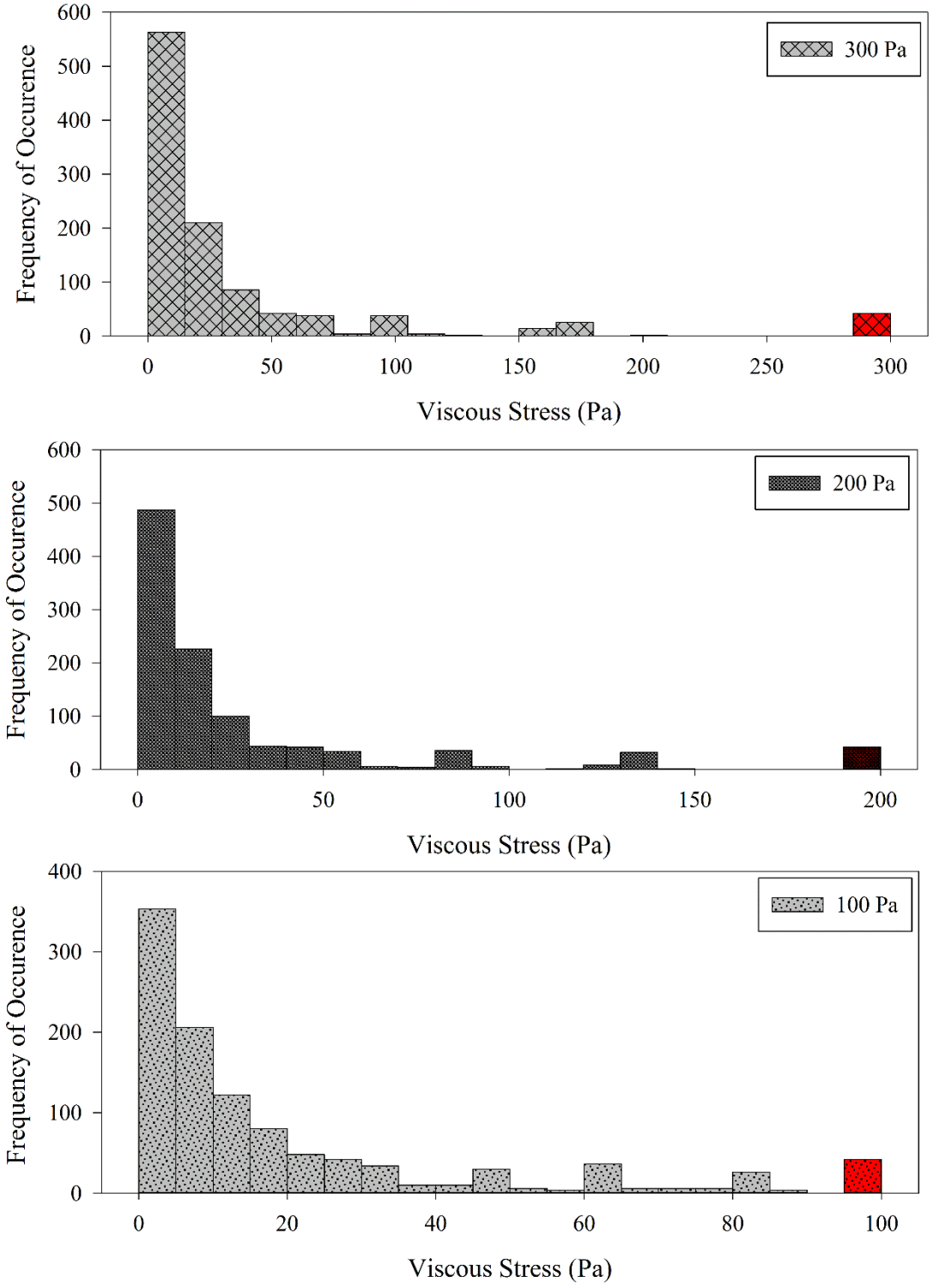

Figure 4.17. Distribution of viscous stresses in the capillary tube for all experiments (400 Pa - 100 Pa). There were a total of 1071 mesh points examined on 21 different rakes in the capillary tube.

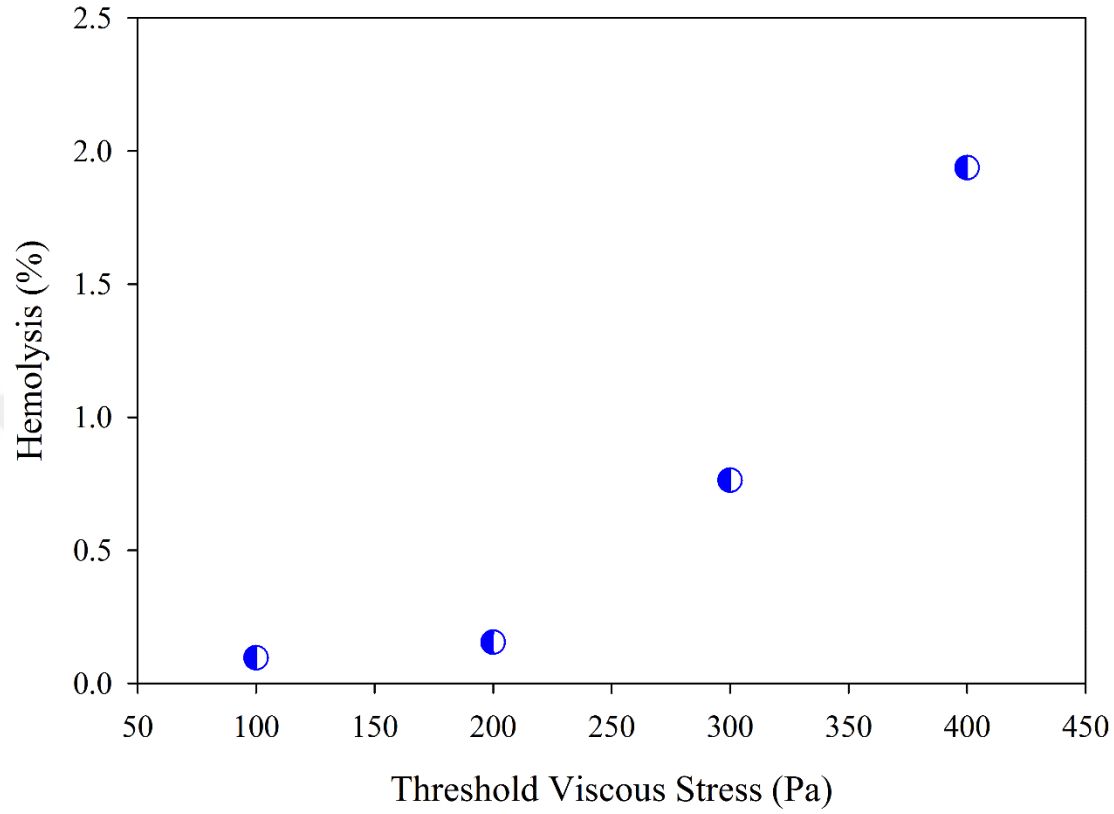

Figure 4.18. Distribution of viscous stresses in capillary tube for all experiments.

It can be concluded as a result of Reynolds stress and viscous stress threshold analysis for the experiments of capillary tube that Reynolds and viscous stresses are not determining parameters for hemolysis.

4.4 Summary

The results of the capillary tube experiments were supporting the results of the Couette viscometer experiments. Threshold analysis results showed that Reynolds stress and viscous stress are not determining parameters for hemolysis prediction, while KLS gives promising and also consistent results with the Couette viscometer. Results of Couette and capillary experiments showed that hemolysis is related directly with the total surface area of eddies with diameters of up to about 10 μm. This indicates that our method (*eddy analysis*) has applicability to work with distinctly different flow conditions (Couette and capillary) and, more importantly, with exposure times varied by orders of magnitude. We applied this method to another experimental setting (jet) to confirm these results and also to propose a hemolysis model in chapter 7.

5 Hemolysis Calculations Using Power Law Models

5.1 Introduction

After examining the existence of threshold Reynolds and viscous stresses for both Couette viscometer and capillary tube in chapters 3 and 4 respectively, it was seen that Reynolds stress and viscous stress do not exhibit a threshold value for hemolysis. In order to explore this question further, we have used four commonly accepted power law models (Giersiepen et al. [21], Heuser et al. [22], Zhang et al. [69], and Fraser et al. [23]), which are of the form of Equation 1.1, to investigate the effects of area averaged, time averaged Reynolds, viscous, total, and wall shear stresses on hemolysis. Calculations were performed only for capillary tube experiments, because power law models are not expected to apply for the Couette viscometer experiments since they were conducted for the very long RBC exposure time of 4 min. Coefficients and the forms of the power law equations are shown in Table 5.1.

Table 5.1. Power law models for hemolysis

Giersiepen et al. [21]	$HI(\%) = 3.62 * 10^{-5}\tau^{2.416}t^{0.785}$
Heuser et al. [22]	$HI(\%) = 1.8 * 10^{-6}\tau^{1.991}t^{0.765}$
Zhang et al. [69]	$HI(\%) = 1.228 * 10^{-5}\tau^{1.9918}t^{0.6606}$
Fraser et al. [23]	$HI(\%) = 1.745 * 10^{-6}\tau^{1.963}t^{0.7762}$

5.2 Methods and Calculations

Calculations of stresses were already discussed in chapter 2. Area averaged, time averaged Reynolds, total, and viscous stresses were calculated for four experiments of the capillary tube that can also be seen on Table 5.2.

Table 5.2. Different types of calculated stresses in the capillary tube

Experimental Shear Stress (Pa)	Reynolds stress (Pa)	Total stress (Pa)	Viscous stress (Pa)
100	36.8	68.6	31.8
200	89.2	137.3	48.1
300	146.4	206.0	59.6
400	204.2	274.6	70.3

After stresses were calculated, hemolysis calculations were performed by using the different power law models that are shown in Table 5.3. Regression analysis was performed to calculate the hemolysis index, HI, for different type of power law models by inserting the average Reynolds (τ_{Re}), total (τ_t), viscous (τ_v), and wall shear stresses (τ_w) instead of stress (τ) in the power law models. Moreover, for the exposure time (t) in different power law models, the time that blood makes a single pass through the narrow part of capillary was used. That time was calculated in Table 4.2 at column 4 which was shown as t(n) in Table 4.2. Since, the blood had multiple exposures by circulating several times in the experimental system of Kameneva et al. [9] the calculated hemolysis values were multiplied with the number of circulations of blood in the whole experimental loop, which was calculated and shown at the 5^{th} column of Table 4.2 as N(L). Finally,

hemolysis predictions were compared with experimental hemolysis data of Kameneva et al. [9] by calculating standard errors. All hemolysis calculations and the standard error are shown in Table 5.3. Standard error (SE) calculation was performed using the formula[100] $SE = \frac{sdev}{\sqrt{N}}$ where *sdev* is the standard deviation and N is the number of observations that correspond to the four different experiments of Kameneva et al. [9]

5.3 **Results and Discussion**

Results of regression analysis for calculated hemolysis index (HI) for four different power law models and standard error when calculations are compared to experimental measurements by Kameneva et al. [9] are shown in Table 5.3.

Table 5.3. Hemolysis calculations for four different power law models by using k-ω SST model.

Power Law Models	Type of Stress	Calculated HI for τ_w=100 Pa	Calculated HI for τ_w=200 Pa	Calculated HI for τ_w=300 Pa	Calculated HI for τ_w=400 Pa	Standard Error [100]
Experimental Hemolysis Data [9]	τ_w	0.0954	0.1538	0.7625	1.9375	0
Giersiepen et al. [21]	τ_{Re}	0.4106	3.9302	13.8268	32.0492	6.6658
	τ_t	2.0132	11.8869	34.1216	70.8037	14.8321
	τ_v	0.3455	1.0587	2.0452	3.2602	0.2485
	τ_w	6.5674	38.7766	111.3085	230.9699	49.3428
Heuser et al. [22]	τ_{Re}	0.0051	0.0335	0.0963	0.1944	0.3861
	τ_t	0.0188	0.0833	0.2028	0.3735	0.3513
	τ_v	0.0044	0.0114	0.0199	0.0296	0.4224
	τ_w	0.0497	0.2208	0.5372	0.9897	0.2126
Zhang et al. [24]	τ_{Re}	0.0514	0.3568	1.065	2.1868	0.0557
	τ_t	0.1905	0.8886	2.2428	4.2034	0.469
	τ_v	0.0445	0.121	0.2203	0.3323	0.3686
	τ_w	0.5049	2.3553	5.9447	11.1413	1.9226
Fraser et al. [23]	τ_{Re}	0.0043	0.0274	0.0775	0.1546	0.3947
	τ_t	0.0155	0.0673	0.1614	0.2943	0.3677
	τ_v	0.0037	0.0094	0.0164	0.0241	0.4234
	τ_w	0.0406	0.176	0.4217	0.7692	0.267

As can be seen from hemolysis predictions on Table 5.3 that the power law model of Zhang [24] gives the lowest standard error. The highest error was obtained by using

Giersiepen's [21] power law model. When results were compared examining different stresses (Reynolds, viscous, total, and wall shear stresses), the best agreement between the experimental data and the power law models was obtained by using Reynolds stress. The worst agreement was obtained by using wall shear stress with Giersiepen's [21] power law model. The greater error is expected because 300 and 400 Pa are outside the range of the experimental conditions used to obtain Giersiepen's model (stresses were less than 255 Pa and exposure times were less than 700 ms). Even though the 400 Pa experiment was higher than the experimental shear stress of Zhang's model (exposure times of less than 1500 ms and shear stresses between 50-320 Pa), it still gave the smallest error with Reynolds stress. Fraser's model is applicable for much lower shear stresses than the experimental conditions of Kameneva, but it still gave smaller errors comparable to Zhang and Heuser. These calculations illustrate the challenge in applying the power law models developed from homogeneous laminar flow measurement to the analysis of devices with complex turbulent flows. The above findings were also plotted for the best (Zhang's) and the worst (Giersiepen's) power law models using all different stresses in Figure 5.1.

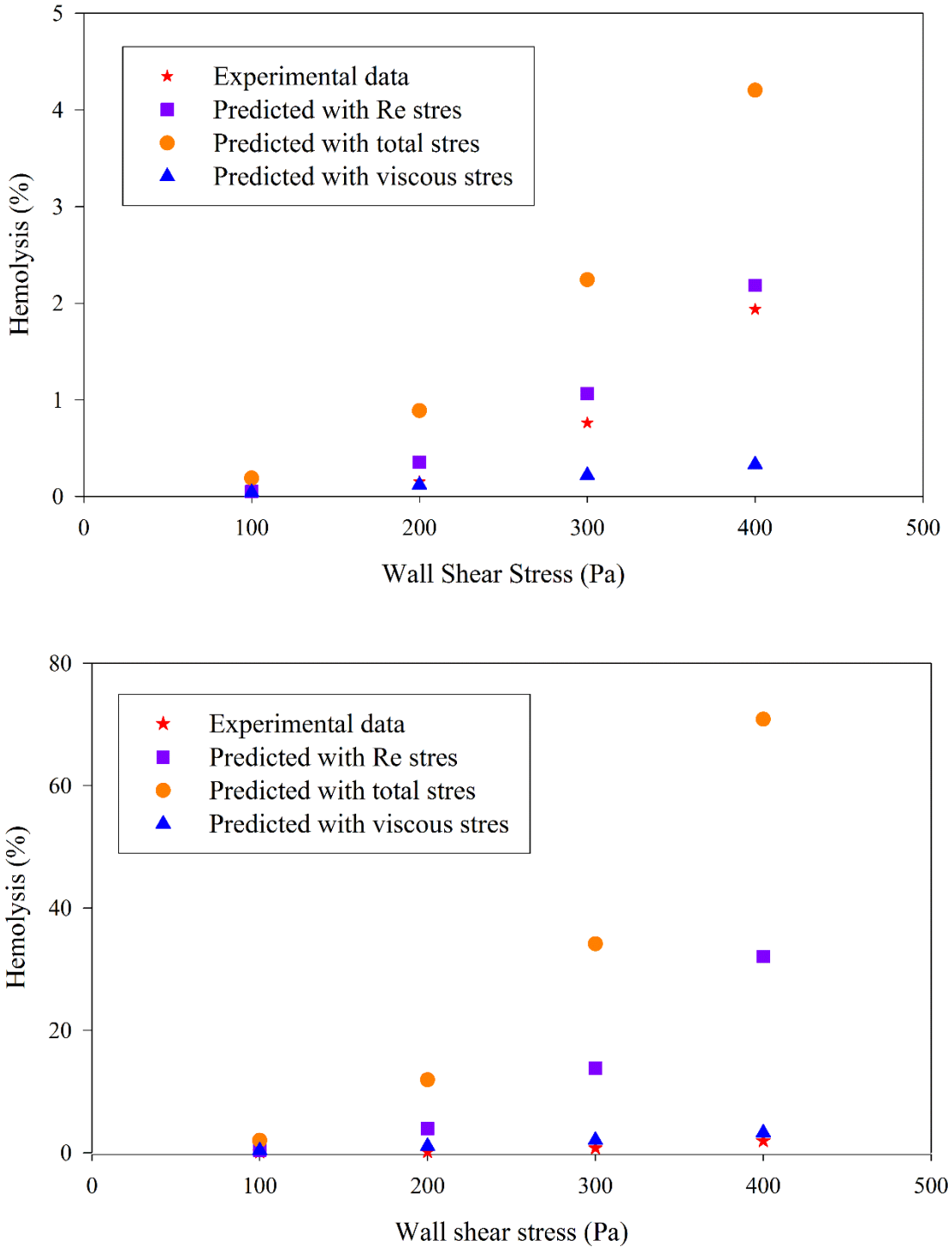

Figure 5.1. Hemolysis predictions using different stresses. Top panel: H% with Zhang's model [24] and bottom panel: H% with Giersiepen's model. [21]

The same analyses as discussed above was also performed for k-ε turbulence model to compare the hemolysis calculations using two different turbulence models. All the calculations are the same with the k-ω SST model except, we use the different stresses that are calculated by using the k- ε model. Results are shown in Table 5.4.

Table 5.4. Hemolysis calculations for four different power law models by using k-ε model

Power Law Models	**Type of Stress**	**Calculated HI for τ_w=100 Pa**	**Calculated HI for τ_w=200 Pa**	**Calculated HI for τ_w=300 Pa**	**Calculated HI for τ_w=400 Pa**	**Standard Error [100]**
Experimental Hemolysis Data [9]	τ_w	0.0954	0.1538	0.7625	1.9375	0
Giersiepen et al. [21]	τ_{Re}	1.0444	7.2103	21.8801	46.8193	9.7547
	τ_t	2.0132	11.8869	34.1216	70.8037	14.8321
	τ_v	0.0627	0.2067	0.4585	0.8122	0.2564
	τ_w	6.5674	38.7766	111.3085	230.9699	49.3428
Heuser et al. [22]	τ_{Re}	0.0109	0.0552	0.1406	0.2657	0.3725
	τ_t	0.0188	0.0833	0.2028	0.3735	0.3513
	τ_v	0.0011	0.003	0.0058	0.0094	0.4258
	τ_w	0.0497	0.2208	0.5372	0.9897	0.2126
Zhang et al. [24]	τ_{Re}	0.1109	0.5885	1.5549	2.9889	0.2249
	τ_t	0.1905	0.8886	2.2428	4.2034	0.469
	τ_v	0.0109	0.0315	0.0642	0.1057	0.4075
	τ_w	0.5049	2.3553	5.9447	11.1413	1.9226
Fraser et al. [23]	τ_{Re}	0.0091	0.0449	0.1125	0.2103	0.3841
	τ_t	0.0155	0.0673	0.1614	0.2943	0.3677
	τ_v	0.0009	0.0025	0.0049	0.0078	0.4261
	τ_w	0.0406	0.176	0.4217	0.7692	0.267

When we compare the k- ε model with k-ω SST model, the power law model of Heuser et al. [22] gives the lowest standard error. The highest error was again obtained by using Giersiepen's [21] power law model. When results were compared examining different stresses (Reynolds, viscous, total, and wall shear stresses), the best agreement between the experimental data and the power law models was obtained by using wall shear stress. The worst agreement was obtained by using wall shear stress with Giersiepen's [21] power law model. Also it can be seen that when Table 5.3 and Table 5.4 are compared only Reynolds and viscous stress results gave different hemolysis predictions because wall shear stress and the total stresses were same in both models. Table 5.5 summarizes the comparison of two models.

Table 5.5. Comparison of k-ε and k-ω SST models

Power Law Models	**Type of Stress**	**Standard Error by Using k-ε model**	**Standard Error by Using k-ω SST model**
Giersiepen et al. [21]	τ_{Re}	9.5747	**6.6658**
	τ_v	0.2564	**0.2485**
Heuser et al. [22]	τ_{Re}	**0.3725**	0.3861
	τ_v	0.4258	**0.4224**
Zhang et al. [24]	τ_{Re}	0.2249	**0.0557**
	τ_v	0.4075	**0.3686**
Fraser et al. [23]	τ_{Re}	**0.3841**	0.3947
	τ_v	0.4261	**0.4234**

As can be seen from Table 5.5, most of the time k-ω SST model gives the smallest standard error, which is shown as underlined and bold in the table, when compared to k-**ε** model.

One of the most significant findings of Kameneva et al. [9] was that turbulent and laminar flows with equal shear stress at the wall resulted in very different blood trauma. There are factors, therefore, in addition to wall shear stress that contribute to increasing hemolysis for turbulent flow conditions. The turbulence feature that leads to RBC trauma cannot be the Reynolds stresses acting the way viscous stresses act in laminar flows. Area averaged Reynolds, total, viscous, and wall shear stresses are plotted for the capillary tube in Figure 5.2.

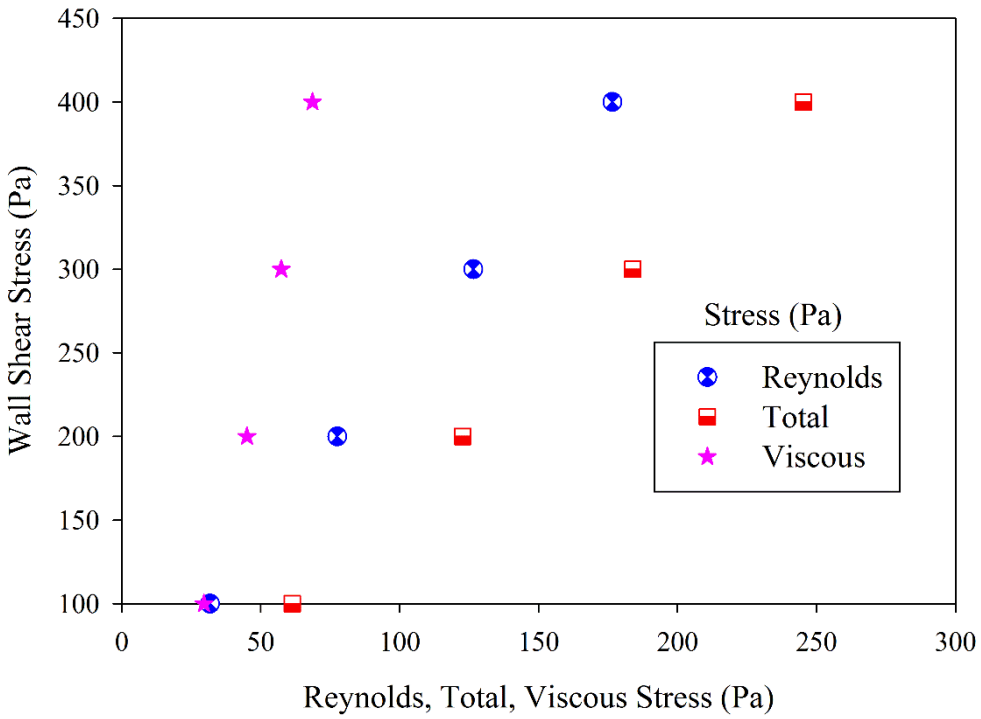

Figure 5.2. Changes of area averaged Reynolds, total, and viscous stress with four different wall shear stress.

It is seen that the Reynolds stresses in a turbulent flow with the same wall shear stress as in laminar flow are in fact smaller than the laminar flow shear stresses (when they were both area averaged). It is obvious from Figure 5.2 that Reynolds stress is less in magnitude than the total stress for the same wall shear stress. Moreover, viscous stress is the smallest when compared to Reynolds and total stress for the same wall shear stress.

5.4 Summary

When hemolysis predictions of 4 commonly accepted power law models of Giersiepen et al. [21], Heuser et al. [22], Zhang et al. [69], and Fraser et al. [23] were compared, the power law model of Zhang et al. [69] gives the lowest standard error. The highest error was obtained by using Giersiepen's [21] power law model. Moreover, use of the Reynolds stresses rather than the total stresses or the viscous stresses in the power law formula is found to provide better agreement between model and measurements. It is commonly known by the researchers that power law models are flow regime specific and cannot be applied to specific locations in medical devices.

6 Modelling Turbulent Flow and Cell Damage in a Jet

Portions of this chapter have been reproduced from the following source. This paper has been submitted for publication to PLOS ONE journal:

- Ozturk, M., Papavassiliou, D. V., & O'Rear, E. A. (2015). An approach to assessing turbulent flow damage to blood in medical devices. PLOS ONE.

6.1 Background

Jet flow provides high stresses in short exposure times, which is similar to typical flow conditions in prosthetic devices. Therefore, jets have been commonly used in hemolysis experiments to imitate the nature of the cardiovascular flows. Blackshear et al. [101] used jet flow to study hemolysis in turbulent flow and calculated Reynolds stresses for exposure times of 10^{-5}s. They found the critical Reynolds stress for hemolysis as 30,000 dynes/cm^2 which was similar to Forstrom's [57] jet experiment. Sallam and Hwang [48] also used jet flow to study hemolysis in turbulent flow. The critical Reynolds stress was found as 4000 dynes/cm^2 in exposure times of less than 100 s. Lu et al. [58] recalculated the threshold Reynolds stress of Sallam and Hwang [48] in a jet flow by using laser Doppler anemometer as 8000 dynes/cm^2 with an exposure time of 10^{-3} s. The threshold stress value of Sallam and Hwang [48] was also re-determined in the theoretical discussion of Grigioni et al. [102]. Their work was not an experimental study; instead they performed a 3D stress analysis and calculated the threshold value as 6000 dynes/cm^2 for exposure times of less than 10^{-2} s. In this study, the jet experiments of Forstrom [57], which is commonly cited in the literature by other researchers who also performed jet experiments, was modeled. Forstrom [57] determined the threshold stress value for

hemolysis as 40000 dynes/cm^2 for exposure times of 10^{-5} s. A summary of these studies is presented in Table 6.1.

Table 6.1. A review of hemolysis studies in jet flow for hemolysis

References for jet experiments	Exposure time (s)	Shear stress threshold for RBC damage (dynes/cm^2)	Flow field
Blackshear et al. [101]	10^{-5}	40000	Turbulent
Sallam and Hwang [48]	$<10^{-2}$	4000	Turbulent
Lu et al. [58]	10^{-3}	8000	Turbulent
Grigioni et al. [102]	$<10^{-2}$	6000	Turbulent
Forstrom [57]	10^{-5}	40000	Turbulent

6.2 Methods

6.2.1 Geometry and Computational Domain

The experimental apparatus of Forstrom [57] includes a blood syringe, a needle (jet), a fluid syringe, a hydraulic cylinder assembly, and a velocity measurement assembly (right image on Figure 6.1). Jet flow occurred at the exit of the needle into a fluid syringe, in which hemolysis measurements were taken. Therefore, only the needle and the fluid syringe were modeled in this work (shown within the red rectangle on the right image and separately on the left image on Figure 6.1).

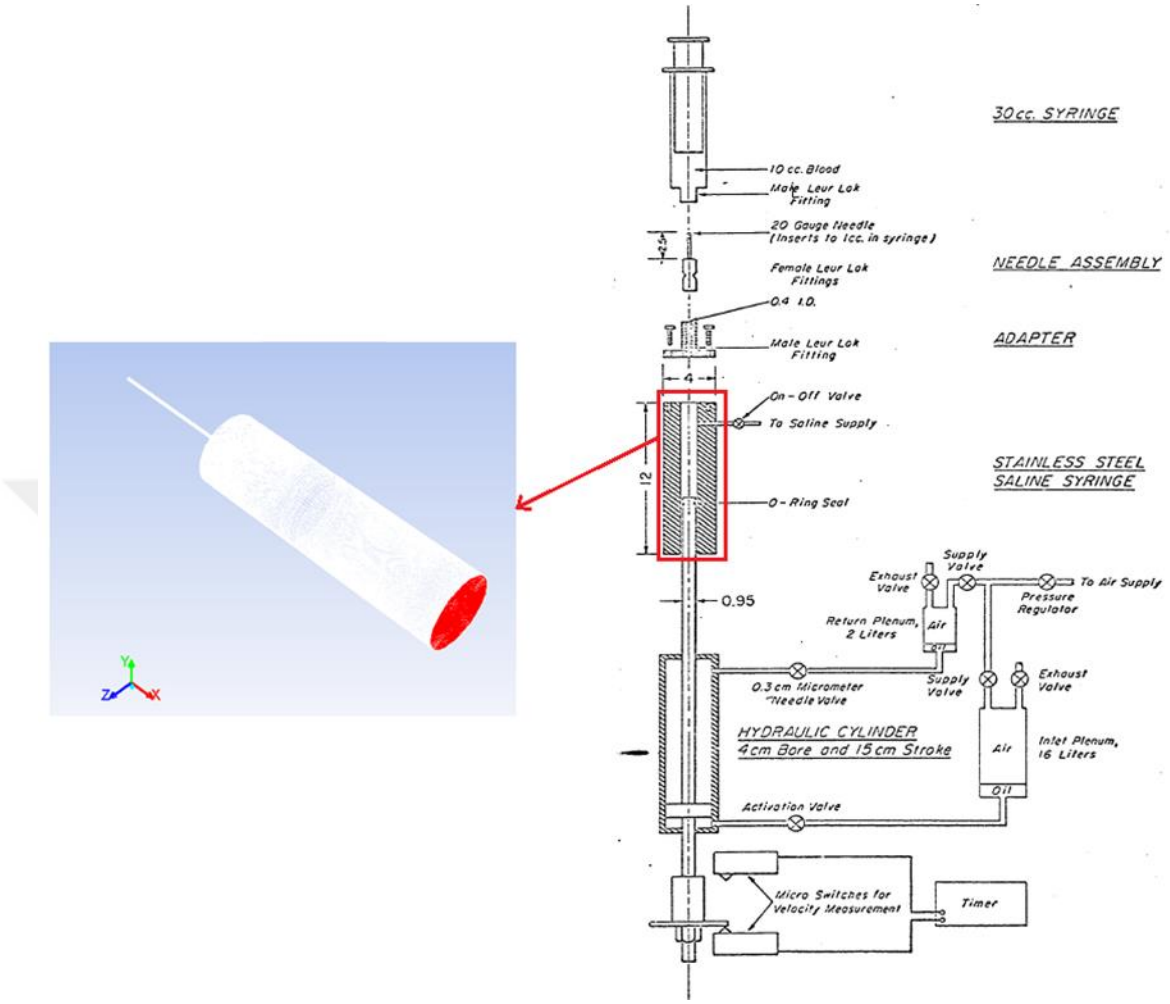

Figure 6.1. (L): 3D model of the jet (the needle and the syringe), (R): Experimental setup of Forstrom et al. [57]

In this study, conditions representing the environment of the actual jet experiment as described in reference [57] have been used. This included the geometries (dimensions, diameters, etc.), as well as the fluid properties and flow conditions. The diameter and the length of the needle were 0.0346 cm and 2.54 cm, respectively, and the syringe diameter was 1.9 cm with a length of 2.93 cm. Saline was injected through the needle to the fluid syringe, which was filled with human blood diluted with isotonic saline to a hematocrit

of 8%, at various velocities from 15.22 to 39.03 m/s (see Table 6.2). Hemolysis was determined for a stress period of 10^{-5} s.

6.2.2 Computational Mesh Development

The geometry was meshed using Fluent 14.0 and its preprocessing software ICEM CFD (Ansys, Pittsburgh, PA). A three dimensional model of the needle and syringe was recreated. Meshing the entire geometry with hexahedral elements was performed after the geometry was created. Moreover, element orthogonality and the mesh quality of the needle and the syringe were increased by using o-grids around the inlet and outlet regions. After mesh creation in ICEM CFD, the flow geometry was imported into Fluent to solve the incompressible Navier-Stokes equations. Mesh independence of the model was tested by refining the grid in regions of high mean velocity gradient until the percent difference for pressure loss and for the velocity profile at multiple cross sectional cuts between a more and less refined simulation solution was less than 3%. Several parameters were used to check grid independence and integrity. Mean velocity magnitude and turbulent kinetic energy results are shown in Figure 6.2. It can be seen from Figure 6.2 that velocity values and turbulent kinetic energy values were independent of the mesh size. The final mesh used for the jet flow simulation included 2,295,593 cells and 2,684,919 nodes.

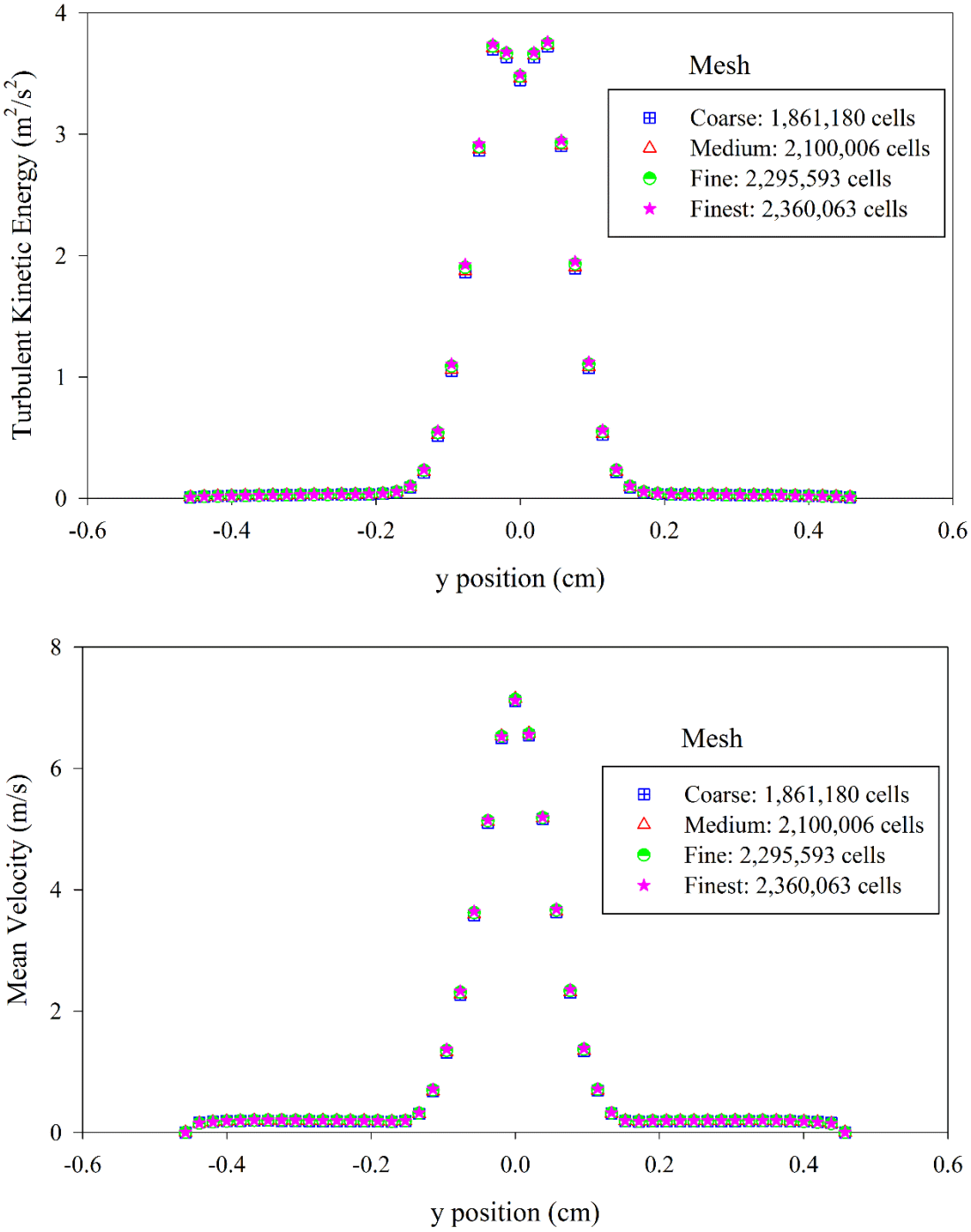

Figure 6.2. Top: Grid independence analysis for velocity for the highest velocity experiment (39.03 m/s) by using k-ω SST model Bottom: Grid independence analysis for turbulent kinetic energy for the highest velocity experiment (39.03 m/s) by using k-ω SST model.

6.2.3 Flow Simulations

The simulations were performed with the finite volume-based Fluent simulator. The boundary conditions for the jet consisted of velocity inlet at the domain inlet and the no-slip boundary condition on the walls. Solution parameters were specified as the 2nd order upwind discretization scheme, the *standard* interpolation scheme for pressure, and the *simple* scheme for pressure-velocity coupling. In the beginning of the simulations, a slow fluid velocity (such that the flow remained laminar) was assigned as the inlet velocity. The velocity was slowly increased until the resulting velocity equaled one of the experimental velocity values reported by Forstrom. [57] After the velocity attained a value high enough to yield turbulent flow, the k-ω SST turbulence model was applied. Selection of turbulence model (k-ε or k-ω SST) was based on comparison of simulation results to theoretical predictions (see details below). The procedure of increasing the velocity was repeated until all thirteen cases of different velocity values (15.22 - 39.03 m/s.) of the Forstrom [57] experiments had been simulated (Table 6.2). The fluid properties for all simulations of the jet consisted of a Newtonian model with a viscosity of 0.001 Pa.s and a density of 998 kg/m^3. The Reynolds number (Re) for different cases of jet experiments was determined as $Re = \frac{UD}{\upsilon}$ where U is velocity, D is jet diameter, and ν is kinematic viscosity. The range of Reynolds number was changing from 5241 (for the lowest velocity, 15.22 m/s) to 13,440 (for the highest velocity, 39.03), as seen in Table 6.2. Flow in the jet is fully turbulent, since these Reynolds numbers are higher than the commonly accepted range of critical Reynolds number for jet flow of 2000-3000.[103-107] Simulations were considered converged when residuals for the velocity components,

the continuity equation, and the equations of k, ε, and ω of the turbulence model fell below $1x10^{-5}$.

Table 6.2. Model conditions for the jet experiments [57]

% Experimental Hemolysis	Saline velocity (m/s)	Jet Reynolds number	Range of KLS (µm)
0.04	15.22	5241	1 - 168
0.07	17.08	5881	1 - 155
0.35	19.15	6594	1 - 153
0.66	20.39	7021	1 - 143
1.07	21.99	7572	1 - 139
1.76	23.59	8123	1 - 137
2.8	25.27	8702	1 - 133
4.06	27.41	9438	1 - 128
5.84	30.22	10,406	1 - 110
7.78	33.22	11,439	1 - 116
8.13	34.13	11,752	1 - 104
9.89	36.7	12,637	1 - 112
11.4	39.03	13,440	1 - 106

The validation of the turbulence models was conducted by simulating the jet experiment using both k-ε and k-ω SST turbulence models and then comparing simulation results with the theoretically predicted mean axial velocity, <U> profile and the spreading rate of the turbulent jet. [41] To compare the mean axial velocity profile, the centerline velocities, U_0, and the jet half widths, $r_{1/2}$, were calculated at different x/d values, in which x is the axial distance from the jet exit and d is the jet diameter. According to theory, when the axial distance (x) increases, the jet decays with decreasing U_0, and by increasing

of $r_{1/2}$. While the jet spreads and decays, the mean velocity profile changes, but the shape of the profile does not change. Moreover, when the profile of $<U>/U_0$ is plotted with $r/r_{1/2}$, all the curves at different x/d regions should collapse onto a single curve – in other words the mean velocity profile becomes self-similar. [41] The mean velocity profiles for both k-ε and k-ω SST turbulence models at different x/d regions are plotted on Figure 6.3. Moreover, simulation results were compared to theory [98] using the following equations

$$\langle U_x \rangle = \frac{\nu^{(t)}}{x} \frac{2C_3^2}{\left[1+\frac{1}{4}\left(C_3 r / x\right)^2\right]^2} \qquad \textbf{6.1}$$

where $<U_x>$ is the mean velocity in x direction, $\nu^{(t)}$ is the eddy viscosity, C_3 is a constant, r is the radial distance, and the x is the axial distance. It can be seen from Figure 6.3 that using either the k-ε or the k-ω SST model in the computation of the flow domain does not result in significant differences and both agree with theory by demonstrating self-similarity at different x/d locations. [41]

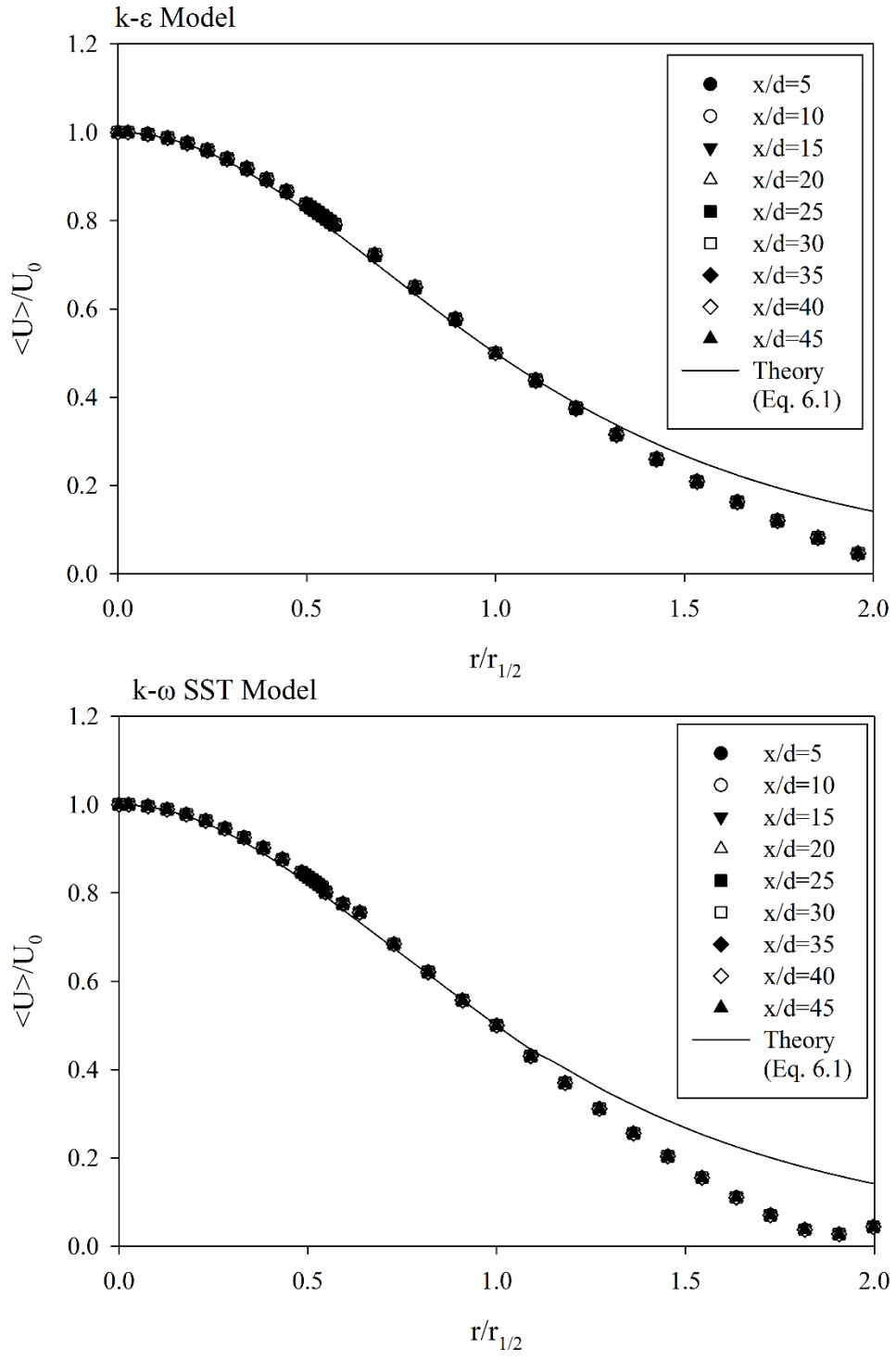

Figure 6.3. Top: Mean axial velocity profile as a function of radial distance for k-ε turbulence model at different x/d locations. Bottom: Mean axial velocity profile as a function of radial distance for k-ω SST turbulence model at different x/d locations. The jet velocity for both models was 20.39 m/s.

To compare the spreading rate, the variation of mean velocity along the centerline at different axial distances were calculated. According to theory, the ratio U_j/U_0 , where U_j is the jet exit velocity, should be linear with x/d, and should obey the following decay equation:

$$\frac{U_j}{U_0(x)} = \frac{(x-x_0)/d}{B} \qquad \textbf{6.2}$$

where x_0 is the virtual origin of the jet and B is the velocity decay constant. [41] Moreover, it is theoretically expected that the jet spreading rate, S, should be constant. The jet spreading rate is defined as follows: [41]

$$S \equiv \frac{dr_{1/2}(x)}{dx} \qquad \textbf{6.3}$$

$$r_{1/2}(x) = S(x-x_0) \qquad \textbf{6.4}$$

The value of the spreading rate found from theory with boundary layer equations in a turbulent round jet is given as [41]

$$\frac{r_{1/2}}{U_0^2}\left(\langle U\rangle \frac{\partial\langle U\rangle}{\partial x}\right)_{r=0} = -S \approx -0.094 \qquad \textbf{6.5}$$

As can be seen from Equation 6.5, the theoretical value for spreading rate is given as 0.094. The variation of mean velocity and spreading rate for both k-ε and k-ω SST turbulence models were plotted on Figure 6.4. As can be seen from Figure 6.4, both k-ε and k-ω SST turbulence models show linear behavior as discussed above.

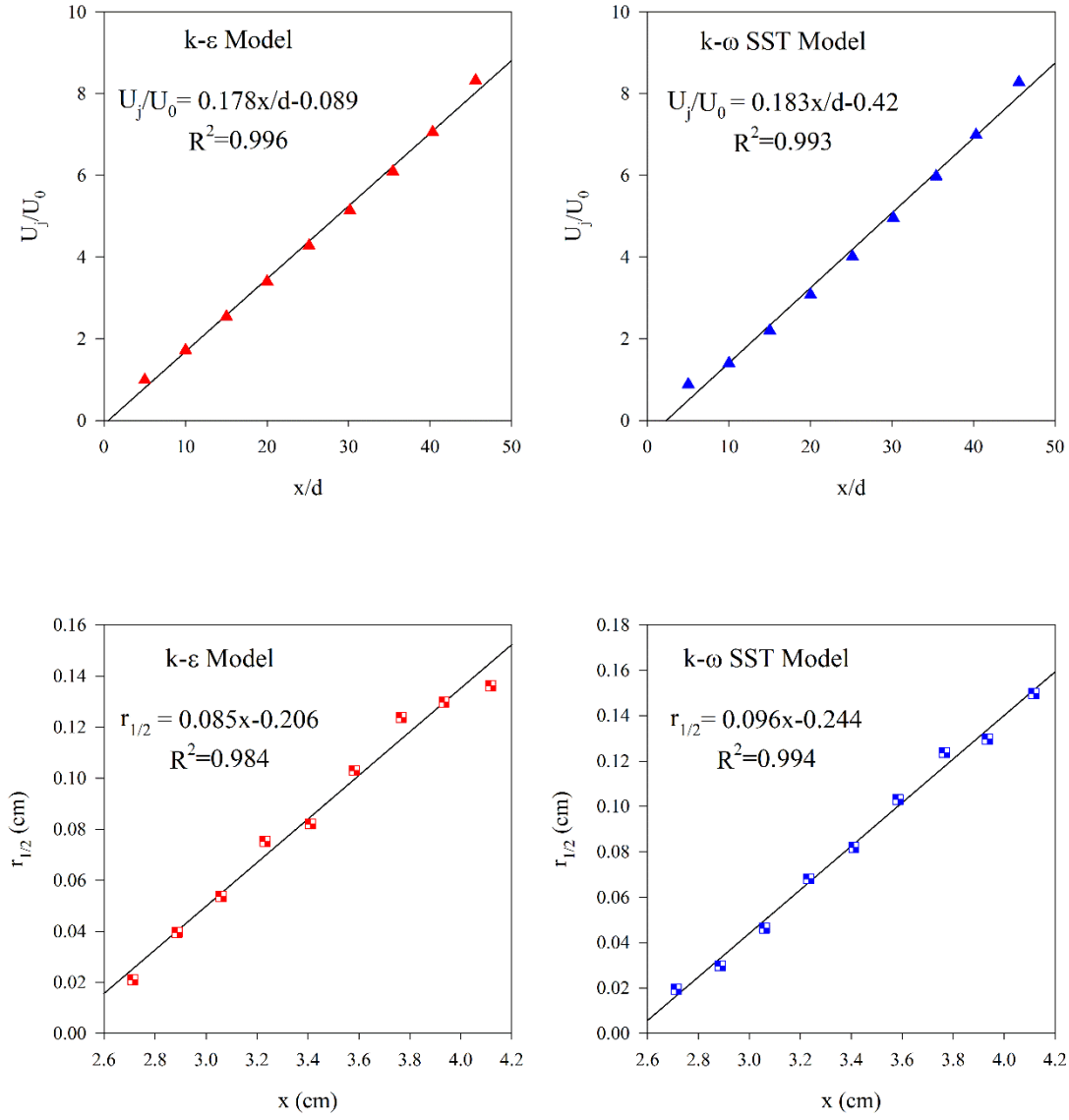

Figure 6.4. Left: Variation of spreading rate (top panel) and variation of mean velocity along the centerline (bottom panel) at different axial distances for k-ε turbulence model. Right: Variation of spreading rate (top panel) and variation of mean velocity along the centerline (bottom panel) at different axial distances for k-ω SST turbulence model. The jet velocity for these runs was 20.39 m/s.

The velocity decay constants and the spreading rates were calculated for both k-ε and k-ω SST turbulence models and compared with the theoretical values on Table 6.3.

Table 6.3. The spreading rate, S, and velocity decay constant, B for turbulent round jets. Simulation results are for a jet with U_0 (x=0) = 20.39 m/s.

	Theoretical value [41]	Panchapakesan and Lumley [108]	Hussein et al. [109] (hot-wire data)	Hussein et al. [109] (laser-Doppler data)	k-ε results	k-ω SST results
S	0.094	0.096	0.102	0.094	0.085	**0.096**
B	empirical constant	6.06	5.9	5.8	5.61	**5.45**

As can be seen from the comparison in Table 6.3, the k-ε and k-ω SST turbulence models give slightly different results while obeying the theoretically predicted behavior. For this study, k-ω SST turbulence model was chosen because the k-ω SST model results in a spreading rate, S, value closer to the theoretical value of 0.094.

6.3 Results and Discussion

6.3.1 Relation between Eddy Size Distribution and KLS

Each specific experimental jet flow condition was simulated and the fluid flow simulations produced time-averaged spatial distributions of the Kolmogorov length scale (KLS). The main assumptions underlying our procedure have been presented in Section 2.5. Eddy analysis in the virtual jet was started by calculating the KLS values in the whole flow domain for each experiment (Table 6.2). Regions with similar turbulence intensity were assumed to be characterized by spherical eddies with sizes reflected by KLS values.

The number and the surface area of eddies for each KLS value were calculated from the total volume for that region as demarcated by its KLS value. The analysis was performed between the jet exit and the outlet of syringe since the experimental hemolysis data were derived from that region. [57] A series of vertical planes along and perpendicular to the jet axis were created that can be seen on Figure 6.5.

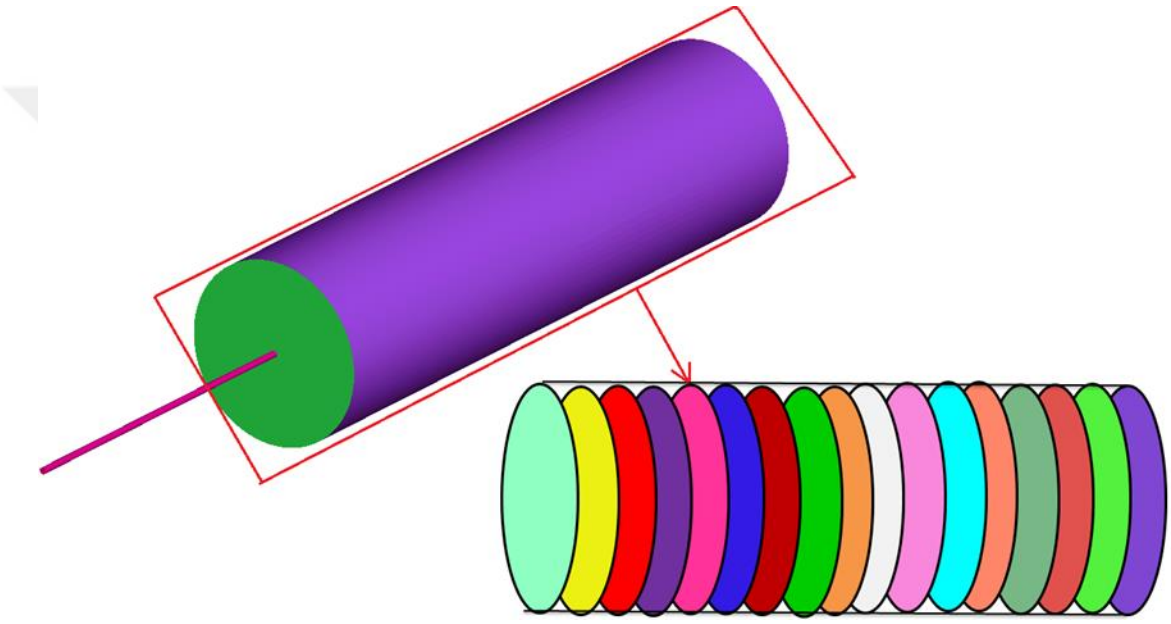

Figure 6.5. Planes in syringe for eddy analysis. The syringe was divided by 53 planes spaced as indicated in Figure 6.6.

The distance between planes were chosen small to capture the whole domain. As can be seen on Figure 6.6, near the jet exit the distance between planes were chosen as 1 jet diameter (0.0346 cm), and the distance were chosen in the range of 1.5 jet diameter (0.0519 cm) to 3 jet diameters (0.1038 cm) starting from the middle of the syringe up to the end.

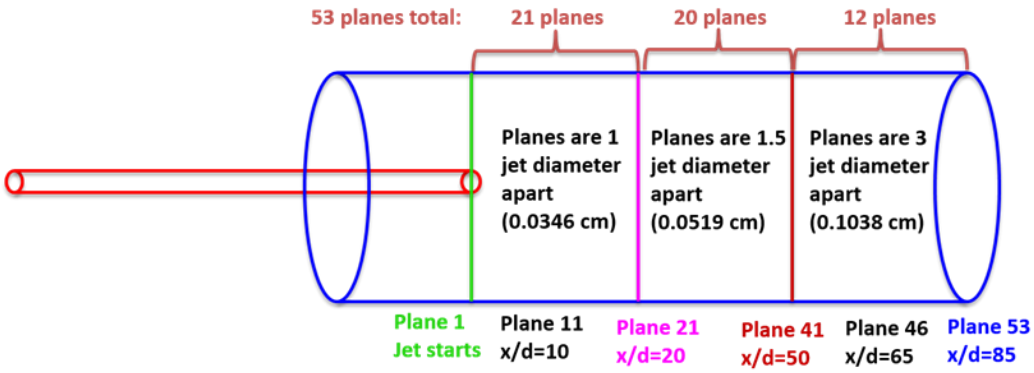

Figure 6.6. Positions and the number of planes in syringe.

On each created plane the KLS values were different. For only one jet experiment (20.38 m/s), the KLS values are shown in Table 6.4 (others are not shown for simplicity). For every plane out of 53 total planes, contour surfaces were created for each KLS in KLS bins of 1µm. For example; for plane 1, 143 different contour surfaces were created that correspond to the KLS range of plane 1 and 135 different contour surfaces were created for plane 2. This analysis was completed for all of the 53 planes, as shown in Table 6.4, to complete the 20.38 m/s experiment. The total number of contour surfaces for only 20.38 m/s jet experiment were around 7000. After data collection for this experiment was completed, the rest of the 12 experiments were analyzed the same way. The complete range of experimental conditions are shown in Table 6.2. The intersection of these planes with surfaces of constant KLS values defined volumes for eddy analysis.

Table 6.4. KLS values on planes for the 20.38 m/s jet experiment. After first 3 column (in pink color), the table continues on the next 3 columns (in yellow color). Plane 1 was located at the jet exit, and rest of the planes continue until the end of the syringe, where plane 53 was located.

Distance in x, cm	Plane name	KLS (min, max), µm	Distance in x, cm	Plane name	KLS (min, max), µm
2.54	plane_1	0.85 – 143.33	3.5953	plane_28	4.91 – 21.24
2.5746	plane_2	0.84 – 135.34	3.6472	plane_29	5.18 – 19.70
2.6092	plane_3	0.99 – 126.77	3.6991	plane_30	5.44 – 17.74
2.6438	plane_4	1.09 – 118.19	3.751	plane_31	5.70 – 16.99
2.6784	plane_5	1.27 – 109.96	3.8029	plane_32	5.97 – 17.04
2.713	plane_6	1.37 – 102.30	3.8548	plane_33	6.23 – 16.36
2.7476	plane_7	1.42 – 95.24	3.9067	plane_34	6.49 – 15.78
2.7822	plane_8	1.48 – 88.67	3.9586	plane_35	6.75 – 15.32
2.8168	plane_9	1.55 – 82.34	4.0105	plane_36	7 – 14.95
2.8514	plane_10	1.64 – 76.21	4.0624	plane_37	7.26 – 14.67
2.886	plane_11	1.74 – 70.45	4.1143	plane_38	7.51 – 14.45
2.9206	plane_12	1.85 – 65.32	4.1662	plane_39	7.75 – 14.35
2.9552	plane_13	1.98 – 60.89	4.2181	plane_40	7.99 – 14.31
2.9898	plane_14	2.11 – 56.81	4.27	plane_41	8.22 – 14.34
3.0244	plane_15	2.25 – 52.55	4.3738	plane_42	8.67 – 14.55
3.059	plane_16	2.39 – 48.25	4.4776	plane_43	9.13 – 14.91
3.0936	plane_17	2.54 – 44.43	4.5814	plane_44	9.64 – 15.38
3.1282	plane_18	2.69 – 41.64	4.6852	plane_45	10.20 – 15.92
3.1628	plane_19	2.84 – 39.68	4.789	plane_46	10.83 – 16.56
3.1974	plane_20	2.996 – 37.70	4.8928	plane_47	11.53 – 17.40
3.232	plane_21	3.15 – 35.70	4.9966	plane_48	12.92 – 18.65
3.2839	plane_22	3.39 – 33.46	5.1004	plane_49	15.51 – 20.21
3.3358	plane_23	3.64 – 32.43	5.2042	plane_50	17.997 – 22.30
3.3877	plane_24	3.88 – 30.14	5.308	plane_51	18.62 – 23.17
3.4396	plane_25	4.14 – 25.32	5.4118	plane_52	17.89 – 22.94
3.4915	plane_26	4.39 – 22.08	5.47	plane_53	17.18 – 22.76
3.5434	plane_27	4.65 – 21.47 Continues on top→			

The total volume of regions containing dissipative eddies of similar spherical size was calculated by multiplying the interplanar distance of the segmented computational domain by the cross-sectional surface area of a region that was radially bounded by contours of KLS with increments of 1μm. After calculating the total volume and the number of eddies, the results were normalized by calculating eddy surface area, eddy number, and eddy volume per-unit-volume to create quantities that might be compared for different turbulent flow situations and experimental configurations. We normalized our results by dividing with the total volume over which hemolysis is thought to occur. Our previous results [61] suggest smaller eddies are more damaging, so we used the total volume of the region in which $KLS \leq 10\,\mu m$. The goal was to determine the correspondence of hemolysis with extensive quantities rather than intensive, on a per unit volume basis for different values of KLS. In addition, cumulative values of these extensive quantities with increasing values of KLS were considered.

The calculated KLS values ranged from 1μm to 106 μm for the highest velocity experiments (39.03 m/s), while the maximum value of KLS was up to 168 μm for the lowest velocity experiments (15.22 m/s). The complete range of KLS and experimental conditions are shown in Table 6.2. The time-averaged spatial distribution of KLS values on several lines at different axial positions of the syringe starting from the jet exit (x/d=0) for the highest velocity experiment is shown in Figure 6.7.

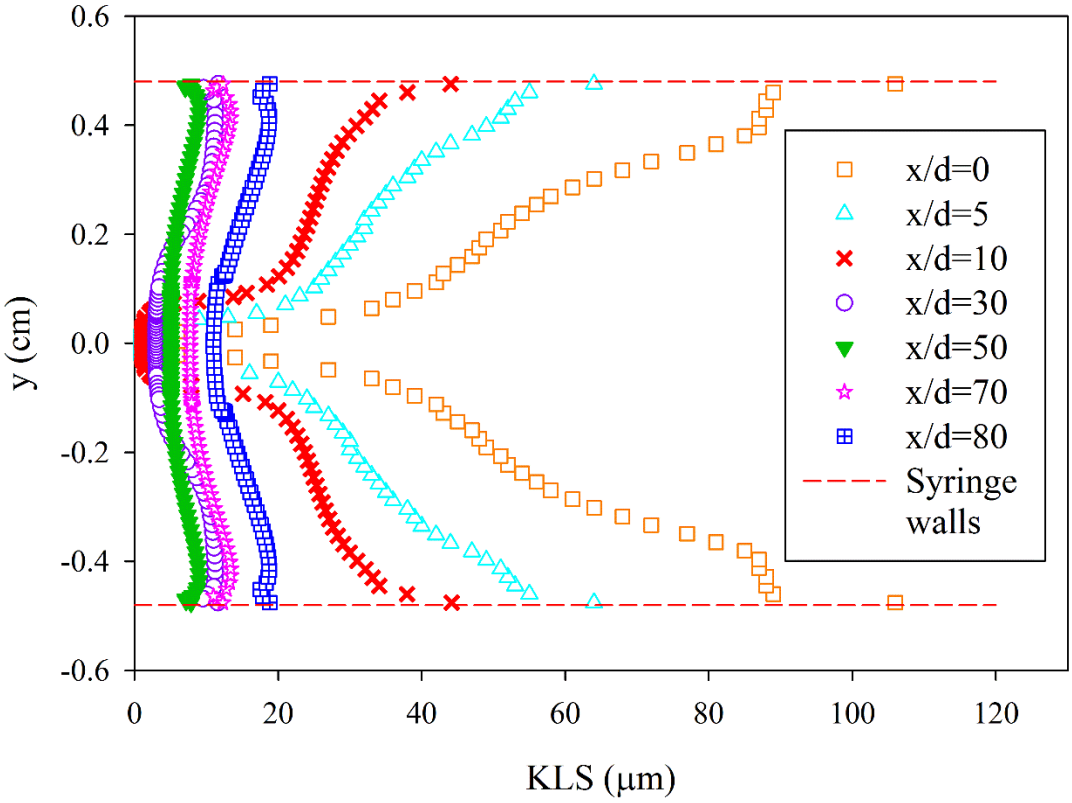

Figure 6.7. Changes of KLS values with increasing axial distance in the syringe starting from jet exit (x/d=0) to the syringe end (x/d=80) for the highest velocity experiment.

It can be seen from Figure 6.7 that KLS values varied radially as well as axially. For a given axial location, turbulence is more intense near the centerline (y=0) as indicated by smaller values of KLS. It can be seen that the turbulence intensity spreads radially as the distance from the jet increases. Moreover, since this study considers that smaller KLS values ($KLS \leq 10\,\mu m$) cause more damage, the regions containing small KLS values (from $KLS \leq 5$ to $KLS \leq 10$) were found for the highest velocity jet experiment as can be seen on Figure 6.8. The same analysis was also made for lower velocity jet experiments and it was found that the higher velocity created a larger region of smaller KLS values. This finding suggests that a larger region of smaller eddies ($KLS \leq 10\,\mu m$) is associated

with more hemolysis, since the highest velocity jet experiment exhibits the most hemolysis (Table 6.2).

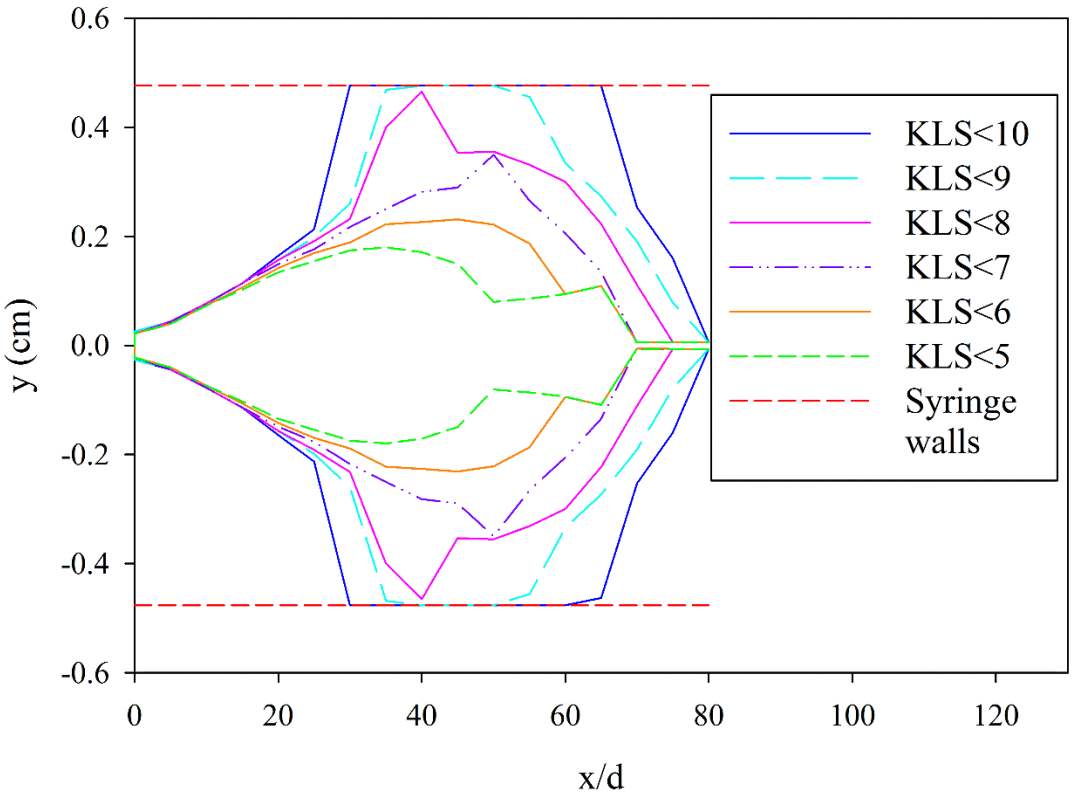

Figure 6.8. Regions showing from KLS ≤ 5 to KLS ≤ 10 in syringe for the highest velocity (39.03 m/s) experiment.

The size distributions of dissipative eddies were calculated based on KLS values for all 13 of Forstrom's jet experiments (Table 6.2). These eddy size distributions are plotted on Figure 6.9. Results showed that for the highest velocity experiments, which exhibited higher hemolysis, the number of smaller eddies increased. The size distribution also shifted to smaller values with simulations for increasing velocity.

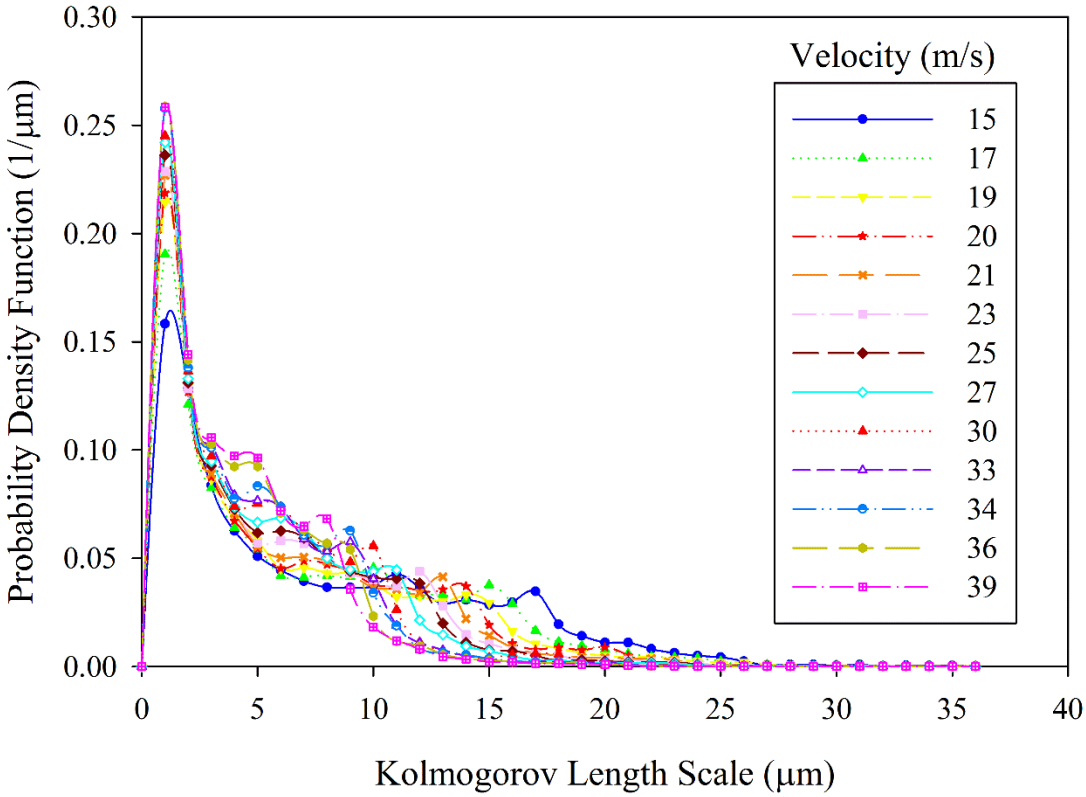

Figure 6.9. Probability distribution of KLS values in the jet for different mean jet velocities (39 m/s – 15 m/s). The area under the each curve is equal to 1.

The relation between distributions of eddies and hemolysis was also examined. The distribution of eddies was calculated by summing the number of eddies up to a specific KLS and plotting with experimental hemolysis on Figure 6.10. As can be seen from Figure 6.10, the greater dependence to hemolysis can be seen for KLS curves up to 10 μm. After this value, the dependence is becoming unimportant (this can be inferred from observing vertical KLS curves for larger KLS values). This finding suggests that blood damage in turbulent flow could be predicted by exploring more closely the role of Kolmogorov length scale as proposed previously by others, and as suggested by our work for capillary flow and Couette flow.

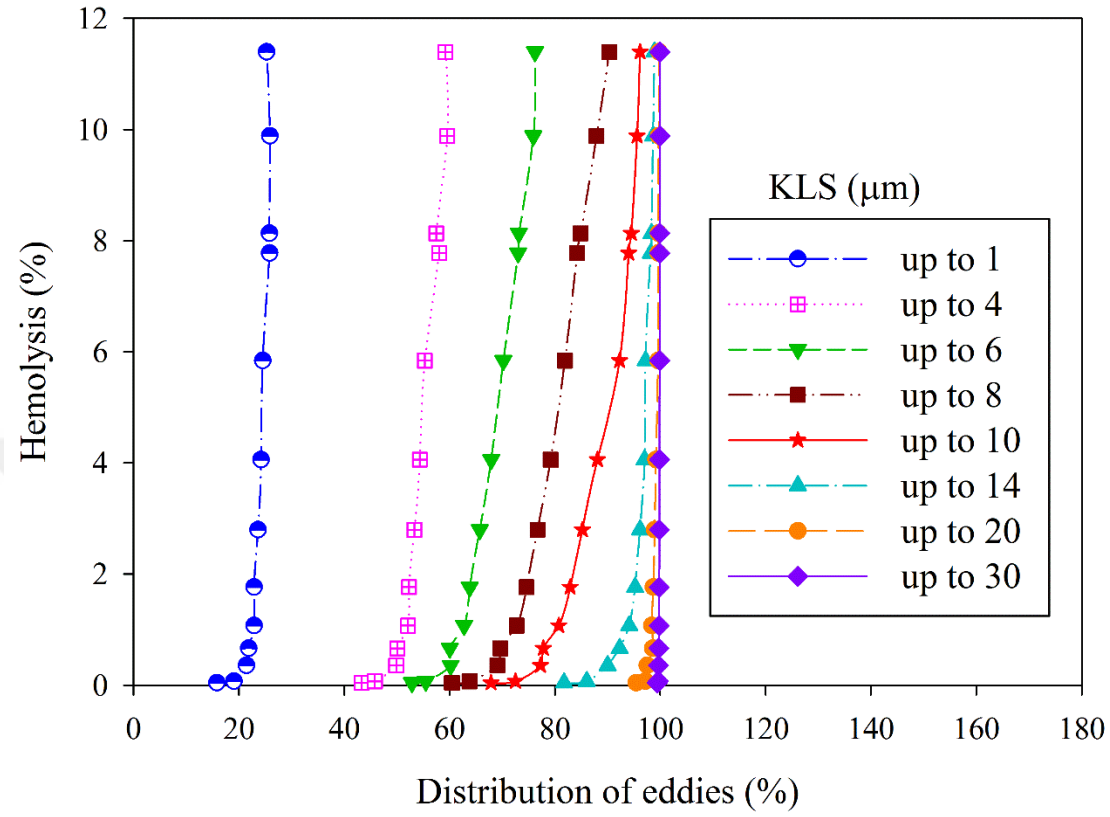

Figure 6.10. Relation between KLS distributions and hemolysis up to specific KLS values. Each data point corresponds to observed hemolysis reported in the experiment.

6.3.2 The Effect of Eddy Surface Area on Hemolysis

The surface area of KLS-sized eddies per unit volume has been calculated for the thirteen experiments in the jet as a function of KLS values. Analysis to find a relation between eddy area and hemolysis continued by combining experimental results for jet with the simulation results. A plot of eddy surface area per volume and hemolysis is shown in Figure 6.11. The analysis was done for every 1 µm KLS values, but only odd KLS values are presented for clarity. Please note that in the figures of the rest of the results section, each data point corresponds to observed hemolysis reported in the

experiments of Forstrom, [57] while the eddy area (or eddy number, or eddy volume) for the specified KLS size as found from simulation of that experiment. The lines are plotted to guide the eye over the data points. In the jet experiment, % hemolysis was not given directly in the original work. [57] We calculated hemolysis using the formula [22] $H(\%) = \frac{\Delta Hb}{Hb} * 100$ where H is the percentage of hemolysis, ΔHb is change of plasma hemoglobin as hemoglobin is released, and Hb is the total amount of hemoglobin. ΔHb values were digitized from original work [57] and Hb was given in the original work [57] (hemolysis values can be seen on Table 6.2).

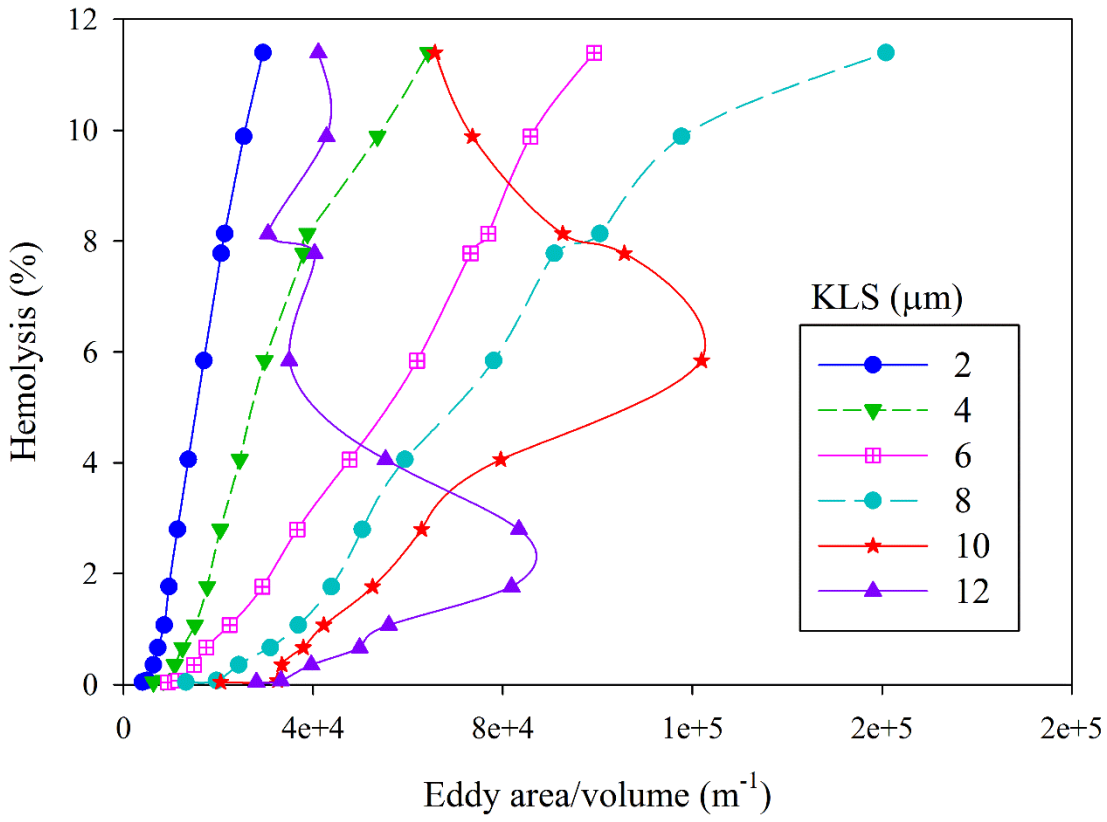

Figure 6.11. Hemolysis as a function of eddy surface area in jet for even values of KLS (experimental data from Forstrom [57], as seen on Table 6.2).

As can be seen from Figure 6.11, the shape of the lines changes when KLS values go from 8 to 10 μm. For KLS larger than 10 μm, the lines curve back and up, and become vertical for larger KLS values, suggesting no apparent dependence of hemolysis on the presence of such eddies in this flow field.

Figure 6.11 shows that eddies below a certain size are related to hemolysis and the critical eddy size for the jet experiment is 10 μm. Furthermore, the cumulative eddy area, which provides deeper understanding than eddy area binned in KLS bins of 1 μm, was also investigated. It would offer an overall assessment of cell damage due to eddies of different sizes. Cumulative effects of all eddies with a size less than a critical value was examined by summing up the KLS eddy surface area as the KLS values increased. Figure 6.12 is a plot of the relation between cumulative sum of eddy surface area and % hemolysis. It is clear from Figure 6.12 that hemolysis increases with increasing KLS eddy area per volume. Only even values of KLS values are shown for clarity. Note that, for higher KLS values, the curves begin to overlap with each other especially for KLS values of KLS > 10 μm.

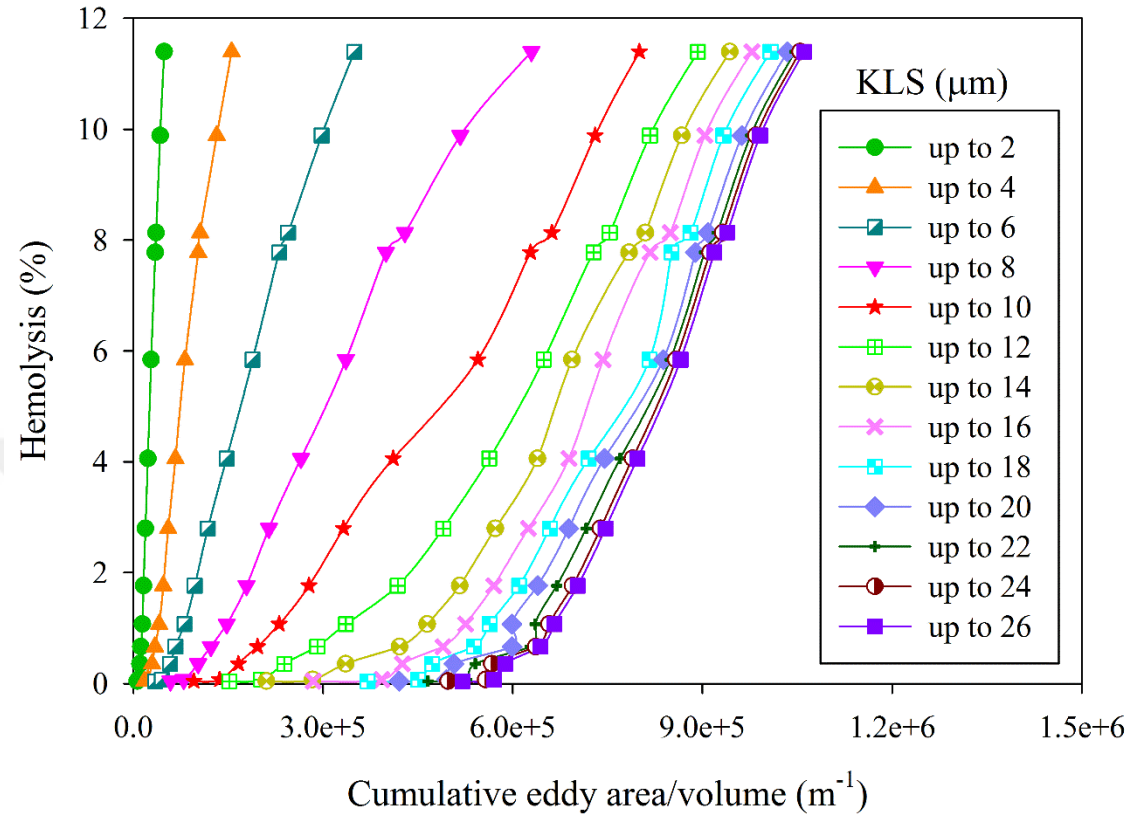

Figure 6.12. Hemolysis as a function of cumulative eddy area in the jet for even values of KLS.

6.3.3 The Effect of Eddy Number on Hemolysis

The eddy numbers for every KLS size were calculated for all thirteen experiments of the jet experiment. Then, results for each experiments were combined and analyzed together and plotted with experimental hemolysis data (Table 6.2). A relationship between eddy number per volume and hemolysis is shown in Figure 6.13.

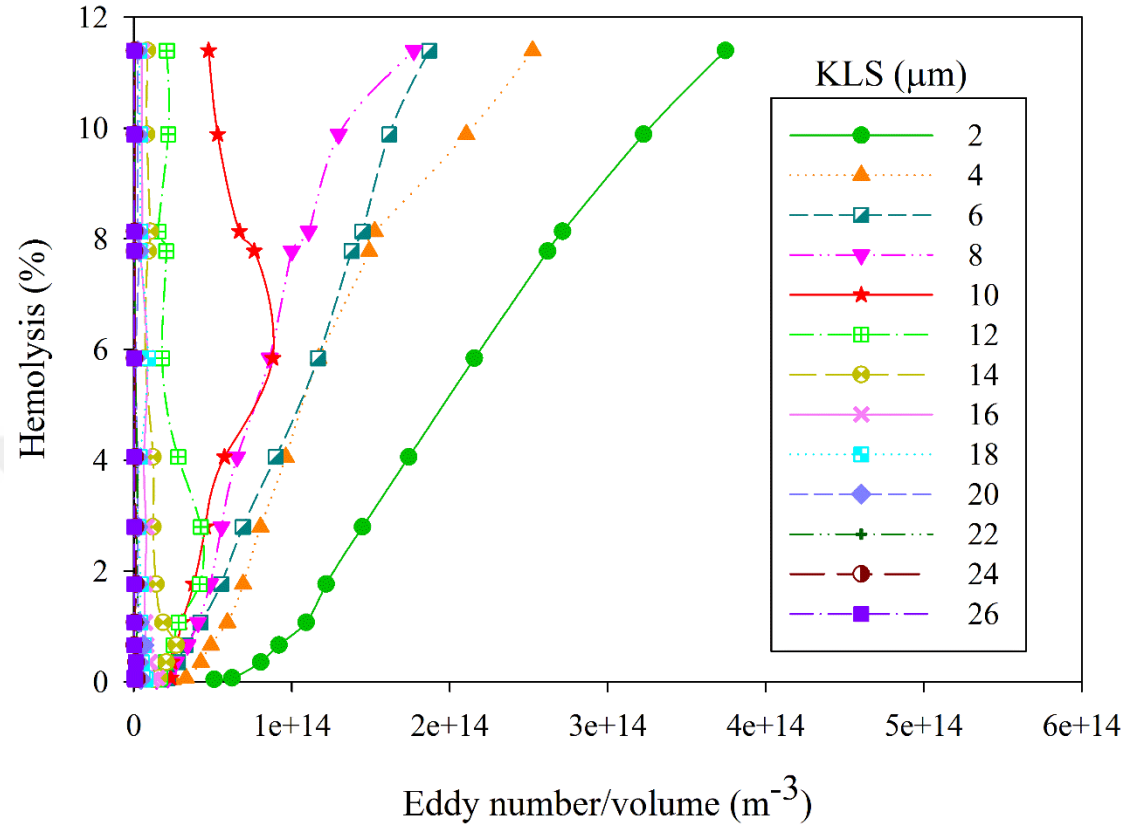

Figure 6.13. Hemolysis as a function of eddy number in the jet for even values of KLS.

Similar results with eddy area are also obtained with eddy number. The shape of the lines are changing as KLS values go from 8 to 10 µm. For KLS above 10 µm, the lines curve back and up, suggesting no apparent dependence of hemolysis on the presence of eddies in this flow field.

Additionally, the cumulative effect of all eddies were also examined for eddy number. Eddy number were summed up to a specific size and then plotted with hemolysis in Figure 6.14.

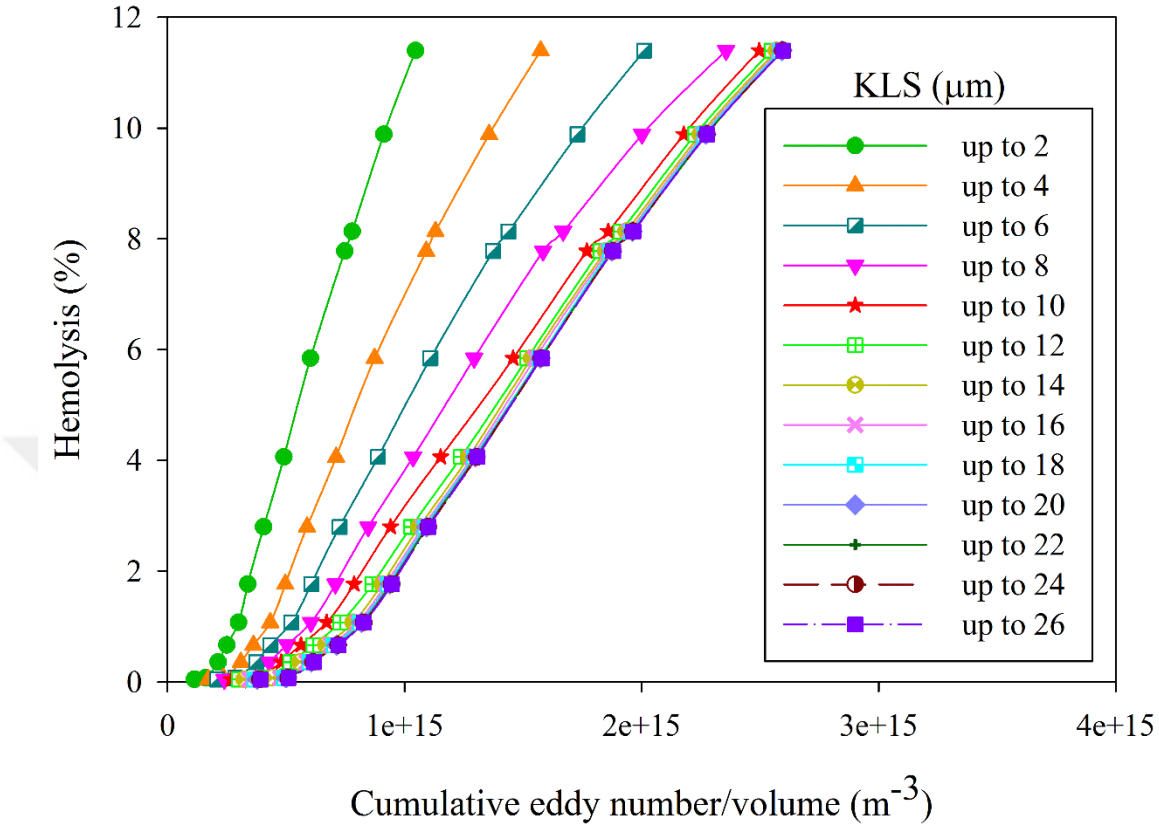

Figure 6.14. Hemolysis as a function of cumulative eddy number in the jet for even values of KLS.

As can be seen from Figure 6.14, hemolysis is increasing with increasing number of KLS eddies. Also, for KLS values larger than 10 µm, the lines start to overlap suggesting that larger KLS values do not contribute to hemolysis, which strentghens the argument that the critical KLS value is 10 µm.

6.3.4 The Effect of Eddy Volume on Hemolysis

Similar analysis with eddy area and eddy number was performed for the total eddy volume. Eddy volumes were calculated and analyzed together for the experiments of jet

(Table 6.2). The calculated eddy volumes and experimental hemolysis is plotted in Figure 6.15.

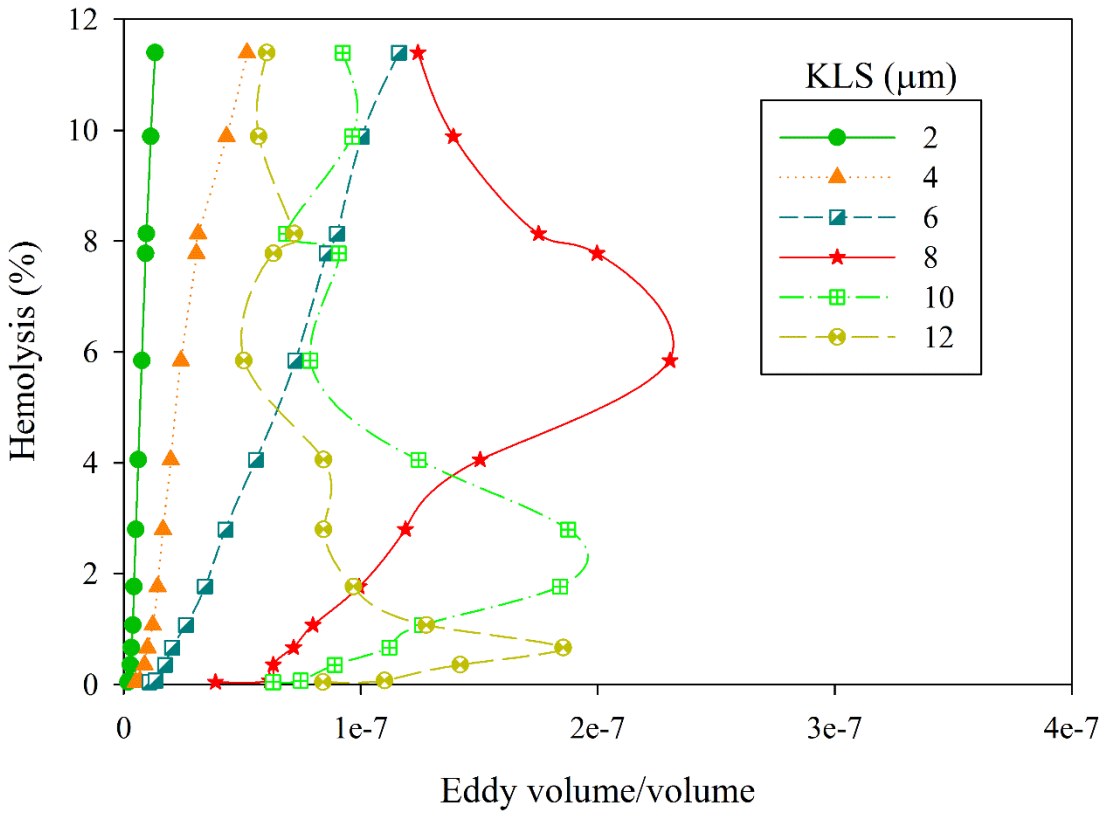

Figure 6.15. Hemolysis as a function of eddy volume in the jet for even values of KLS.

As can be seen from Figure 6.15, the lines change their shapes becoming vertical when KLS increases from 8 to 10 μm.

Additionally, the cumulative effect of all eddies was also examined for eddy volume. Eddy volumes were summed up to a specific size and then plotted with hemolysis in Figure 6.16.

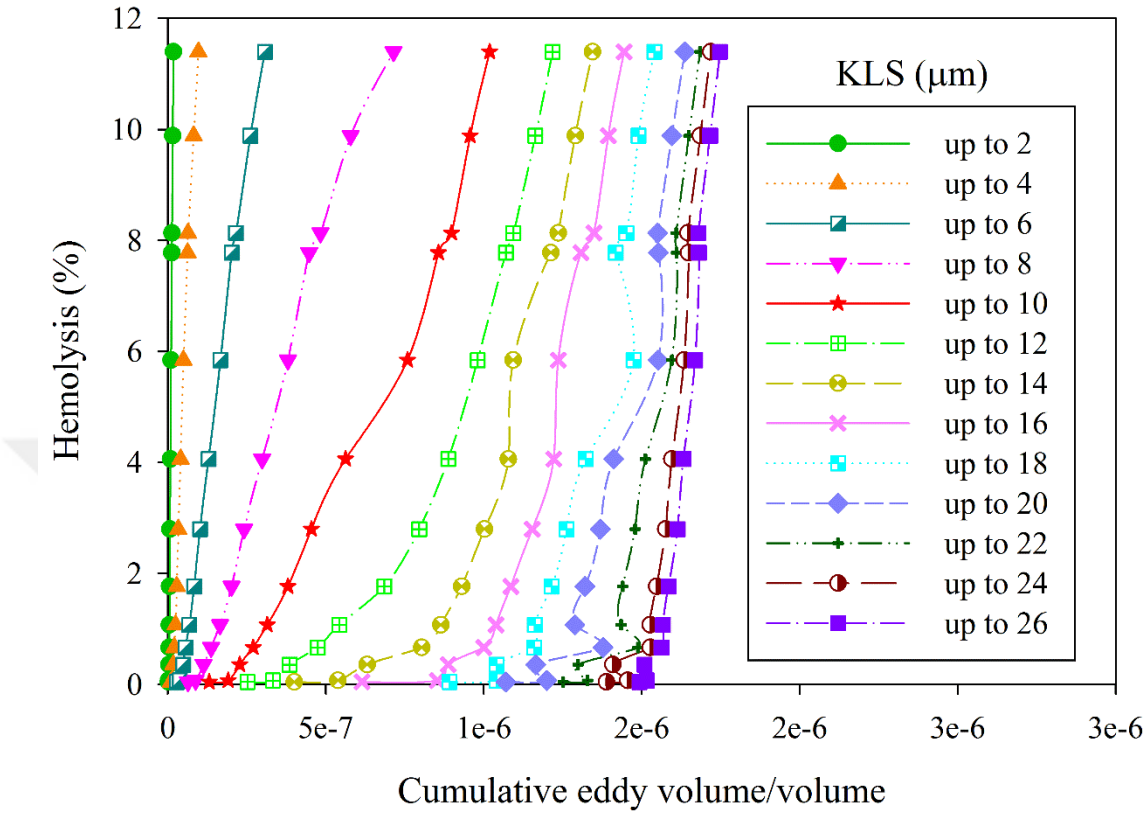

Figure 6.16. Hemolysis as a function of cumulative eddy volume in the jet for even values of KLS.

As can be seen from Figure 6.16, hemolysis is increasing with increasing volume of KLS eddies. Moreover, curves for larger KLS values are overlapping as well as tending to become vertical suggesting no effect on hemolysis for larger KLS values.

6.4 Summary

Results showed that there is a clear relationship between hemolysis and the total surface area of eddies with diameters of up to about 10 µm. A relation was not evident for larger eddies. This result supports our previous results (presented in Sections 3 and 4) in which two very different experiments, a Couette viscometer [60] and a capillary tube [9] were analyzed.

7 Hemolysis Model for Systems of the Couette viscometer, the Capillary Tube and the Jet

Portions of this chapter have been reproduced from the following sources. These papers have either been published or submitted for publication in peer-review journals:

- Ozturk, M., O'Rear, E. A., & Papavassiliou, D. V. (2015). Hemolysis related to turbulent eddy size distributions using comparisons of experiments to computations. Artificial Organs, 39(12), E227-E239. Doi: 10.1111/aor.12572.

- Ozturk, M., Papavassiliou, D. V., & O'Rear, E. A. (2015). An approach to assessing turbulent flow damage to blood in medical devices. PLOS ONE.

7.1 Introduction

As already discussed in Section 1.2, power law models are missing the general flow features of typical medical devices because they were derived from steady viscometer experiments with uniform shear stress. Therefore, we propose a new hemolysis model based on experimental results from three distinctly different devices; a jet [57], a Couette viscometer [60], and a capillary tube [9]. We assume that hemolysis is related to the surface area of eddies with sufficient stress and energy intensity to damage the cell. This way hemolysis can be examined based on an extensive property (eddy surface area) throughout the domain of turbulent flows.

7.2 Methods

A series of tests was performed to find the best empirical model for all three systems that have varying levels of hemolysis as discussed in Sections 3, 4, and 6. The levels of hemolysis for the Couette viscometer experiments are changing from 1% to

85%, while for the capillary tube and the jet experiments hemolysis are changing from 0.09% to 1.9% and from 0.04% to 11.4 %, respectively. The experimental hemolysis values of less than 5% were chosen to be used in the three systems, since more than 5% hemolysis is clinically irrelevant.

7.3 Results and Discussion

To find the best fit to the Couette viscometer, the capillary tube, and the jet, regression analysis of different functions was carried out. The biggest challenge to find the best fit for these systems was the big differences between them. They are different in terms of exposure times, geometries, stress ranges and exposure type to stresses being continuous and cumulative. The capillary tube has multiple exposures in a flow loop as explained in Section 4.2. First of all, to better observe the difference between 3 systems, 3D plot of eddy area per volume is plotted on Figure 7.1.

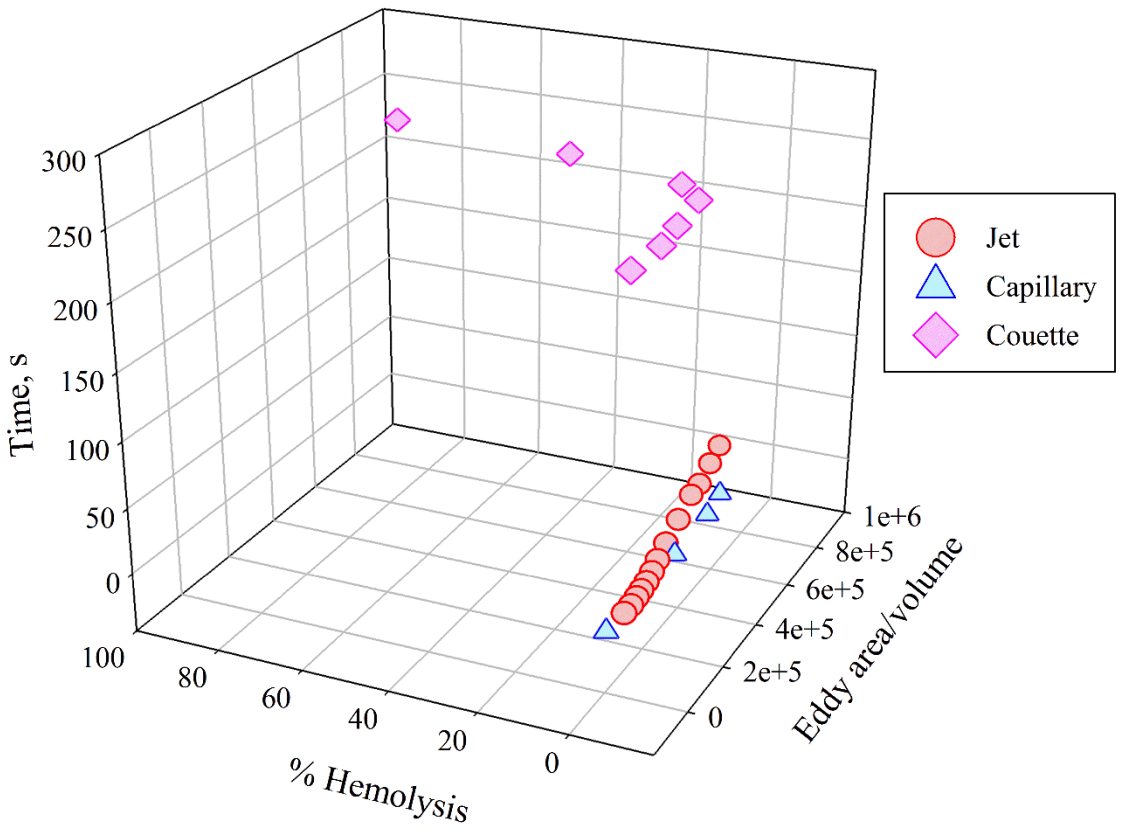

Figure 7.1. Eddy area per volume for the Couette viscometer, the capillary tube, and the jet.

Similar with the eddy area per volume, eddy number per volume is also plotted for three systems together.

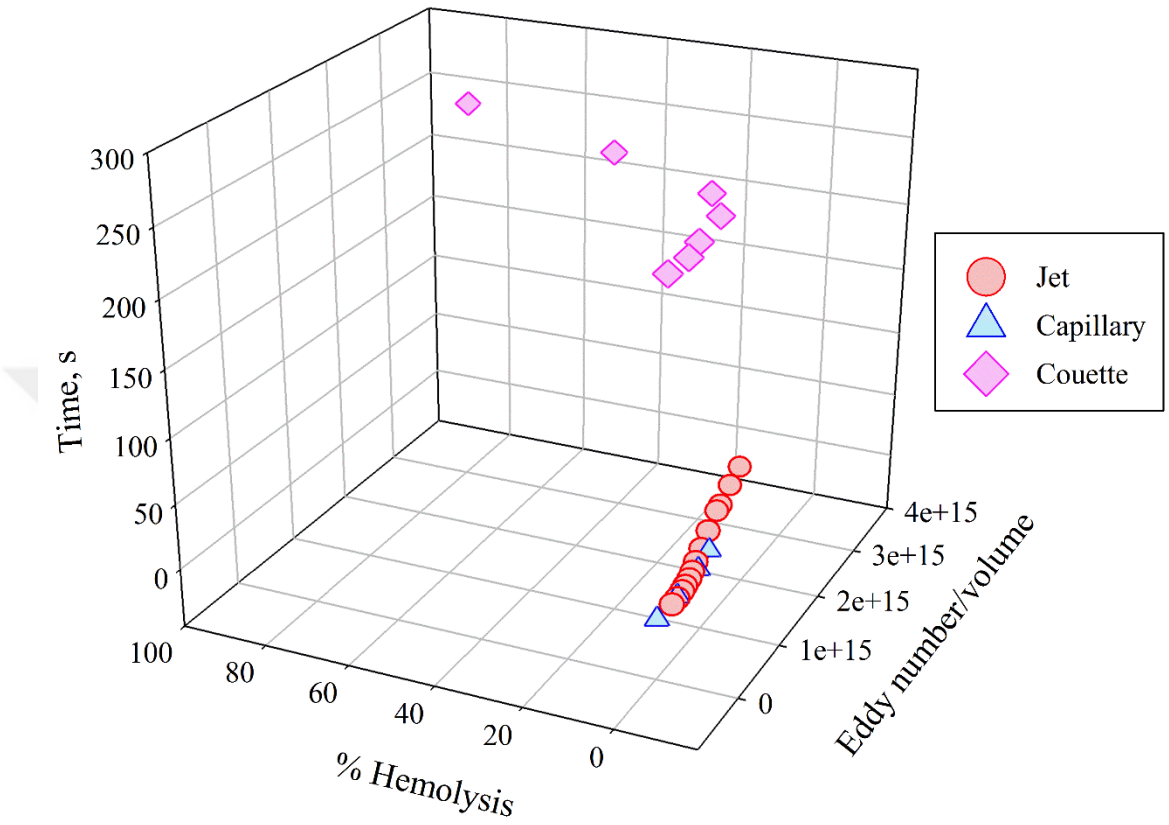

Figure 7.2. Eddy number per volume for the Couette viscometer, the capillary tube, and the jet.

As can be seen from Figure 7.1 and Figure 7.2, these three systems show huge differences especially in terms of exposure time that differ by orders of magnitude - the Couette viscometer has the longest exposure time of 4 minutes compared to much shorter times for the other 2 systems. Even if they look similar in figures, the capillary tube and the jet were also different in terms of exposure times of 1 s and 10^{-5} s respectively.

Empirical fits of different types of functions were performed for both eddy area and eddy number. Moreover, every different function was also tested for the whole range of hemolysis levels (presented in Sections 3, 4, and 6), for hemolysis levels of 10%, and

for hemolysis levels of 5% for each system. However, only results for hemolysis level of 5% is presented here for simplicity. Results of fitting eddy number to every different function is also not shown here for simplicity and also eddy number results are not shown, because they are mostly similar to eddy area results. The forms of several trial functions tested are summarized below.

7.3.1 Regression of Power Law Functions

Regression analysis was started by testing a power law type model for the three systems. The function is of the form

$$HI = aEA^{b}t^{c} \qquad \textbf{7.1}$$

where HI is hemolysis index (%), EA is cumulative eddy surface area up to 10 μm KLS, t is exposure time, a, b, and c are coefficients to be determined empirically. The same function was also tested for eddy number per volume. The function [Eq. 7.1] was fitted for 3 systems together as well as fitted separately for each system. Results of fitting 3 system together for the power law type function are presented in Figure 7.3. Coefficients are presented in Table 7.1. As can be seen from Figure 7.3, power law type function do not yield a satisfactory fit for all three systems. The results presenting the fit for 3 systems separately are presented in the appendix (Figure 0.3).

After fitting the 3 systems together and fitting them separetly, we also fit every 2 systems together to test the power law type function of Equation 7.1. The coeffcients for fitting every two system are presented in Table 7.1. Moreover, the figures for fitting every 2 systems together were also plotted, similarly Figure 7.3, and presented in the appendix (Figure 0.4, Figure 0.5, and Figure 0.6).

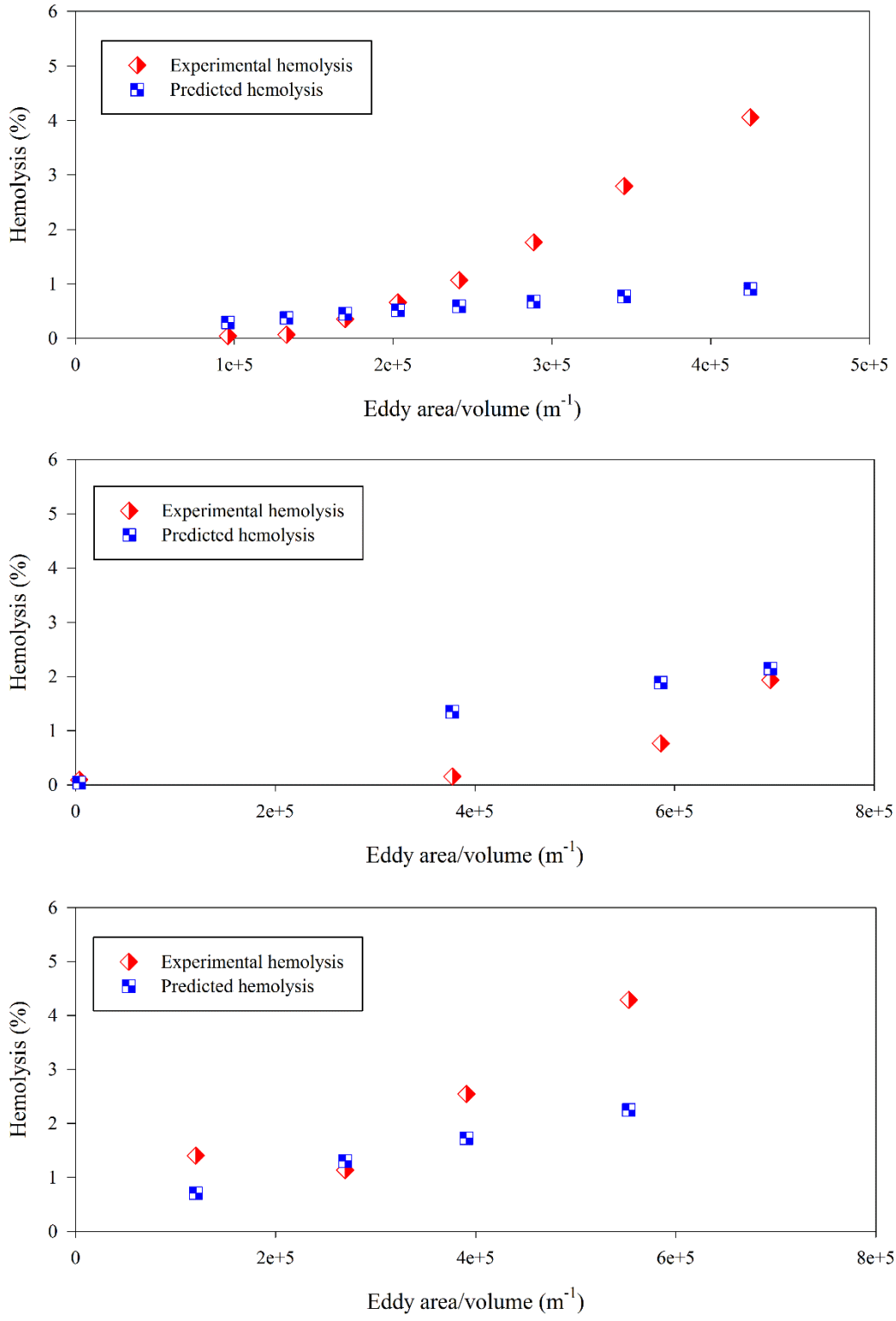

Figure 7.3. Comparison of hemolysis from experiment and from our model [Eq. (7.1)] by fitting the 3 systems together. Top: jet, middle: capillary tube, bottom: Couette viscometer.

We also tested the power law type model with binning the eddy area with different KLS sizes in the form of Equation 7.2. The reason of binning the eddy areas is that the distribution of eddy sizes in the three systems (i.e., jet, Couette viscometer, and capillary tube) is very different, especially in the jet experiment (distribution plots can be seen on Sections 3,4, and 6). Therefore, the contribution of an eddy area for a specific KLS size can be different in each of these systems. The fit equation is

$$HI = \mathrm{a}t^{b} EA^{c}_{KLS(0-3)} + EA^{d}_{KLS(4-6)} + EA^{e}_{KLS(7-9)} \qquad \textbf{7.2}$$

where a, b, c, d and e are experimental coefficients, $EA_{KLS(0-3)}$ is cumulative eddy surface area for KLS size of 0 to 3 μm. Similarly, the other two terms are eddy areas for KLS sizes from 4 to 6 μm and from 7 to 9 μm. Eddy number was also tested with the same function. The three systems were fitted together by using function [Eq. 7.2] and plotted with experimental hemolysis in Figure 7.4. Coefficients are presented in Table 7.1. As can be seen from Figure 7.4, power law type function with binning the eddy area do not yield satisfactory fit for all three systems.

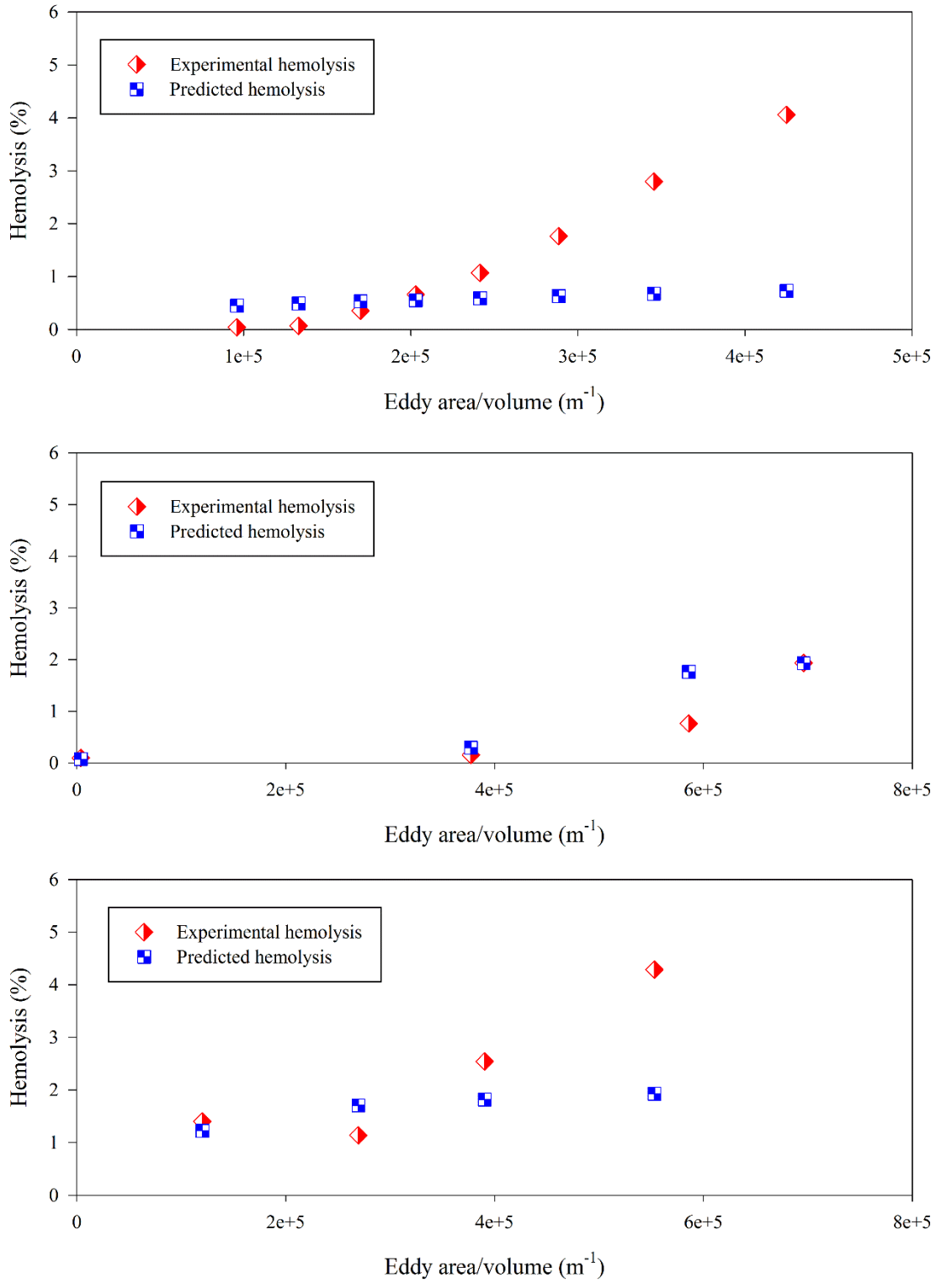

Figure 7.4. Comparison of experimental hemolysis and hemolysis from our model [Eq. (7.2)] by fitting the jet, capillary tube, and Couette viscometer together. Top: jet, middle: capillary tube, bottom: Couette viscometer.

Table 7.1. Power law type functions and model constants tested for empirical fitting of three systems together, every two system together and each system separate. Please note that if the tested function does not have all the coefficients (a, b, c, d, e), the cell on the table left blank.

Coefficients / Systems		a	b	c	d	e	R^2	
3 systems together (Eq.7.1)		$7.88*10^{-5}$	0.785	0.042	-	-	Jet	0.08
							Capillary	0.24
							Couette	0.13
Two systems together (Eq. 7.1)	Jet and Couette	$4.17*10^{-10}$	1.79	0.06	-	-	Jet	0.88
							Couette	0.19
	Capillary and Couette	$3.94*10^{-4}$	0.57	0.44	-	-	Capillary	0.39
							Couette	0.12
	Jet and Capillary	$6.74*10^{-6}$	0.92	-0.06	-	-	Jet	0.20
							Capillary	0.55
Each system separate (Eq. 7.1)	Jet	$8.54*10^{3}$	1.01	1.91	-	-	0.11	
	Capillary	$4.28*10^{-7}$	0.4	51.25	-	-	0.23	
	Couette	$6.87*10^{-4}$	0.605	0.072	-	-	0.62	
3 systems together (Eq. 7.2)		$3.11*10^{-2}$	0.048	0.001	0.36	-0.04	Jet	0.20
							Capillary	0.53
							Couette	0.05

7.3.2 Polynomial Regression

Another model we analyzed is a polynomial type function. We tried the following function with eddy area and eddy number of KLS up to 9 μm, and also with eddy areas and eddy numbers of different KLS bin sizes:

$$HI = \mathrm{a} + b*t + c*EA + d*EA^2 + e*t^2 + f*EA*t \qquad \textbf{7.3}$$

where EA is cumulative eddy surface area up to 9 μm KLS, a, b, c, d, e, and f are empirical coefficients. Equation 7.3 was used to fit the three systems together and plotted with experimental hemolysis in Figure 7.5. Coefficients are presented in Table 7.2. As can be seen from Figure 7.5, similar to the power law type function, a polynomial function does not give acceptable fit for all three systems.

Table 7.2. Polynomial function and model constants tested for empirical fitting**.**

Coefficients / **Systems**	**a**	**b**	**c**	**d**	**e**	**f**	**R^2**	
3 systems together (Eq. 7.3)	-0.66	$1.12*10^{-5}$	-0.14	$-1.15*10^{-11}$	$5.56*10^{-4}$	$2.17*10^{-8}$	Jet	0.58
							Capillary	0.30
							Couette	0.75

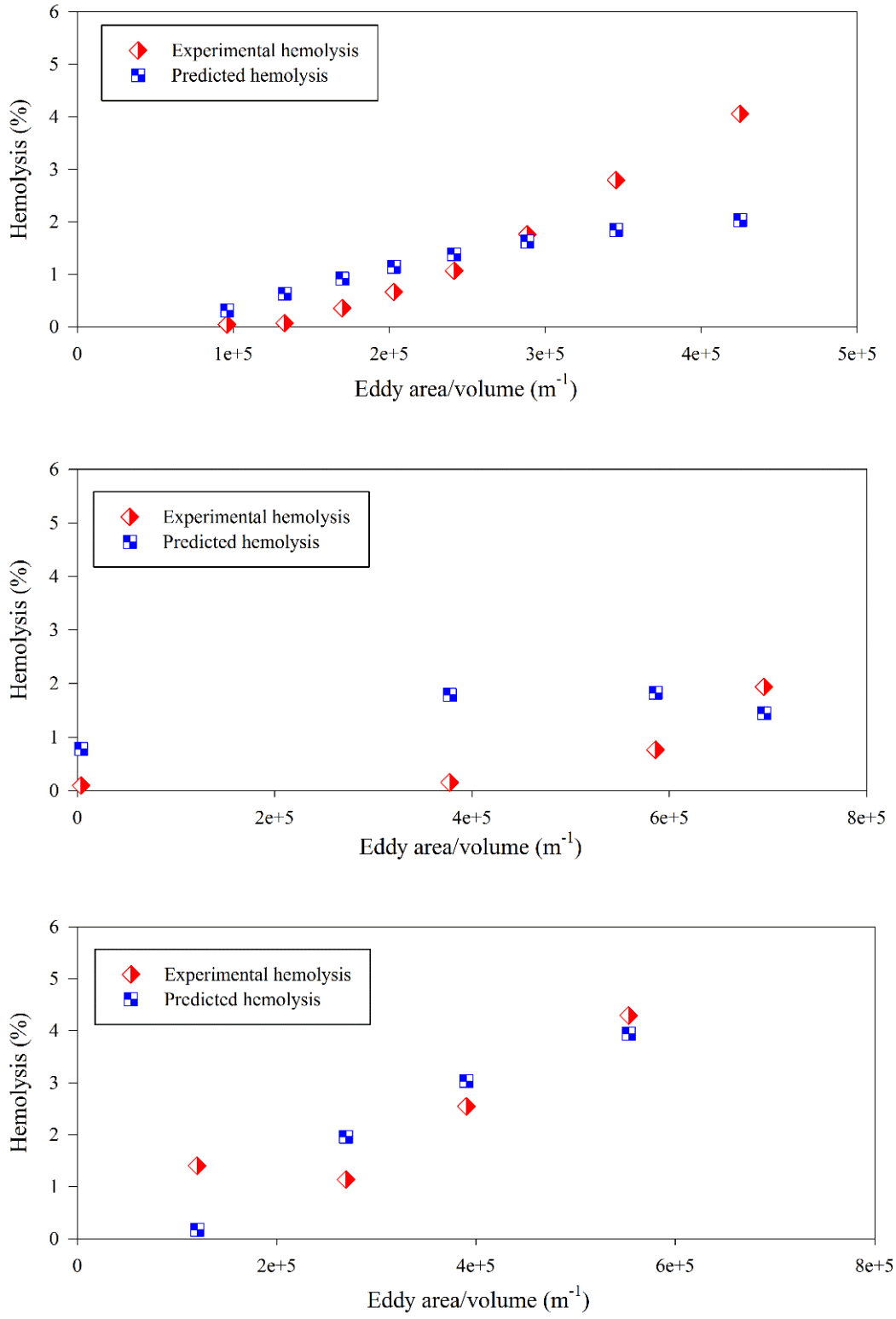

Figure 7.5. Comparison of experimental hemolysis and hemolysis from our model [Eq. (7.3)] by fitting the jet, capillary tube, and Couette viscometer together. Top: jet, middle: capillary tube, bottom: Couette viscometer.

7.3.3 Exponential Regression

After testing the power law and polynomial functions, we also tested an exponential type model, with eddy areas grouped in different bin sizes. We fit three systems together as well as fitting them separately. The function is as follows:

$$HI = \mathrm{a} * t + b * e^{EA_{KLS(0-3)}} + c * e^{EA_{KLS(4-6)}} + d * e^{EA_{KLS(7-9)}} \quad \textbf{7.4}$$

where a, b, c, and d are experimental coefficients, $EA_{KLS(0-3)}$ is cumulative eddy surface area for KLS size of 0 to 3 µm. Similarly, the other two terms are eddy areas for KLS sizes from 4 to 6 µm and from 7 to 9 µm. Results of fitting 3 system together for the exponential type function is presented in Figure 7.6. Moreover, the figures for fitting every system separately were also plotted and presented in the appendix (Figure 0.7). Coefficients of the fit are shown on in Table 7.3. As can be seen from Figure 7.6, exponential function is also not adequate for all three systems.

Table 7.3. Exponential function and model constants tested for empirical fitting of three systems together and each system separately.

Coefficients / **Systems**		**a**	**b**	**c**	**d**	**R^2**	
3 systems together (Eq.7.4)		$4.54*10^{-3}$	$4.89*10^{-1}$	$7.09*10^{-1}$	$4.12*10^{-2}$	Jet	0.05
						Capillary	0.10
						Couette	0.20
Each system separate (Eq.7.4)	Jet	$-1.17*10^{6}$	-16.6	32.2	-3.68	0.77	
	Capillary	1.37	-1.09	2.09	-2.54	0.802	
	Couette	-0.018	0.798	-11.7	16.6	0.797	

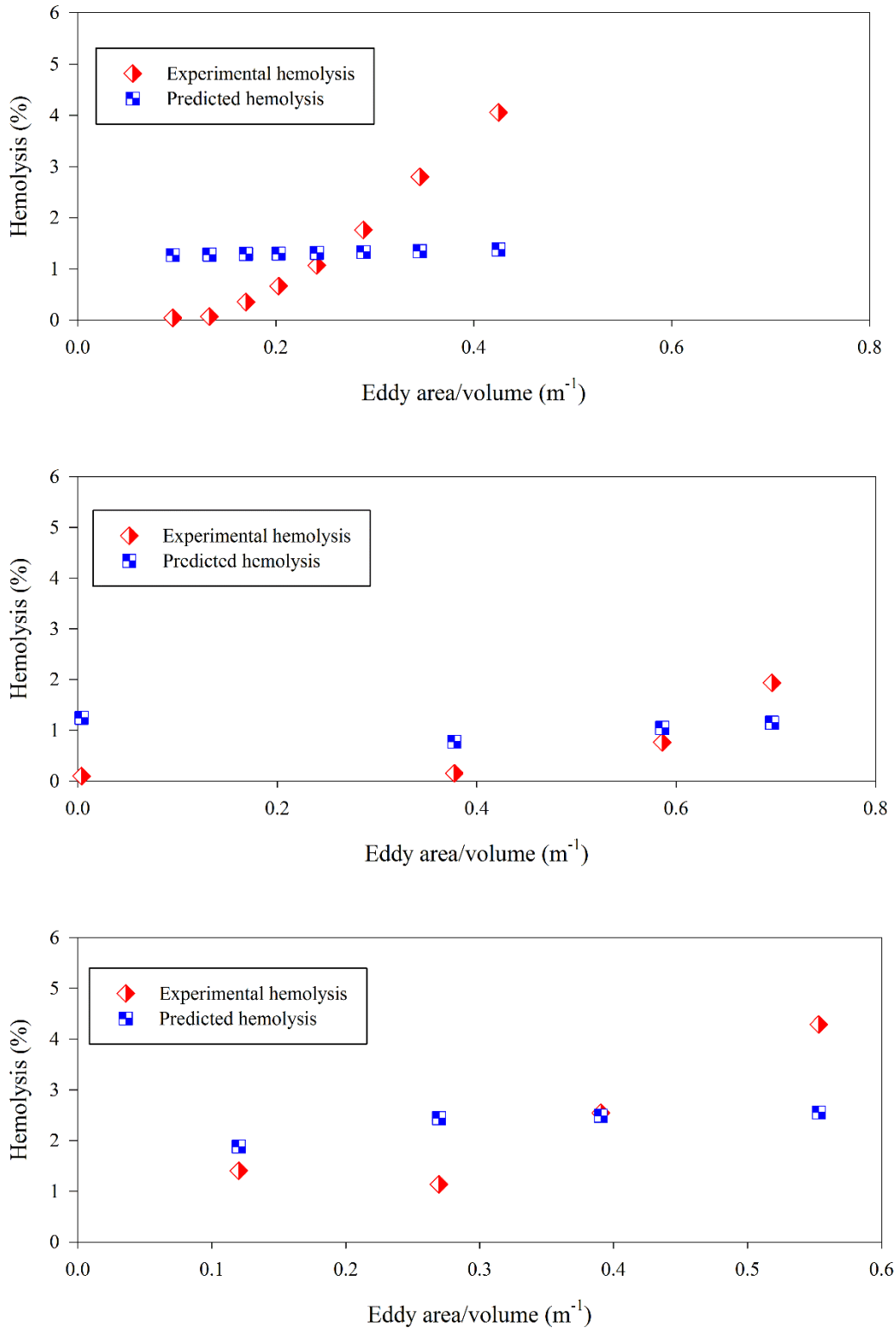

Figure 7.6. Comparison of experimental hemolysis and hemolysis from our model [Eq. (7.4)] by fitting the jet, capillary tube, and Couette viscometer together. Top: jet, middle: capillary tube, bottom: Couette viscometer.

7.3.4 Linear Regression

After tests for power law, polynomial, and exponential function types failed to yield satisfactory fits, we examined linear functions with eddy area and eddy number of different bin sizes. We tested the following equation form:

$$HI = \mathrm{a} + b*t + c*EA_{KLS(0–3)} + d*EA_{KLS(4–6)} + e*EA_{KLS(7–9)} \qquad \textbf{7.5}$$

where a, b, c, d, and e are experimental coefficients, $EA_{KLS(0-3)}$ is cumulative eddy surface area for KLS size of 0 to 3 μm. Similarly, the other two terms are eddy areas for KLS sizes from 4 to 6 μm and from 7 to 9 μm. Results of fitting 3 system together for the linear type function is presented in Figure 7.7. Coefficients of the fit are shown in Table 7.4. As can be seen from Figure 7.7, linear function gave much better agreement with the experimental data for all three systems when it does for other function types.

Another linear function we tried is very similar to Equation 7.5, only difference was to use the coefficient of exposure time as a power. This was tested to better observe contribution of exposure time since three systems have very different exposure times. Equation form:

$$HI = \mathrm{a} + t^{b} + c*EA_{KLS(0–3)} + d*EA_{KLS(4–6)} + e*EA_{KLS(7–9)} \qquad \textbf{7.6}$$

Changing the coefficient type of exposure time did not improve the fitting when compared to Equation 7.5. Results are plotted and presented in appendix (Figure 0.8). Coefficients were given in Table 7.4.

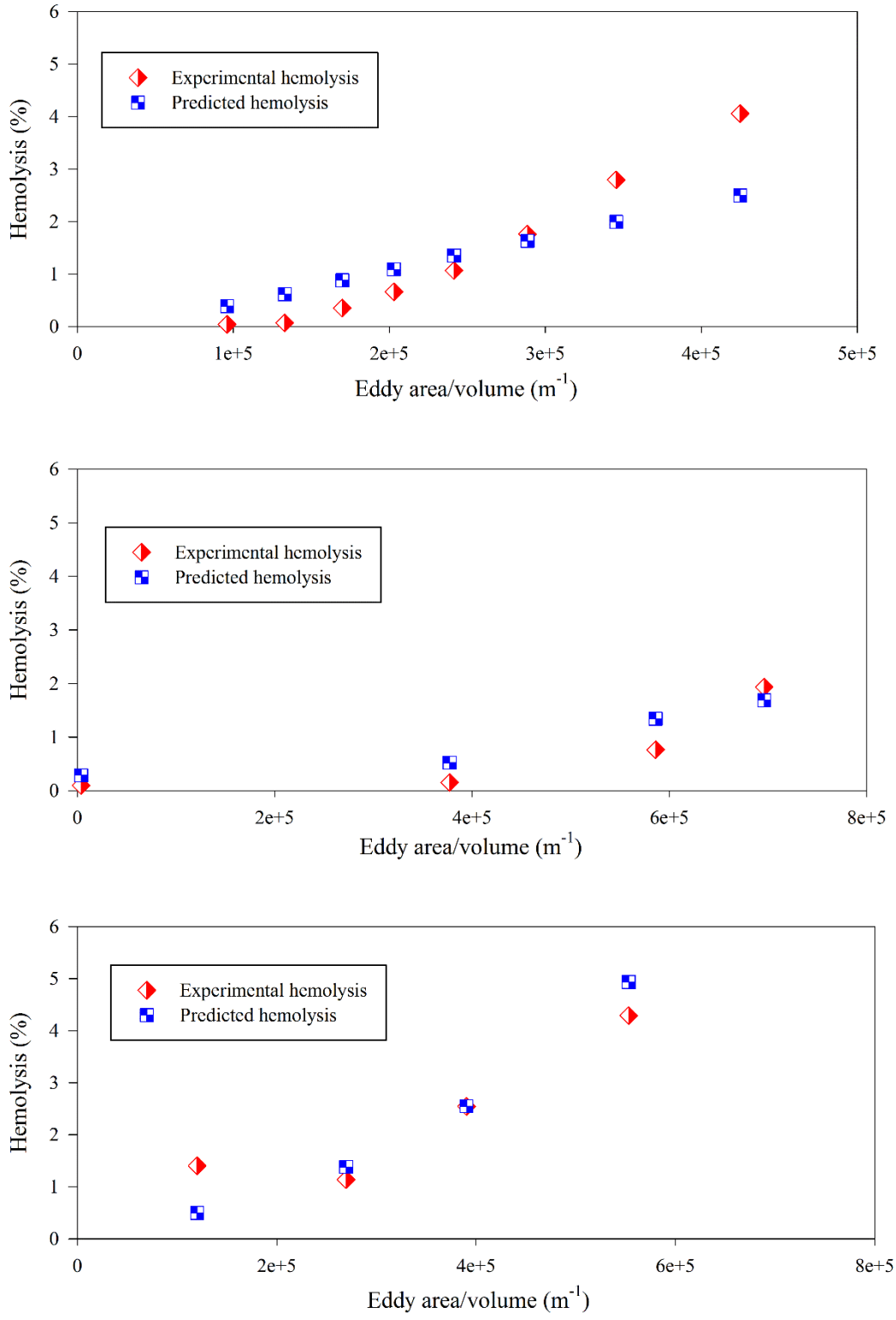

Figure 7.7. Comparison of experimental hemolysis and hemolysis from our model [Eq. (7.5)] by fitting the jet, capillary tube, and Couette viscometer together. Top: jet, middle: capillary tube, bottom: Couette viscometer.

The next function we tested was also linear, but it has different bin sizes for eddy area and eddy number. The equation form is as follows:

$$HI = \mathrm{a} + bt + c * EA_{KLS(0-4)} + d * EA_{KLS(5-9)} \qquad \textbf{7.7}$$

where a, b, and c are experimental coefficients, $EA_{KLS(0-4)}$ is cumulative eddy surface area for KLS size of 0 to 4 μm and $EA_{KLS(5-9)}$ cumulative eddy area for KLS sizes from 5 to 9 μm. Results of fitting 3 system together for the linear type function are presented in Figure 7.8. Coefficients of the fit are shown in Table 7.4. As can be seen from Figure 7.8, linear function with different bin size gave good agreement with the experimental data for all three systems.

Table 7.4. Linear functions and model constants tested for empirical fitting.

Coefficients / Systems	a	b	c	d	e	R^2	
3 systems together (Eq.7.5)	$1.62*10^{-7}$	$1.82*10^{-7}$	$3.08*10^{-5}$	$3.42*10^{-6}$	$1.72*10^{-6}$	Jet	0.67
						Capillary	0.58
						Couette	0.78
3 systems together (Eq.7.6)	-0.076	0.0198	$3.77*10^{-5}$	$3.20*10^{-6}$	$1.60*10^{-6}$	Jet	0.18
						Capillary	0.70
						Couette	0.23
3 systems together (Eq.7.7)	-0.25	$1.36*10^{-4}$	$2.18*10^{-5}$	$2.38*10^{-6}$	-	Jet	0.69
						Capillary	0.76
						Couette	0.66

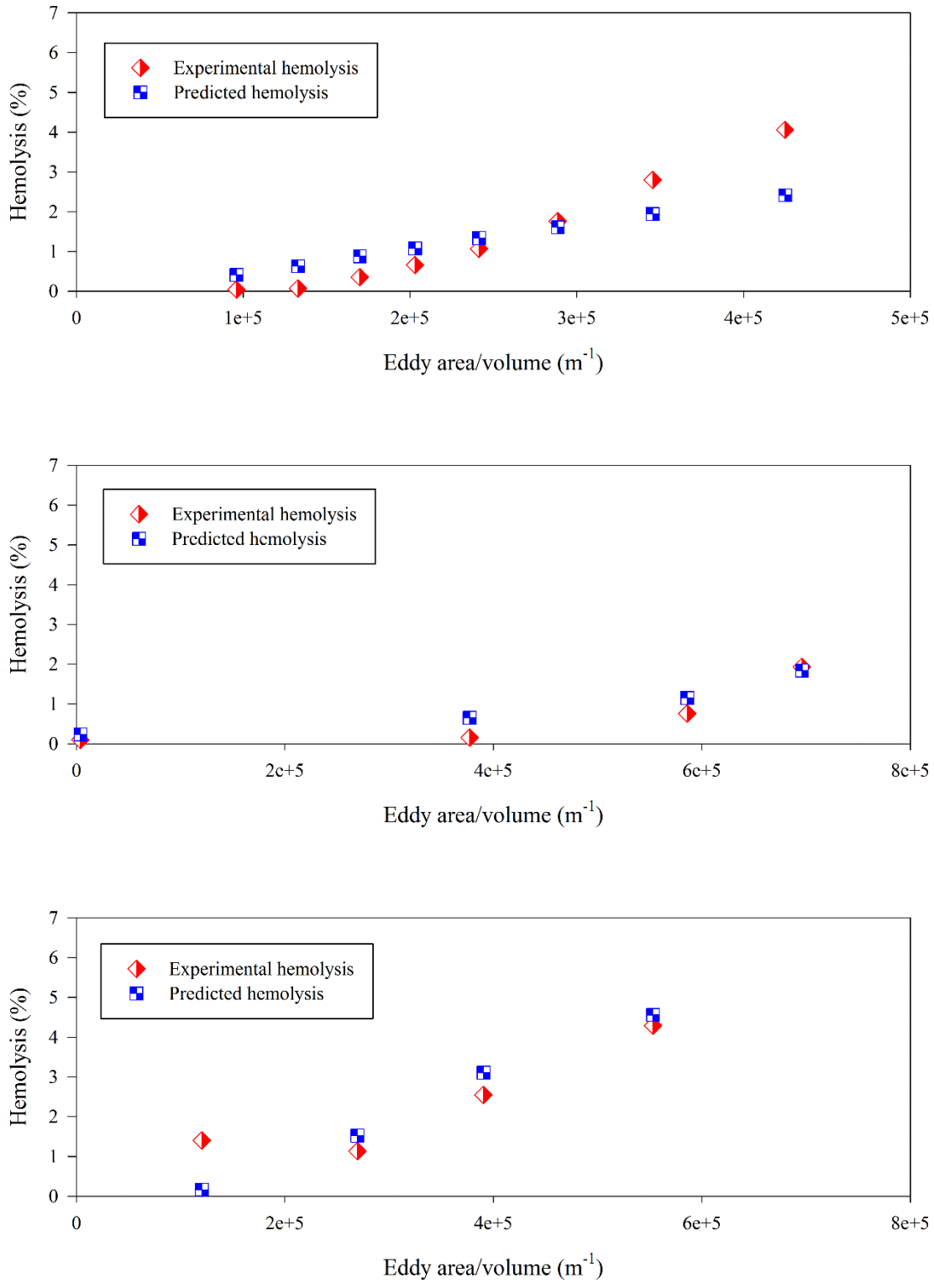

Figure 7.8. Comparison of experimental hemolysis and hemolysis from our model [Eq. (7.7)] by fitting the jet, capillary tube, and Couette viscometer together. Top: jet, middle: capillary tube, bottom: Couette viscometer.

7.3.5 Proposed Hemolysis Model

Several other functions were tried with different bin sizes, different number of coefficients, and other functions. We do not present all of the different forms examined here. The best function found is a linear form, as follows:

$$HI = at + b * EA_{KLS(0-4)} + c * EA_{KLS(5-7)} + d * EA_{KLS(8-10)} \qquad \textbf{7.8}$$

where a, b, c, and d are experimental coefficients, $EA_{KLS(0-4)}$ is cumulative eddy surface area for KLS size of 0 to 4 μm and similarly, the other two terms are eddy areas for KLS sizes from 5 to 7 μm and from 8 to 10 μm. Equation 7.8 was used to fit calculate hemolysis for the three systems together and plotted in Figure 7.9. The coefficients for Equation 7.8 are presented in Table 7.5.

Table 7.5. Model constants for Equation 7.8 for fitting 3 systems together and separate.

Coefficients / **Systems**		**a (s^{-1})**	**b (m^{-2})**	**c (m^{-2})**	**d (m^{-2})**	**R^2**	
3 systems together (Eq.7.8)		$5.57*10^{-4}$	$2.45*10^{-5}$	$2.67*10^{-6}$	$1.14*10^{-6}$	Jet	0.61
						Capillary	0.82
						Couette	0.68
Each system separate (Eq.7.8)	Jet	1.028	$4.10*10^{-8}$	$2.19*10^{-5}$	$2.50*10^{-8}$	0.78	
	Capillary	$2.41*10^{-7}$	$5.43*10^{-5}$	$2.14*10^{-6}$	$1.25*10^{-11}$	0.98	
	Couette	$1.45*10^{-7}$	$1.13*10^{-5}$	$1.11*10^{-5}$	$8.51*10^{-7}$	0.83	

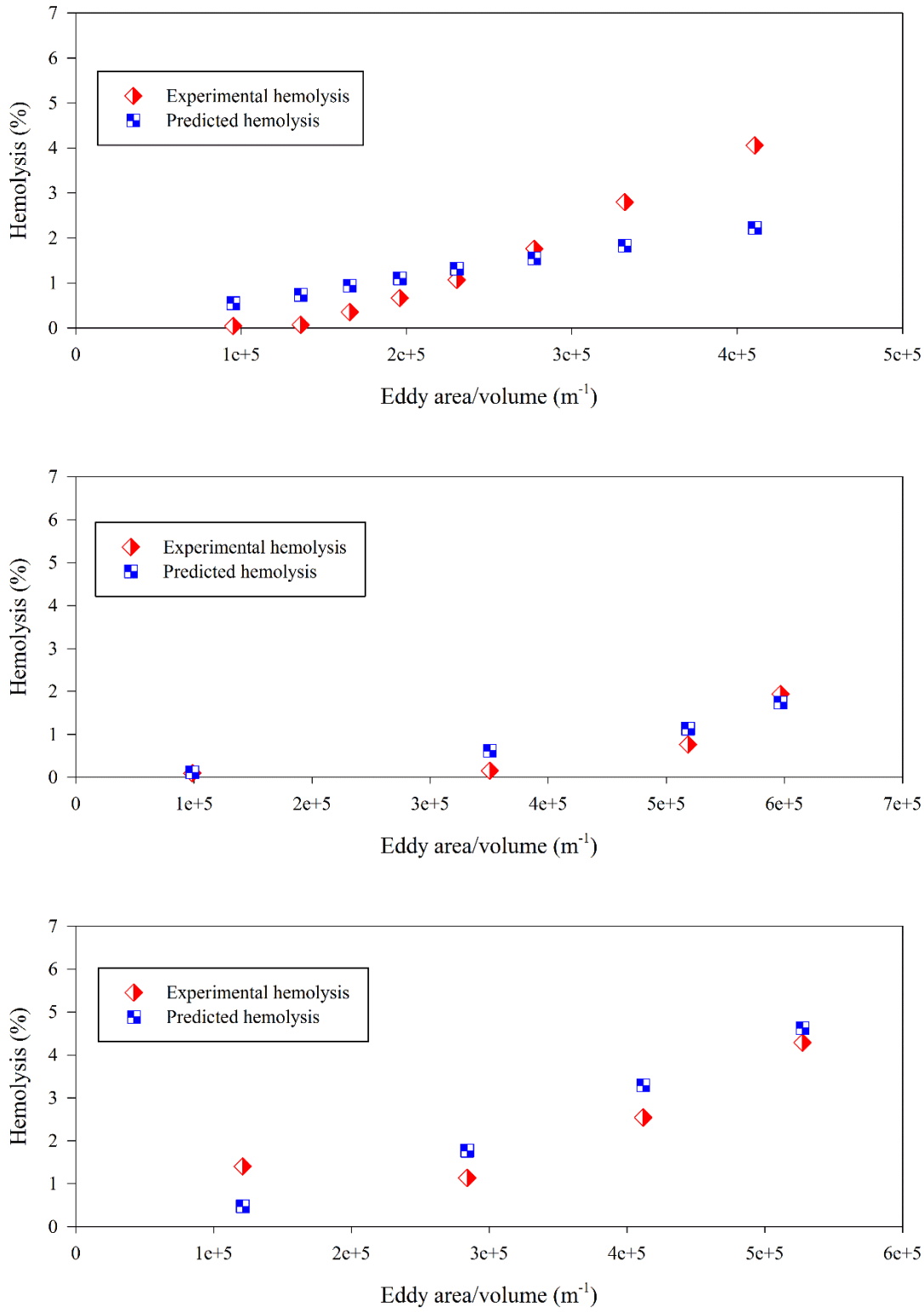

Figure 7.9. Comparison of experimental hemolysis and hemolysis from our model [Equation (7.8)] by fitting jet, capillary tube, and Couette viscometer together. Top: jet, middle: capillary tube, bottom: Couette viscometer.

As can be seen from Figure 7.9 and R^2 values on Table 7.5, the hemolysis model gives reasonably good agreement with experimental hemolysis values even though these systems have very different conditions. The worst agreement was obtained with the jet experiment because it has much shorter exposure times (10^{-5} s) and much smaller KLS sizes as compared to the Couette viscometer experiment that has 4 minutes exposure time.

We also fit the three systems separately by using Equation 7.8 and obtained coefficients for each experiment that can be seen on Table 7.5. By using the coefficients on Table 7.5 on Equation 7.8, hemolysis predictions were performed for three systems and shown in Figure 7.10.

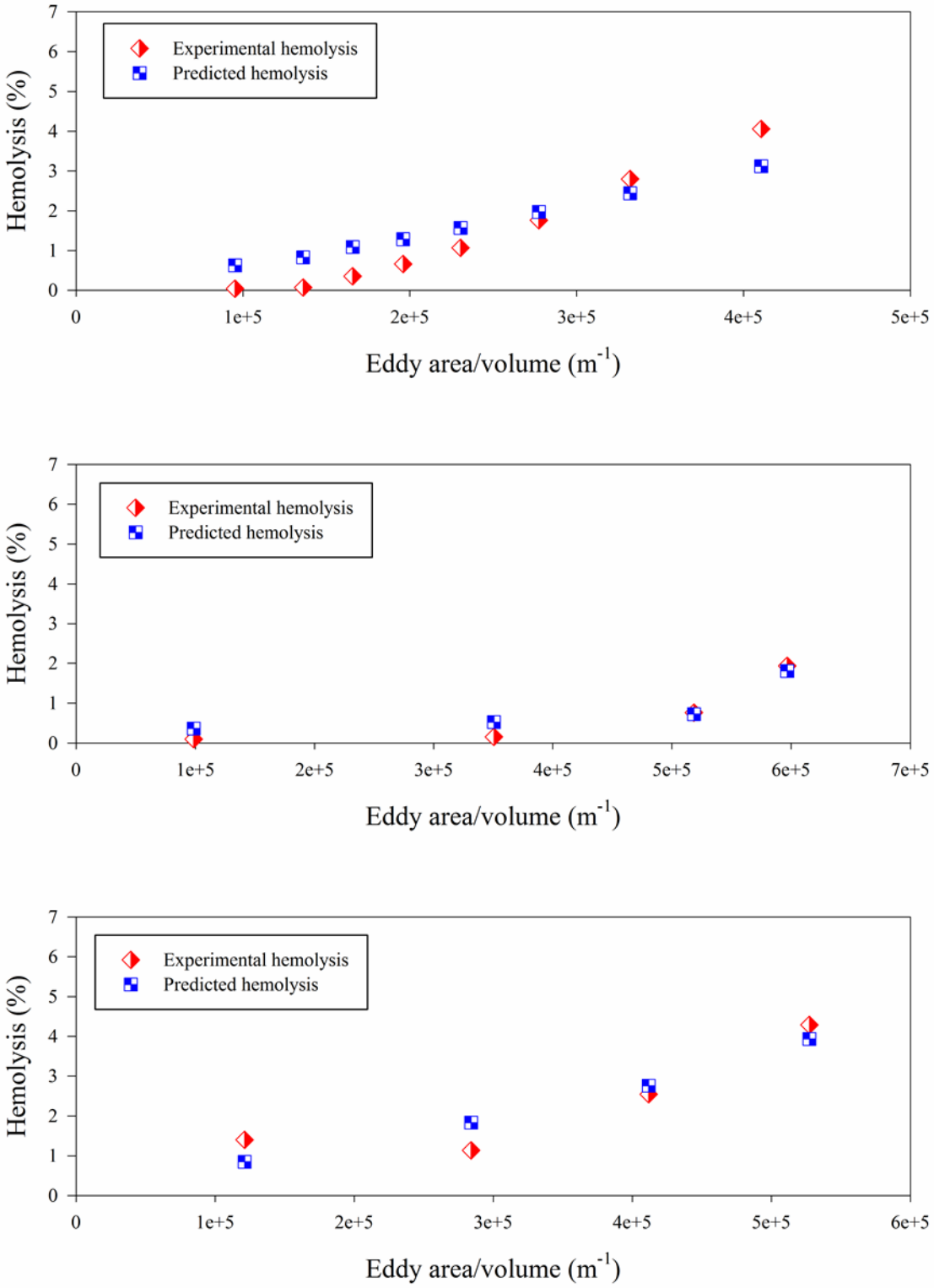

Figure 7.10. Comparison of experimental hemolysis and hemolysis from our model [Equation (7.8)] by fitting jet, capillary tube, and Couette viscometer separately. Top: jet, middle: capillary tube, bottom: Couette viscometer.

The linear model can fit the three system separately as well as fit them together. Non-linearity appearing in the plots results from the shift in the distribution to smaller eddy sizes with increasing turbulence.

7.4 Summary

The results showed that power law, exponential, and polynomial type functions did not give good fits for the Couette viscometer [60], the capillary tube [9], and the jet [57] that have distinctly different flow fields and exposure times. The linear model (Equation 32) with different bin size of eddy area gave the best fit.

8 Conclusions and Future Work

The lack of a fundamental physical description of the hemolysis mechanisms in a turbulent flow field complicates a deterministic approach to hemolysis prediction. However, if the shear and/or extensional deformations of cells occur at the boundaries or within small eddies, then the probability of hemolysis might be expected to be proportional to properties of eddies in a device and the surface area of these eddies.

In this work, the relation between turbulence characteristics and hemolysis is examined for a Couette viscometer, a capillary tube, and a jet. Calculation of the Kolmogorov length scales for the Couette viscometer may be applicable to computationally investigate hemocompatibility of blood-wetted devices, such as in rotary VADs. Results of Couette, capillary, and jet experiments showed that hemolysis is related directly with the total surface area of eddies with diameters of up to about 10 μm. This is comparable to the size of RBCs. This value has been calculated given the uncertainties incorporated in our analysis, and further experiments and more detailed simulations are needed for different flow configurations and other experimental setups to verify or modify the accuracy of this value. Based on the current findings, we cannot say that there is a cause and effect relationship. However, many investigators have looked at energy dissipation as a basis for hemolysis. The approach presented here aims to assess the effects of the intensity of energy dissipation on hemolysis. A relation was not evident for larger eddies. At present, additional investigation of eddy analysis to yield hemolysis predictions in other device and systems is required to confirm widespread applicably to blood-contacting devices. At this time, the KLS-based approach might offer insight into the hemolytic changes due to proposed changes in design or operation of a device.

A new empirical model was also proposed to predict hemolysis in turbulent flow that takes into account the complexity of turbulence by giving varying weight to eddies of different sizes. The model was applied to the Couette viscometer, [60] the capillary tube, [9] and the jet. [57] Reasonable results have been obtained for flow fields and exposure times of the three distinctly different experiments.

The eddy analysis and the hemolysis model presented here can be applied in conjunction with various turbulence simulations, possibly across a wide range of conditions and devices. The prediction of the Kolmogorov eddy size distribution might then lead to an evaluation of whether a particular design of a medical device is more or less susceptible to hemolysis, and what changes need to be done in the design to increase the size of the Kolmogorov scales. If eddy analysis is to be investigated for broader application, additional measurements of hemolysis need to be made in turbulent flows as a function of exposure time for various KLS values, ideally with a nearly uniform KLS value throughout the flow field.

Eddy analysis as presented here does not explicitly take into account exposure time. We note two points in that regard. Results for the very different exposure times of the three systems examined suggest a possible a relationship for hemolysis from exposure time-eddy surface area plots. Moreover, the power law relationships teach us there is a much stronger dependence on stress than exposure time. An order of magnitude increase in exposure time ($10^{0.75}$) results in a factor of 5.6 compared to a factor of 100 (10^{2}) for a comparable shear stress increase. A focus on energy dissipation and associated stresses may be justified in a well-mixed turbulent system.

Moreover, in this work, a threshold analysis for Reynolds stress and viscous stresses was conducted for a Couette viscometer and a capillary tube by assuming that systems were well mixed and cells on average spent the same amount of time in any location inside the flow field. Results of Couette and capillary experiments showed that there is not a common threshold value for Reynolds and viscous stress where hemolysis happens.

Therefore, it is seen that neither Reynolds nor viscous stress is a good predictor when determining hemolysis. At present, additional investigation of threshold analysis of Reynolds and viscous stresses in other devices and systems is required to confirm widespread applicably of this finding. At this time, this threshold analysis may offer insight into the hemolysis calculations by using Reynolds and viscous stresses.

When applying a power law model that takes into account stress and exposure time of the RBCs, use of the Reynolds stress rather than the total stresses or the viscous stresses in the power law formula is found to provide better agreement between model and measurements at least in both systems modeled. However, it appears the coefficients of the power law formulation must be empirically derived for each device. This is a disadvantage of this class of hemolysis models.

References

1. Centers for disease control and prevention. *Heart disease facts and statistics*. 2015; Available from: http://www.cdc.gov/heartdisease/statistics.htm.
2. Go, A.S., et al., *Heart disease and stroke statistics-2014 update: A report from the American Heart Association*. 2014.
3. Fraser, K.H., et al., *The use of computational fluid dynamics in the development of ventricular assist devices.* Medical Engineering & Physics, 2011. **33**(3): p. 263-280.
4. Givertz, M.M., *Ventricular assist devices important information for patients and families.* Circulation 2011. **124**: p. e305-311.
5. University of Michigan health system. *Ciculatory and ventricular assist devices (VAD)*. 2015; Available from: http://www.med.umich.edu/cardiac-surgery/patient/adult/ccs/vad.shtml.
6. National Institutes of Health. *Ventricular assist device*. 2012; Available from: http://www.nhlbi.nih.gov/health/health-topics/topics/vad/.
7. Antiga, L. and D.A. Steinman, *Rethinking turbulence in blood.* Biorheology, 2009. **46**(2): p. 77-81.
8. Hund, S.J., J.F. Antaki, and M. Massoudi, *On the representation of turbulent stresses for computing blood damage.* Int J Eng Sci, 2010. **48**(11): p. 1325-1331.
9. Kameneva, M.V., et al., *Effects of turbulent stresses upon mechanical hemolysis: experimental and computational analysis.* ASAIO J, 2004. **50**(5): p. 418-423.
10. Aziz, A., et al., *The cumulative and sublethal effetcs of turbulence on erythrocytes in a stirred-tank model.* Annals of Biomedical Engineering, 2007. **35**(12): p. 2108-2120.
11. Bludszuweit, C., *Three-dimensional numerical prediction of stress loading of blood particles in a centrifugal pump.* Artificial Organs, 1995. **19**(7): p. 590-596.
12. Sigma-Aldrich. *Physical properties of blood and plasma*. 2015 [cited 2015; Available from: http://www.sigmaaldrich.com/life-science/metabolomics/enzyme-explorer/learning-center/plasma-blood-protein/blood-basics.html.
13. Penn Medicine. *Formed elements of blood*. 2002 [cited 2015; Available from: http://www.pennmedicine.org/encyclopedia/em_DisplayImage.aspx?gcid=19192&ptid=2&rgcid=003644&rptid=1.
14. Arora, D., M. Behr, and M. Pasquali, *Hemolysis computations in centrifugal clood pump using a tensor-based measure.* Artificial Organs, 2006. **30**(7): p. 539-547.
15. Behbahani, M., et al., *A review of computational fluid dynamics analysis of blood pumps.* Eur J Appl Math, 2009. **20**: p. 363-397.
16. Ge, L., et al., *Characterization of hemodynamic forces induced by mechanical heart valves: Reynolds vs. viscous stresses.* Annals of Biomedical Engineering, 2008. **36**(2): p. 276-297.

17. Grigioni, M., et al., *Prosthetic heart valves' mechanical loading of red blood cells in patients with hereditary membrane defects.* Journal of Biomechanics, 2005. **38**(8): p. 1557-1565.
18. Quinlan, N.J. and P.N. Dooley, *Models of flow-induced loading on blood cells in laminar and turbulent flow, with application to cardiovascular device flow.* Annals of Biomedical Engineering, 2007. **35**(8): p. 1347-1356.
19. Park, S.J., S.S. Kushwaha, and C.G.A. McGregor, *State-of-the-art implantable cardiac assist device therapy for heart failure: Bridge to transplant and destination therapy.* Clinical Pharmacology & Therapeutics, 2012. **91**(1): p. 94-100.
20. Blackshear, P.L., F.D. Dorman, and J.H. Steinbach, *Some mechanical effects that influence hemolysis.* T Am Soc Art Int Org, 1965. **11**(1): p. 112-117.
21. Giersiepen, M., et al., *Estimation of shear stress-related blood damage in heart valve prostheses-in vitro comparison of 25 aortic valves.* Int J Artif Organs, 1990. **13**(5): p. 300-306.
22. Heuser, G. and R. Opitz, *A Couette viscometer for short time shearing of blood.* Biorheology, 1980. **17**(1-2): p. 17-24.
23. Fraser, K.H., et al., *A quantitative comparison of mechanical blood damage parameters in Rotary Ventricular Assist Devices: shear stress, exposure time, and hemolysis index.* Journal of Biomechanical Engineering, 2012. **134**(8): p. 081002.
24. Zhang, T., et al., *Study of flow-induced hemolysis using novel Couette-type blood shearing devices.* Artificial Organs, 2011. **35**(12): p. 1180-1186.
25. Arvand, A., M. Hormes, and H. Reul, *A validated computational fluid dynamics model to estimate hemolysis in a rotary blood pump.* Artificial Organs, 2005. **29**(7): p. 531-540.
26. Bludszuweit, C., *Model for a general mechanical blood damage predication.* Artificial Organs, 1995. **19**(7): p. 583-589.
27. Chan, W.K., et al., *Numerical investigation of the effect of blade geometry on blood trauma in a centrifugal blood pump.* Artificial Organs, 2002. **26**(9): p. 785-793.
28. Song, X., et al., *Computational fluid dynamics prediction of blood damage in a centrifugal pump.* Artificial Organs, 2003. **27**(10): p. 938-941.
29. Arora, D., M. Behr, and M. Pasquali, *A tensor-based measure for estimating blood damage.* Artificial Organs, 2004. **28**(11): p. 1002-1015.
30. Vitale, F., et al., *A multiscale, biophysical model of flow-induced red blood cell damage.* American Institute of Chemical Engineers Journal, 2014. **60**(4): p. 1509-1516.
31. Chen, Y. and M.K. Sharp, *A strain-based flow-induced hemolysis prediction model calibrated by in vitro erythrocyte deformation measurements.* Artificial Organs, 2011. **35**(2): p. 145-156.
32. Goubergrits, L. and K. Affeld, *Numerical estimation of blood damage in artificial organs.* Artificial Organs, 2004. **28**(5): p. 499-507.
33. Grigioni, M., et al., *A novel formulation for blood trauma prediction by a modified power-law mathematical model.* Biomechanics and Modeling in Mechanobiology, 2005. **4**(4): p. 249-260.

34. Gu, L. and W.A. Smith, *Evaluation of computational models for hemolysis estimation.* ASAIO J, 2005. **51**(3): p. 202-207.
35. Kataoka, H., et al., *Influence of radial clearance and rotor motion to hemolysis in a journal bearing of a centrifugal blood pump.* Artificial Organs, 2006. **30**(11): p. 841-854.
36. Kim, N.J., et al., *Parametric study of blade tip clearance, flow rate, and impeller speed on blood damage in rotary blood pump.* Artificial Organs, 2009. **33**(6): p. 468-474.
37. Paul, R., et al., *Shear stress related blood damage in laminar couette flow.* Artificial Organs, 2003. **27**(6): p. 517-529.
38. Arwatz, G. and A.J. Smits, *A viscoelastic model of shear-induced hemolysis in laminar flow.* Biorheology, 2013. **50**: p. 45-55.
39. Grigioni, M., et al., *The power-law mathematical model for blood damage prediction: analytical developments and physical inconsistencies.* Artificial Organs, 2004. **28**(5): p. 467-475.
40. Taskin, M.E., et al., *Evaluation of Eulerian and Lagrangian models for hemolysis estimation.* American Society for Artificial Internal Organs 2012. **58**(4): p. 363-372.
41. Pope, S.B., *Turbulent flows*, ed. C.U. Press. 2000, New York, USA.
42. Liu, J.S., P.C. Lu, and S.H. Chu, *Turbulence characteristics downstream of bileaflet aortic valve protheses.* J Biomech Eng, 1999. **122**(2): p. 118-124.
43. Li, C.P., C.W. Lo, and P.C. Lu, *Estimation of viscous dissipative stresses induced by a mechanical heart valve using PIV data.* Annals of Biomedical Engineering, 2010. **38**(3): p. 903-916.
44. Quinlan, N.J., *Mechanical loading of blood cells in turbulent flow*. Computational Biomechanics for Medicine. 2014, New York: Springer New York.
45. Yen, J.H., et al., *The effect of turbulent viscous shear stress on red blood cell hemolysis.* J Artif Organs, 2014.
46. Lee, H., E. Tatsumi, and Y. Taenaka, *Experimental study on the Reynolds and viscous shear stress of bileaflet mechanical heart valves in a pneumatic ventricular assist device.* ASAIO J, 2009. **55**(4): p. 348-354.
47. Jones, S.A., *A relationship between reynolds stresses and viscous dissipation: implications to red cell damage.* Annals of Biomedical Engineering, 1995. **23**(1): p. 21-28.
48. Sallam, A.M. and N.H.C. Hwang, *Human red blood cell hemolysis in a turbulent shear flow: contribution of Reynolds shear stresses.* Biorheology, 1984. **21**(6): p. 783-797.
49. Sallam, A.M., *An investigation of the effect of Reynolds shear stress on red blood cell hemolysis*. 1982, University of Houston.
50. Sallam, A.M. and N.H.C. Hwang, *Influence of red blood cell concentrations on the measurement of turbulence using hot-film anemometer.* Journal of Biomechanical Engineering, 1983. **105**: p. 406-410.
51. Ellis, J.T., T.M. Wick, and A.P. Yoganathan, *Prosthesis-induced hemolysis: mechanisms and quantification of shear stress.* J Heart Valve Dis, 1998. **7**(4): p. 376-386.

52. Dooley, P.N. and N.J. Quinlan, *Effect of eddy length scale on mechanical loading of blood cells in turbulent flow.* Annals of Biomedical Engineering, 2009. **37**(12): p. 2449-2458.
53. Davidson, P.A., *Turbulence: An introduction for scientists and engineers*. 2004, New York: Oxford University Press.
54. Hinze, J.O., *Turbulence: An introduction to its mechanism and theory* 1st Edition ed. 1969: McGraw-Hill.
55. Richardson, L.F., *Weather prediction by numerical process*. 1922, Cambridge: Cambridge University Press.
56. Pinotti, M. and E.M. de Faria, *Critical flow regions in tissue artificial heart valve assessed by laser doppler anemometer in continuous flow*. J Braz Soc Mech Sci Eng, 2006. **XXVIII**(3): p. 259-263.
57. Forstrom, R.J., *A new measure of erythrocyte membrane strength-the jet fragility test*. 1969, University of Minnesota.
58. Lu, P.C., H.C. Lai, and J.S. Liu, *A reevaluation and discussion on the threshold limit for hemolysis in a turbulent shear flow.* Journal of Biomechanics, 2001. **34**(10): p. 1361-1364.
59. Goubergrits, L., *Numerical modeling of blood damage: current status, challenges and future prospects.* Expert Review of Medical Devices, 2006. **3**(5): p. 527-531.
60. Sutera, S.P. and M.H. Mehrjardi, *Deformation and fragmentation of human red blood cells in turbulent shear flow.* Biophys J, 1975. **15**(1): p. 1-10.
61. Ozturk, M., E.A. O'Rear, and D.V. Papavassiliou, *Hemolysis related to turbulent eddy size distributions using comparisons of experiments to computations.* Artificial Organs, 2015. **39**(12): p. E227-E239.
62. Moin, P. and J. Kim, *Tackling turbulence with supercomputers.* Scientific American 1996. **276**(1): p. 62-68.
63. Tennekes, H. and J.L. Lumley, *A first course in turbulence*. 1972, U.S.: MIT Press.
64. Burgreen, G.W., et al., *Computational fluid dynamics as a development tool for rotary blood pumps.* Artificial Organs, 2001. **25**(5): p. 336-340.
65. Izraelev, V., et al., *A passively suspended Tesla pump left ventricular assist device.* American Society for Artificial Internal Organs, 2009. **55**(6): p. 556-561.
66. Morsi, Y.S., et al., *Numerical analysis of the flow characteristics of rotary blood pump.* Journal of Artificial Organs, 2001. **4**(1): p. 54-60.
67. Nguyen, V.T., et al., *Experimentally validated hemodynamics simulations of mechanical heart valves in three dimensions.* Cardiovascular Engineering and Technology, 2012. **3**(1): p. 88-100.
68. Wu, J., et al., *Computational fluid dynamics analysis of blade tip clearances on hemodynamic performance and blood damage in a centrifugal ventricular assist device.* Artificial Organs, 2010. **34**(5): p. 402-411.
69. Zhang, Y., et al., *Design optimization of an axial blood pump with computational fluid dynamics.* ASAIO J 2008. **54**(2): p. 150-155.
70. Apel, J., F. Neudel, and H. Reul, *Computational fluid dynamics and experimental validation of a microaxial blood pump.* ASAIO J, 2001. **47**(5): p. 552-558.

71. Chua, L.P., et al., *Computational fluid dynamics of gap flow in a biocentrifugal blood pump.* Artificial Organs, 2005. **29**(8): p. 620-628.
72. Mitoh, A., et al., *Computational fluid dynamics analysis of an intra-cardiac axial flow pump.* Artificial Organs, 2003. **27**(1): p. 34-40.
73. Schenkel, A., M.O. Deville, and M.L. Sawley, *Flow simulation and hemolysis modeling for a blood centrifuge device.* Computers and Fluids, 2013. **86**: p. 185-198.
74. Yano, T., et al., *An estimation method of hemolysis within an axial flow blood pump by computational fluid dynamics analysis.* Artificial Organs, 2003. **27**(10): p. 920-925.
75. *ANSYS Fluent 14.0: Theory guide*. 2011, Canonsburg, Pennsylvania: ANSYS Inc.
76. Reynolds, W.C., *Fundamentals of turbulence for turbulence modelling and simulation*. 1987.
77. Rodi, W., *Turbulence models and their application in hydraulics*. 1993.
78. Menter, F.R., *Two-equation eddy-viscosity turbulence models for engineering applications.* The American Institute of Aeronautics and Astronautics 1994. **32**(8): p. 1598-1605.
79. Al-Azawy, M., A. Turan, and A. Revell. *Investigating the use of turbulence models for flow investigations in a positive displacement ventricular assist devices*. in *IFBME Conference*. 2015. IFMBE Proceedings.
80. Carswell, D., et al., *A CFD model for the prediction of haemolysis in micro axial left ventricular assist devices.* Appl Math Model, 2013. **37**: p. 4199-4207.
81. Kido, K., et al., *Computational fluid dynamics analysis of the Pediatric tiny centrifugal blood pump (TinyPump).* Artificial Organs, 2006. **30**(5): p. 392-399.
82. Song, X., et al., *Studies of turbulence models in a computational fluid dynamics model os a blood pump.* Artificial Organs, 2003. **27**(10): p. 935-937.
83. *ANSYS Fluent 14.0, User's Guide*. ed.
84. Evans, E.A. and R. Skalak, *Mechanics and thermodynamics of biomembranes: part 1.* CRC Critical Reviews in Bioengineering, 1979. **3**(3): p. 181-330.
85. Sutera, S.P., *Flow-induced trauma to blood cells.* Circulation Research, 1977. **41**: p. 2-8.
86. Watanabe, N., et al., *Deformability of human red blood cells exposed to a uniform shear stress as measured by a cyclically reversing shear flow generator.* Physiological Measurement, 2007. **28**(5): p. 531-545.
87. Boehning, F., et al., *Hemolysis in a laminar flow-through Couette shearing device: an experimental study.* Artificial organs, 2014. **38**(9): p. 761-765.
88. Klaus, S., et al., *In vitro blood damage by high shear flow: human versus porcine blood.* The international Journal of Artificial Organs, 2002. **25**(4): p. 306-312.
89. Klaus, S., et al., *Investigation of flow and material induced hemolysis with a Couette type high shear system.* Materials Science and Engineering Technology, 2001. **32**(12): p. 922-925.
90. Leverett, L.B., et al., *Red blood cell damage by shear stress.* Biophysical journal, 1972. **12**(3): p. 257-273.

91. Pirro, D. and M. Quadrio, *Direct numerical simulation of turbulent Taylor-Couette flow*. European Journal of mechanics - B/Fluids, 2007. **27**: p. 552-566.
92. Luchini, P. and M. Quadrio, *A low-cost parallel implementation of direct numerical simulation of wall turbulence.* Journal of Computational Physics, 2006. **211**(2): p. 551-571.
93. Bacher, R.P. and M.C. Williams, *Hemolysis in capillary flow*. Journal of Laboratory and Clinical Medicine, 1970. **76**(3): p. 485-496.
94. Keshaviah, P.R., *Hemolysis in the accelerated flow region of an abrubt contraction*. 1974, University of Minnesota.
95. Blackshear, P.L., *Hemolysis at prosthetic surfaces*. 1972, Marcel Dekker: New York. p. 523-562.
96. Down, L.A., D.V. Papavassiliou, and E.A. O'Rear, *Significance of extensional stresses to red blood cell lysis in a shearing flow.* Annals of Biomedical Engineering, 2011. **39**(6): p. 1632-1642.
97. Yen, J.H., et al., *The effects of extensional stress on red blood cell hemolysis.* Biomedical Engineering: Applications, Basis and Communications, 2015. **27**(5): p. 1550042.
98. Bird, R.B., W.E. Stewart, and E.N. Lightfoot, *Transport phenomena*. Second ed. 2002, New York: John Wiley & Sons, Inc.
99. Chin, C., J.P. Monty, and A. Ooi, *Reynols number effects in DNS of pipe flow and comparison with channels and boundary layers.* International Journal of Heat and Fluid Flow, 2014. **45**: p. 33-40.
100. Chapra, S.C. and R.P. Canale, *Numerical methods for engineers*. 2010.
101. Blackshear, P.L., et al., *Shear wall interaction and hemolysis.* Transactions American Society for Artificial Internal Organs, 1966. **12**: p. 113-120.
102. Grigioni, M., et al., *A discussion on the threshold limit for hemolysis related to Reynolds shear stress.* Journal of Biomechanics, 1999. **32**(10): p. 1107-1112.
103. Vargas, R.R., *The effects of varying levels of turbulence in a submerged turbulent jet*, in *Albert Nerken School of Engineering*. 2001, The Cooper Union.
104. Xia, L.P. and K.M. Lam, *Velocity and concentration measurements in initial region of submerged round jets in stagnant environment and in coflow.* J Hydro Environ Res, 2009. **3**: p. 21-34.
105. Ungate, C.D., D.R.F. Harleman, and G.H. Jirka, *Stability and mixing of submerged turbulent jets at low reynolds numbers*. 1975, Massachusetts Institute of Technology: M.I.T. Energy Laboratory.
106. Lee, J.H. and V.H. Chu, *Turbulent jets and plumes - A Lagrangian approach*. 2003, Massachusetts, USA: Kluwer Academic Publisher. 390.
107. Hulet, C., *Interaction phenomena of submerged jets and fluidized solids*, in *Chemical and Biochemical Engineering*. 2006, The University of Western Ontario.
108. Panchapakesan, N.R. and J.L. Lumley, *Turbulence measurements in axisymmetric jets of air and helium. Part 1. Air jet.* J Fluid Mech, 1993. **246**: p. 197-223.
109. Hussein, H.J., S.P. Capp, and W.K. George, *Velocity measurements in a high-Reynolds-number, momentum-conserving, axisymmetric, turbulent jet.* Journal of Fluid Mechanics, 1994. **258**: p. 31-75.

Appendices

Appendix A

Eddy Analysis

The first step of eddy analysis is calculating Kolmogorov length scale (KLS) values in the flow domain. Kolmogorov length scale is described as $KLS = \left(\frac{\nu^3}{\varepsilon}\right)^{1/4}$, where ν is kinematic viscosity and ε is the dissipation rate of turbulent kinetic energy. Since, KLS is not directly available in Fluent, KLS calculation was defined as a custom field function for every experiment of every simulated system. As can be seen on Figure 0.1, the formula of KLS was defined in the *Definition* box of the *Custom Field Function* in Fluent.

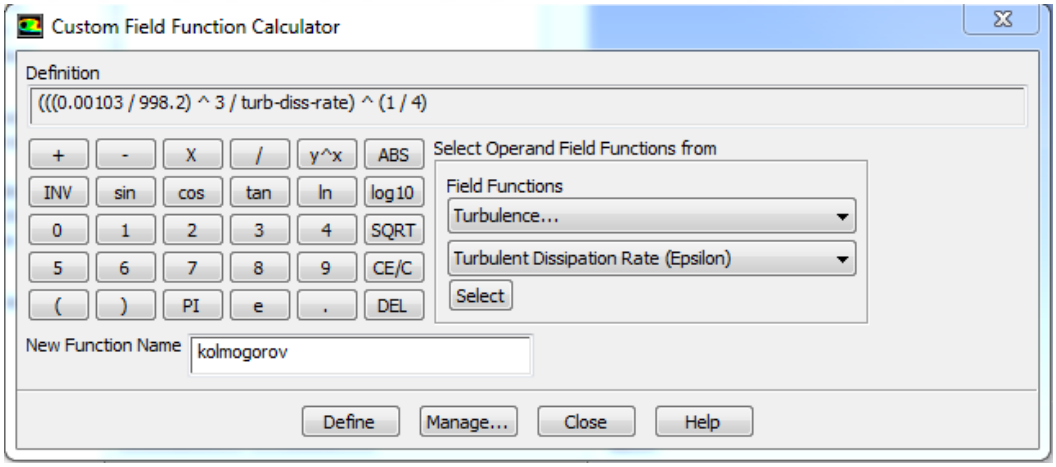

Figure 0.1. Custom field function for KLS in Fluent.

KLS calculations were determined for the entire flow domains of each experiments of every system (the Couette viscometer, the capillary tube, and the jet). For capillary tube and jet, several planes were created and for the Couette viscometer a vertical plane was used (since the KLS values were the same when moving circumferentially as can be seen

in Figure 3.4). Plane creations were already discussed for all the systems in Sections 3, 4, and 6 for the Couette viscometer, the capillary tube, and the jet, respectively. The important point when creating planes is that planes are needed to be created in a distances so that KLS values stays constant between them. Therefore, several trials are needed to find the places where KLS values stays constant.

After calculating KLS values in each plane, a contour surface was created for each KLS in KLS bins of 1 μm. Contour surfaces were created using *Iso-Clip* option in Fluent. As can be seen from Figure 0.2, *Iso-Clip* window shows the KLS range of each plane for the *Custom Field Function* for KLS that was presented in Figure 0.1. Plane list can be seen on the right part of Figure 0.2 for the specified experiment of specific system.

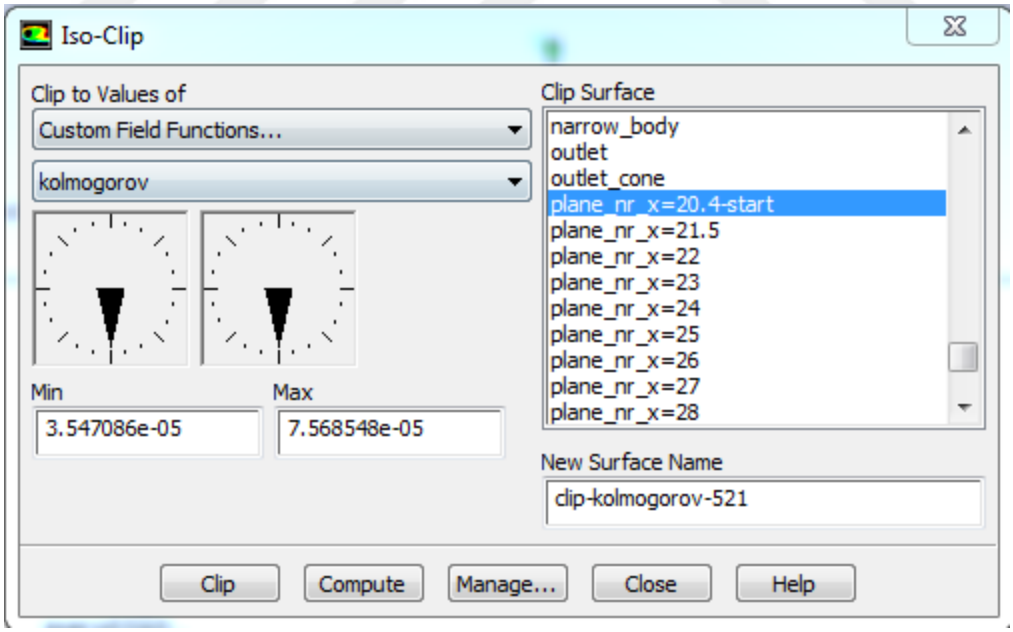

Figure 0.2. Creating contour surfaces for KLS in Fluent.

Contour surfaces were created by choosing each plane and then creating KLS bins of 1μm for the entire KLS range of each plane. Number of contour surfaces change depend on

the number of experiments of each system and the number of planes for every experiment of each system. Approximate numbers of contours surfaces for each system is shown in Table 0.1.

Table 0.1. Number of contour surfaces for simulated systems

Experimental systems	**Total number of experiments**	**Approximate total number of contour surfaces**
Couette viscometer	7	100
Capillary tube	4	1700
Jet	13	7000

Surface area of each contour surface was calculated in Fluent and imported into Excel. It is important to check that total surface area of contour surfaces for a specified plane has to be equal to the surface area of that specific plane. The rest of the *eddy analysis* was completed by post-processing in Excel.

The total volume of regions containing dissipative eddies of similar spherical size was calculated by multiplying the interplanar distance of the segmented computational domain by the cross-sectional surface area of each KLS value with increments of 1μm. Eddy volume for each KLS size was calculated as $V_{eddy} = \frac{4}{3}\pi(KLS/2)^3$. The number of eddies ($N_{eddy}$) of a specific size was calculated by dividing the total volume of the region and the volume of one eddy (V_{eddy}). Finally, the total surface area of eddies for each KLS value (A_{eddy}) was calculated as $A_{eddy} = N_{eddy}4\pi(KLS/2)^2$. The results were normalized by calculating eddy surface area, eddy number, and eddy volume per-unit-

volume to create quantities that might be compared for different turbulent flow situations and experimental configurations.

After all the calculations were performed for each experiment, all of the experiments of every systems were combined and analyzed together. For each KLS size, calculated eddy surface areas (or eddy numbers or eddy volumes) were combined together and plotted with experimental hemolysis.

List of Equations for Eddy Analysis

Equations for the eddy analysis was summarized below and also presented in Table 0.2.

- **Kolmogorov length scale (KLS):**

$$KLS = \left(\frac{\nu^3}{\varepsilon} \right)^{1/4} \quad \textbf{(1)}$$

- **Total volume of region for each specific KLS (V_{total}):**

$$V_{total} = \text{surface area (from Fluent)} * \text{length of the domain} \quad \textbf{(2)}$$

- **Volume of one eddy (V_{eddy}):**

$$V_{eddy} = \frac{4}{3}\pi \left(\frac{KLS}{2} \right)^3 \quad \textbf{(3)}$$

- **Number of eddies (N_{eddy}):**

$$Neddy = \frac{V_{total}}{V_{eddy}} \quad \textbf{(4)}$$

- **Total surface area of eddies for each KLS value (A_{eddy}):**

$$A_{eddy} = N_{eddy} * 4 * \pi * \left(\frac{KLS}{2}\right)^2 \quad \textbf{(5)}$$

Table 0.2. Computational equations of eddy analysis in excel for the highest shear stress (450 Pa) experiment of the Couette viscometer.

$KLS = \left(\frac{\nu^3}{\varepsilon}\right)^{1/4}$	From Fluent	V_{total} = surface area * L	$R_{eddy} = (KLS/2)$	$V_{eddy} = \frac{4}{3}\pi\left(\frac{KLS}{2}\right)^3$	$Neddy = \frac{V_{total}}{V_{eddy}}$	$A_{eddy} = N_{eddy} * 4 * \pi * \left(\frac{KLS}{2}\right)^2$
KLS, µm	Eddy surface area, m^2	Total volume, m^3	Radius of eddy, m	Eddy volume, m^3	Number of eddies	Total eddy surface area, m^2
1	2.20E-08	2.20E-08	1.50E-06	1.41E-17	1.56E+09	4.40E-02
2	1.04E-06	1.04E-06	2.50E-06	6.54E-17	1.59E+10	1.25E+00
3	1.65E-06	1.65E-06	3.50E-06	1.80E-16	9.19E+09	1.41E+00
4	1.80E-06	1.80E-06	4.50E-06	3.82E-16	4.73E+09	1.20E+00
5	2.32E-06	2.33E-06	5.50E-06	6.97E-16	3.34E+09	1.27E+00
6	3.53E-06	3.54E-06	6.50E-06	1.15E-15	3.08E+09	1.63E+00
7	2.44E-06	2.44E-06	7.50E-06	1.77E-15	1.38E+09	9.78E-01
8	1.56E-06	1.56E-06	8.50E-06	2.57E-15	6.06E+08	5.50E-01
9	1.02E-06	1.02E-06	9.50E-06	3.59E-15	2.84E+08	3.22E-01
10	7.27E-07	7.28E-07	1.05E-05	4.85E-15	1.50E+08	2.08E-01
11	4.57E-07	4.58E-07	1.15E-05	6.37E-15	7.20E+07	1.20E-01

Appendix B

Results for Hemolysis Models of Different Functions

Additional results that show comparison between experimental hemolysis and hemolysis from our model are presented in this section.

Figure 0.3 shows the results presenting the fitting 3 systems separately by using the power law type function (Eq. 7.1). Figure 0.4, Figure 0.5, and Figure 0.6 present the results for fitting every 2 systems together (Couette viscometer-jet, jet-capillary tube, and capillary tube-couette viscometer) by using the power law type function (Eq. 7.1). Figure 0.7 illustrates, results for fitting every system separately by using exponential type function (Eq. 7.4).Figure 0.8, displays the results for fitting the 3 systems together by using a linear type function (Eq. 7.6).

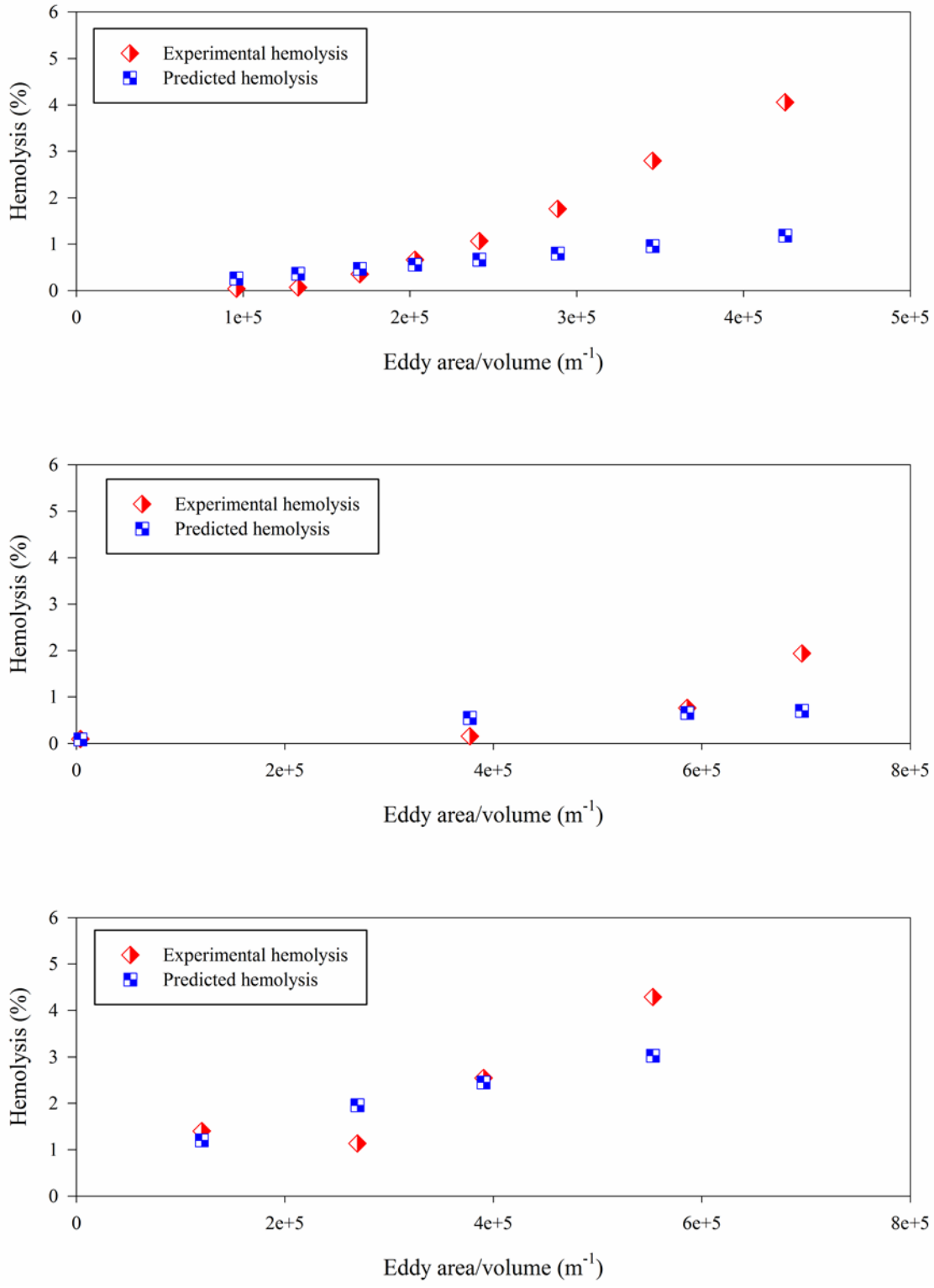

Figure 0.3. Comparison of experimental hemolysis and hemolysis from our model [Eq. (7.1)] by fitting the jet, capillary tube, and Couette viscometer separately. Top: jet, middle: capillary tube, bottom: Couette viscometer.

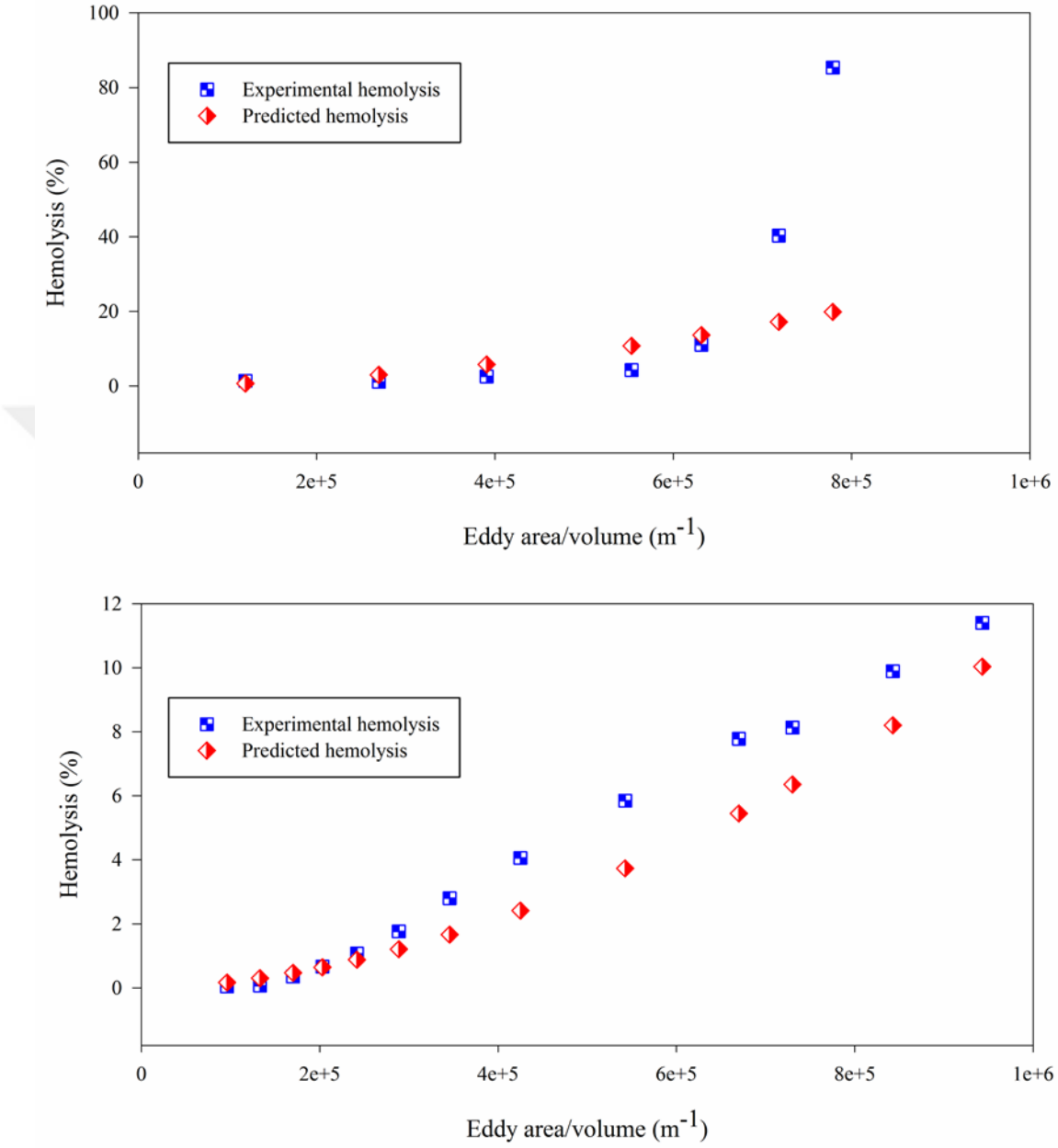

Figure 0.4. Comparison of experimental hemolysis and hemolysis from our model [Eq. (7.1)] by fitting the Couette viscometer (top) and jet (bottom) with power law function.

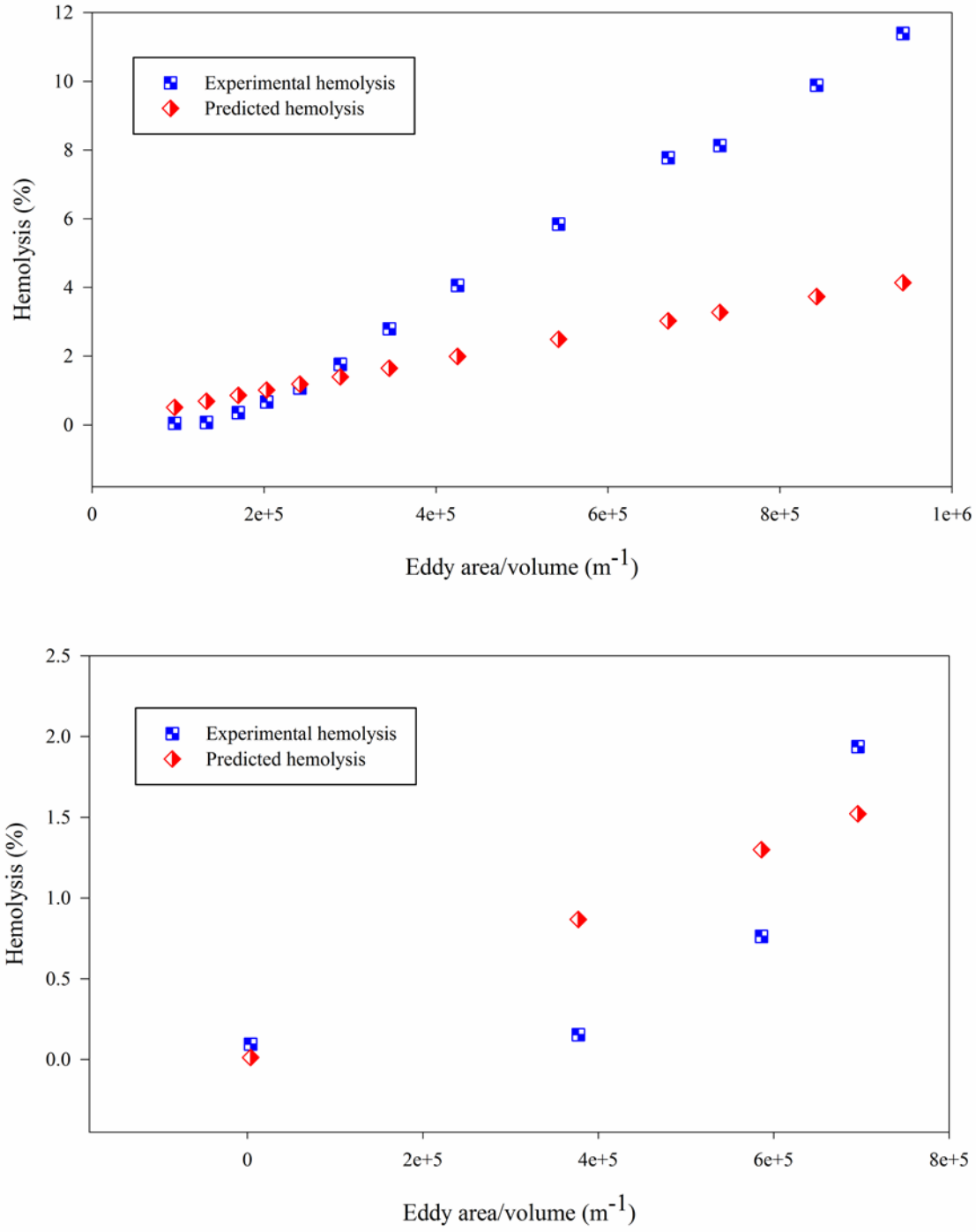

Figure 0.5. Comparison of experimental hemolysis and hemolysis from our model [Eq. (7.1)] by fitting the jet (top) and capillary tube (bottom) with power law function.

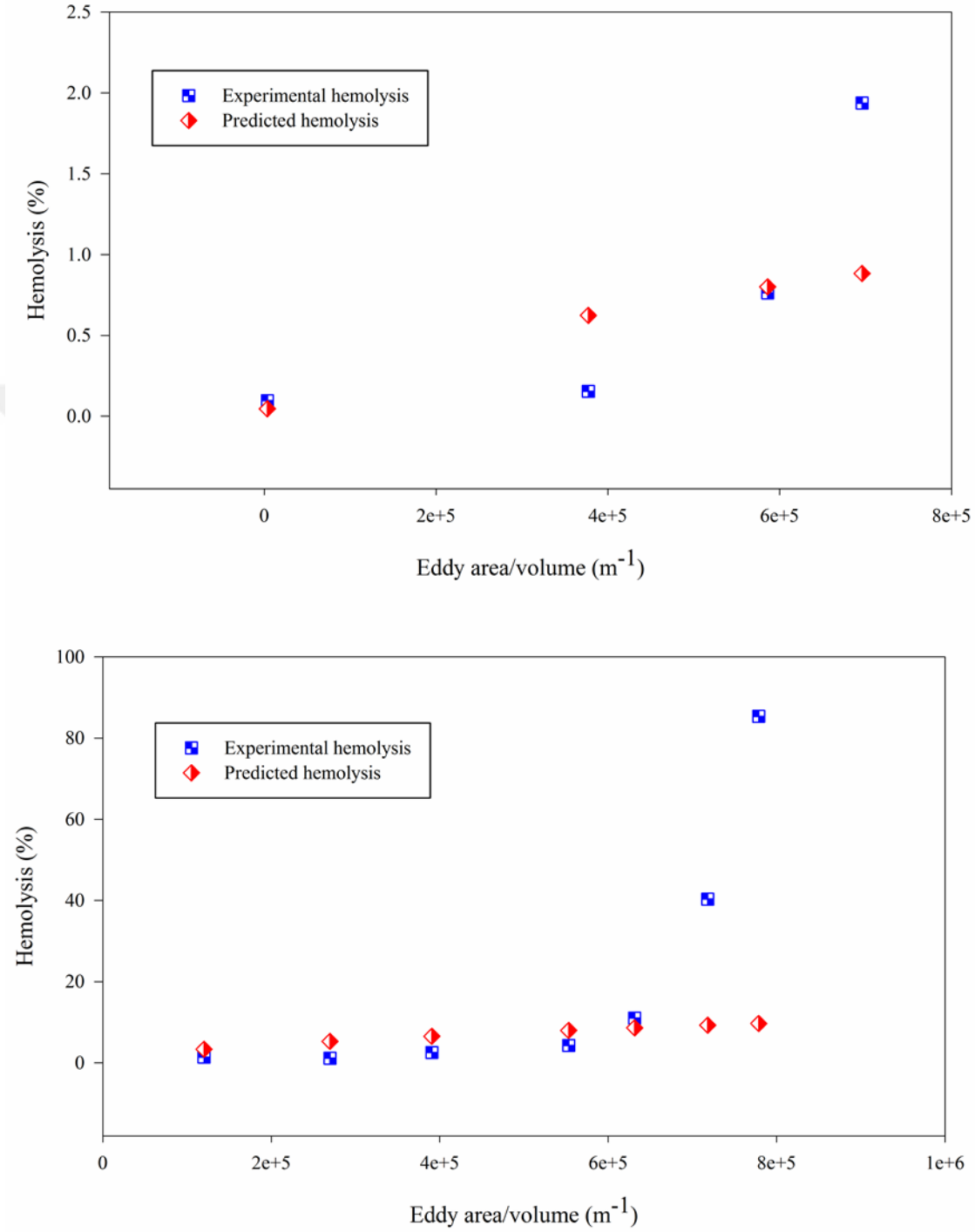

Figure 0.6. Comparison of experimental hemolysis and hemolysis from our model [Eq. (7.1)] by fitting the capillary tube (top) and the Couette viscometer (bottom) with power law function.

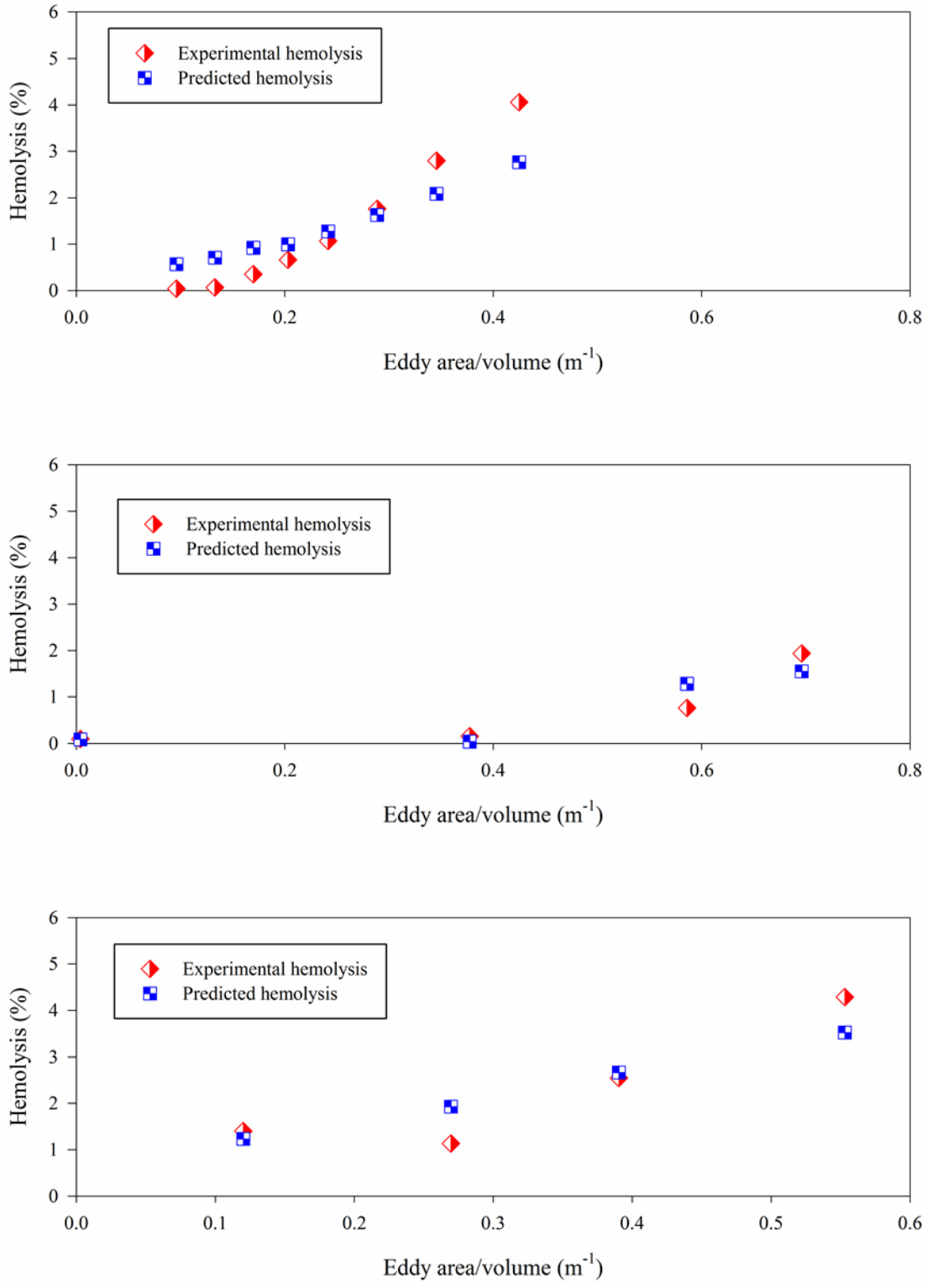

Figure 0.7. Comparison of experimental hemolysis and hemolysis from our model [Eq. (7.4)] by fitting the jet, capillary tube, and Couette viscometer separately. Top: jet, middle: capillary tube, bottom: Couette viscometer.

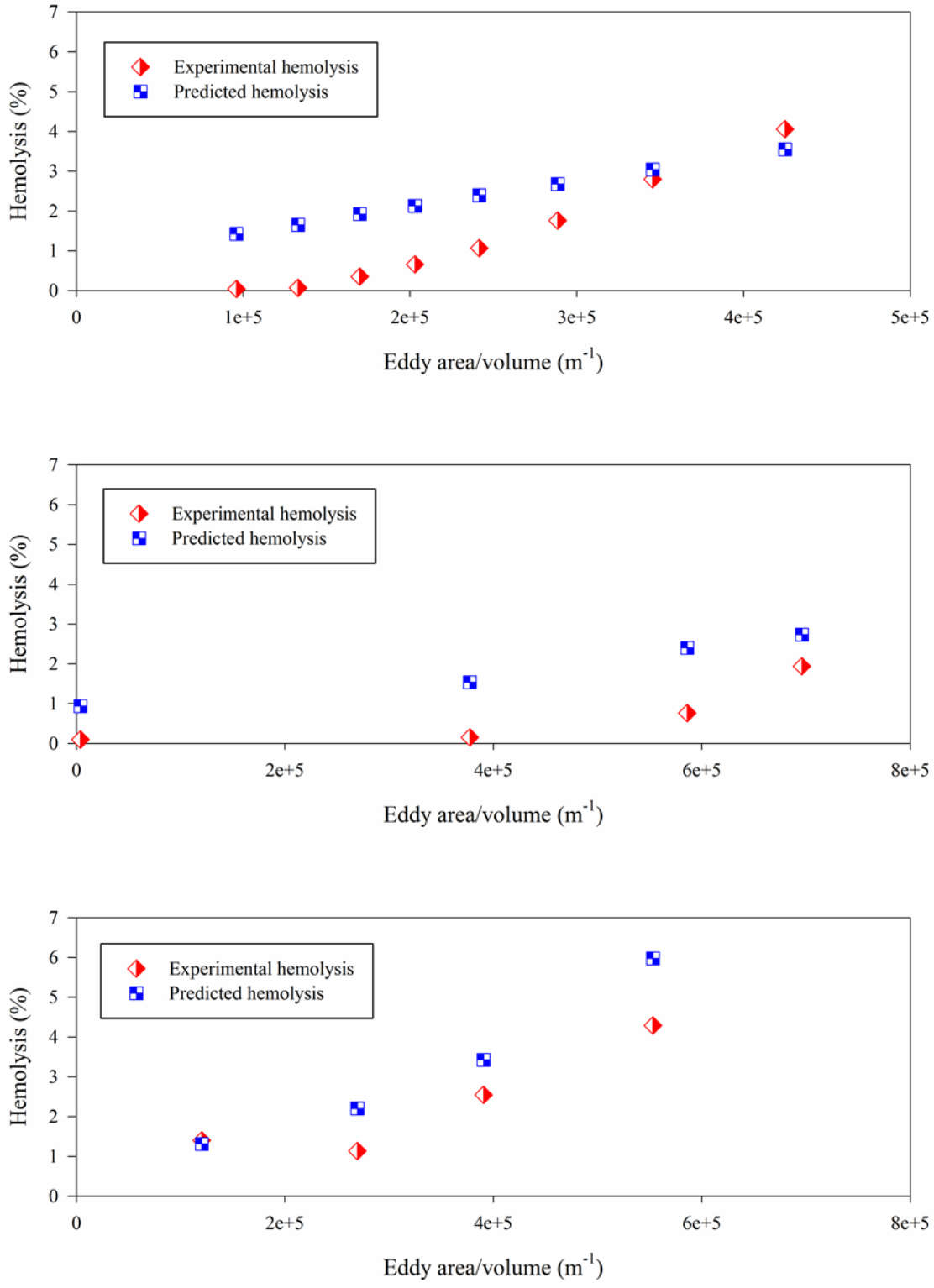

Figure 0.8. Comparison of experimental hemolysis and hemolysis from our model [Eq. (7.6)] by fitting the jet, capillary tube, and Couette viscometer together.